**Dissertation**
**submitted to the**
**Combined Faculties for the Natural Sciences and for Mathematics**
**of the Ruperto-Carola University of Heidelberg, Germany**
**for the degree of**
**Doctor of Natural Sciences**



presented by

Alban Kellerbauer, M.Sc.
born in Munich, Germany

Date of the oral examination: 3 July 2002

# A Study of the Accuracy of the Penning Trap Mass Spectrometer ISOLTRAP and Standard-Model Tests With Superallowed Beta Decays

Referees: Prof. Dr. H.-Jürgen Kluge
Prof. Dr. Andreas Wolf

**A study of the accuracy of the Penning trap mass spectrometer ISOLTRAP and Standard-Model tests with superallowed beta decays –** ISOLTRAP is a Penning trap mass spectrometer installed at the on-line isotope separator ISOLDE/CERN. It is dedicated to the measurement of the atomic masses of short-lived radioactive nuclides. Relative statistical uncertainties of individual mass measurements are typically of the order of $10^{-8}$. Using ions of carbon clusters whose mass ratios are exactly known, the various contributions to the total uncertainty of a mass measurement were studied. It was found by these measurements that the limit of the relative uncertainty of a mass measurement is $8 \cdot 10^{-9}$, more than an order of magnitude better than previously expected. Using the new measurement and evaluation procedure adopted as a result of this study, the $Q$ value of the superallowed beta decay of $^{74}$Rb was determined via a mass measurement of the mother and the daughter nuclide. With a half-life of under 65 ms, $^{74}$Rb is the shortest-lived nuclide ever investigated in a Penning trap. This experimental result allowed a contribution to the verification of the conserved-vector-current hypothesis of the weak interaction, a postulate of the Standard Model. It also served as a check of calculated parameters that are required for more stringent tests in the future.

**Eine Untersuchung der Genauigkeit des Penningfallen-Massenspektrometers ISOLTRAP und Tests des Standard-Modells mit Hilfe von übererlaubten Beta-Zerfällen –** ISOLTRAP ist ein Penningfallen-Massenspektrometer, das an dem on-line Isotopenseparator ISOLDE/CERN installiert ist. Es dient der Messung der atomaren Massen von kurzlebigen radioaktiven Nukliden. Die statistischen Meßungenauigkeiten einzelner Massenmessungen erreichen in etwa $10^{-8}$. Mit Hilfe von Kohlenstoffcluster-Ionen, deren Massenverhältnisse exakt bekannt sind, wurden die unterschiedlichen Beiträge zur Gesamtmeßungenauigkeit einer Massenmessung untersucht. Aus diesen Messungen folgt, daß die erreichbare relative Genauigkeit von ISOLTRAP-Massenmessungen $8 \cdot 10^{-9}$ beträgt, mehr als eine Größenordnung besser als bisher angenommen. Unter Verwendung der neuen Meß– und Auswertungsprozedur, die sich aus dieser Untersuchung ergeben hat, wurde der $Q$-Wert des übererlaubten Beta-Zerfalls von $^{74}$Rb über Massenmessungen des Mutter– und des Tochternuklids bestimmt. Mit einer Halbwertzeit von unter 65 ms ist $^{74}$Rb das kurzlebigste Nuklid, das je in einer Penningfalle untersucht wurde. Dieses experimentelle Ergebnis hat es erlaubt, einen Beitrag zur Überprüfung der CVC-Hypothese (Erhaltung des Vektor-Stroms) der schwachen Wechselwirkung zu leisten, die ein Axiom des Standard-Modells ist. Es wurde außerdem dazu verwendet, berechnete Parameter, die für zukünftige noch strengere Tests benötigt werden, auf ihre Richtigkeit hin zu überprüfen.

Pour Mélanie

Und um zu wissen, was ich schon ahnte, beugte ich mich über das Wasser hinaus und hob die Laterne, und aus dem schwarzen Spiegel sah mir ein scharfes und ernstes Gesicht mit grauen Augen entgegen, und das war ich. Und da kein Weg zurückführte, fuhr ich auf dem dunkeln Wasser weiter durch die Nacht.

aus „Märchen," Hermann Hesse (1912)

# Acknowledgment

I want to thank my supervisor H.-Jürgen Kluge for his guidance that despite the large geographical distance has always proved highly effective. In some difficult situations his encouragements helped put me back on track. Many thanks to my former CERN group leader Georg Bollen who, besides initiating me to the art of running such a complex experiment as ISOLTRAP, organized my financial support via a CERN Doctoral Student Fellowship. My current CERN group leader Juha Äystö has very generously continued that support, both scientifically and financially.

This thesis would not have been possible without the excellent experimental work achieved by the ISOLTRAP team, in particular the help of my current colleagues Klaus Blaum and Frank Herfurth and former collaborators Michael Kuckein, Emmanuel Sauvan, and Christoph Scheidenberger. I would also like to thank the many people who were part of the ISOLTRAP group or the ISOLDE group at different times for their professional contributions and, in some cases, for their friendship.

I am indebted to Georges Audi for his patient assistance with the Atomic-Mass Evaluation and valuable discussions of the carbon cluster results. I thank Dave Lunney for the discussions of the physics results of this thesis work and for proofreading part of the text. Many thanks to Ian S. Towner for very kindly providing me with the results of his calculations of the statistical rate functions and other input parameters for my work.

A special thanks goes to my former supervisor and mentor Robert B. Moore for inflaming me with his enthusiasm for a very wide range of applied-physics subjects and for unconditionally supporting me throughout my studies. It was also he who sent me to CERN as a doctoral student to work on the ISOLTRAP experiment.

Finally I would like to thank my wife Mélanie for her encouragement and for the many sacrifices she made during the last few months of my thesis work and writing. I dedicate this thesis to her.

# Table of Contents

# List of Figures

# List of Tables

# 1 Introduction

Since the publication in 1905 by Einstein of his postulate of the equivalence of mass and energy [Eins1905], we know that the total mass of a complex system of bodies is not simply given by the sum of the masses of its constituents. More particularly, the mass of an atom is the sum of the masses of its constituents minus the various binding energies that hold them together. The reason why it took until 1905 for such a fundamental law to be discovered is that the total energy of most systems of particles is very much larger than the binding energies involved.

It follows from this mass–energy equivalence that mass measurements can yield a wealth of information on the forces that are at work in the studied systems. Ultimately, atomic-physics techniques can thus be used to investigate the fundamental particles and the interactions between them. The main obstacle to such studies is the required precision. The masses of medium-heavy atoms, for instance, are of the order of 100 GeV/$c^2$, while nuclear-structure effects such as nucleonic pairing and shell structure have an energy scale of about 1 MeV. Moreover, only differences in binding energies actually convey information, thereby further reducing the energy scale involved. This also means that mass determinations with a view to an investigation of nuclear-structure effects must achieve relative mass uncertainties of better than $10^{-6}$.

Two experiments dedicated to atomic-mass measurements on radioactive nuclides are installed at the ISOLDE facility at CERN (Geneva, Switzerland): The radiofrequency transmission spectrometer MISTRAL and the Penning trap mass spectrometer ISOLTRAP [Lunn2000]. They represent the techniques that can currently attain this level of precision. MISTRAL, designed for the very short-lived nuclides, reaches a resolving power of about 100 000 and a relative precision of better than $5 \cdot 10^{-7}$. ISOLTRAP, which attains resolving powers of as much as $10^7$, can be used to routinely carry out mass measurements with a relative uncertainty of $1 \cdot 10^{-7}$. The masses of close to two hundred radioactive nuclides have already been successfully measured with ISOLTRAP at this level of precision [Boll2001]. The half-life limit of the nuclides studied with ISOLTRAP has been continuously reduced and now reaches below 100 ms.

Some fundamental studies, however, such as a verification of the conservation of the weak vector current (CVC hypothesis) or the unitarity of the Cabibbo-Kobayashi-Maskawa matrix (CKM matrix), both postulates of the Standard Model, require accurate mass measurements with precisions at the $10^{-8}$ level [Hard2001], which seemed out of reach for exotic nuclides until now. The possibility of conducting these tests provided the motivation for pushing mass measurements of radioactive nuclides beyond the $10^{-7}$ precision barrier.

A major upgrade in the beam preparation stage of the ISOLTRAP experiment in 1999 brought about an immense improvement in the transmission of the entire setup. Relative statistical uncertainties for individual cyclotron frequency measurements close to $10^{-8}$ are now routinely achieved, putting the high-precision studies mentioned above within reach of a Penning trap experiment for the first time. But in order to benefit from this gain in precision, the systematic effects, whose contribution to the uncertainty of the measure-

ment had previously been estimated to be at the level of $10^{-7}$, had to be studied more comprehensively.

For this purpose, a carbon cluster ion source was installed at the ISOLTRAP setup. With the help of clusters of $^{12}$C, whose masses are exact multiples of the microscopic mass standard, the accuracy of the experiment was for the first time experimentally determined. The results of this study have shown that a modified measurement and evaluation procedure, along with the improved statistical uncertainty, provides the precision that is required for a test of the CVC hypothesis via a study of the superallowed beta decay of $^{74}$Rb.

The main part of this work thus consisted of the measurement of the mass difference between $^{74}$Kr and the very short-lived $^{74}$Rb, the least well-known of the three experimentally accessible parameters that govern the decay of $^{74}$Rb. The result of this measurement, which extends the nuclear-physics contribution to tests of the Standard Model, was put into the perspective of the high-precision data for the superallowed beta decays of the lighter nuclides.

In Chap. 2, an overview of the experimental setup and technique is given. The functions of ISOLTRAP's main components, from the production of reference ions to the actual cyclotron frequency determination, are explained in detail. The principle of a mass measurement and how it is obtained from the cyclotron frequency ratio of two different ion species is also shown. Chapter 3 gives an account of construction and operation of the carbon cluster ion source and the measurements that have been conducted with it to determine the accuracy limit of the setup. The mass measurements of radioactive krypton and rubidium isotopes that were performed for a determination of the $Q$ value of the $^{74}$Rb($\beta^+$)$^{74}$Kr decay are described in Chap. 4. The ramifications of the experimental results for the CVC hypothesis are discussed in Chap. 5.

# 2 The ISOLTRAP experiment

A mass measurement with ISOLTRAP is carried out via a determination of the cyclotron frequency $\nu_c$ of an ion with charge $q$ and unknown mass $m_{\text{ion}}$ in a strong magnetic field [Boll1996]:

$$\nu_c = \frac{1}{2\pi}\frac{q}{m_{\text{ion}}}B\,. \tag{2.1}$$

The magnitude $B$ of the magnetic field is inferred from the cyclotron frequency measurement of an ion whose mass is already known to high precision.

The structure of the ISOLTRAP apparatus is based on the principle of separation of function. It consists of four main components, serving very distinct purposes. Figure 2.1 shows a functional sketch of these four main components. The ions produced either by the ISOLDE target–ion source or by the reference ion source are first decelerated, radially cooled, and bunched in the RFQ ion beam cooler and buncher (RICB). The cooled ion bunches are then transported to the cooling Penning trap, where isobaric contaminants are removed through mass-selective cooling. In the last stage, the precision Penning trap, the actual mass measurement is carried out using a time-of-flight cyclotron resonance technique.

ISOLTRAP's physical setup is shown in Fig. 2.2. The stable alkali reference ion source located upstream of the RICB allows the testing and preparation of the setup before radioactive experiments. Furthermore, the nuclides produced in this ion source are used as reference ions for mass measurements.

The RICB is located on the ground level of the ISOLDE hall, while the cooling trap and the precision trap occupy the first and second floor of a tall platform. An electrostatic 90-degree deflector is used to direct the ion bunches from the RICB upwards to the Penning trap setup. Micro-channel-plate (MCP) detectors along the trajectory are used for beam diagnostics. MCP 5 is also the detector used for the mass measurement; its function will be explained in 2.2.3.

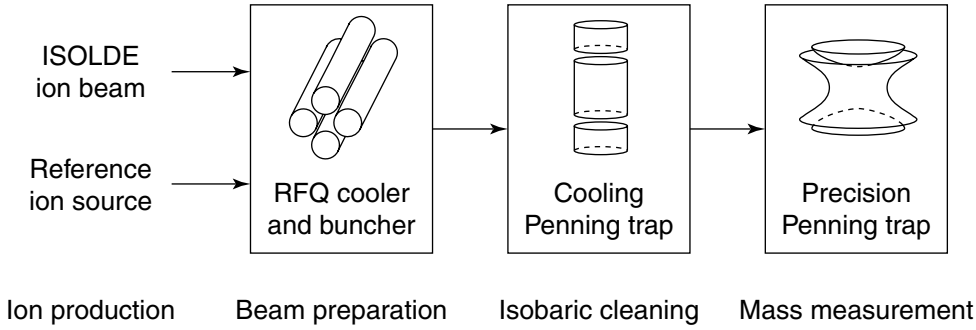


Figure 2.1: Sketch of the main components of the ISOLTRAP mass spectrometer and their functions.

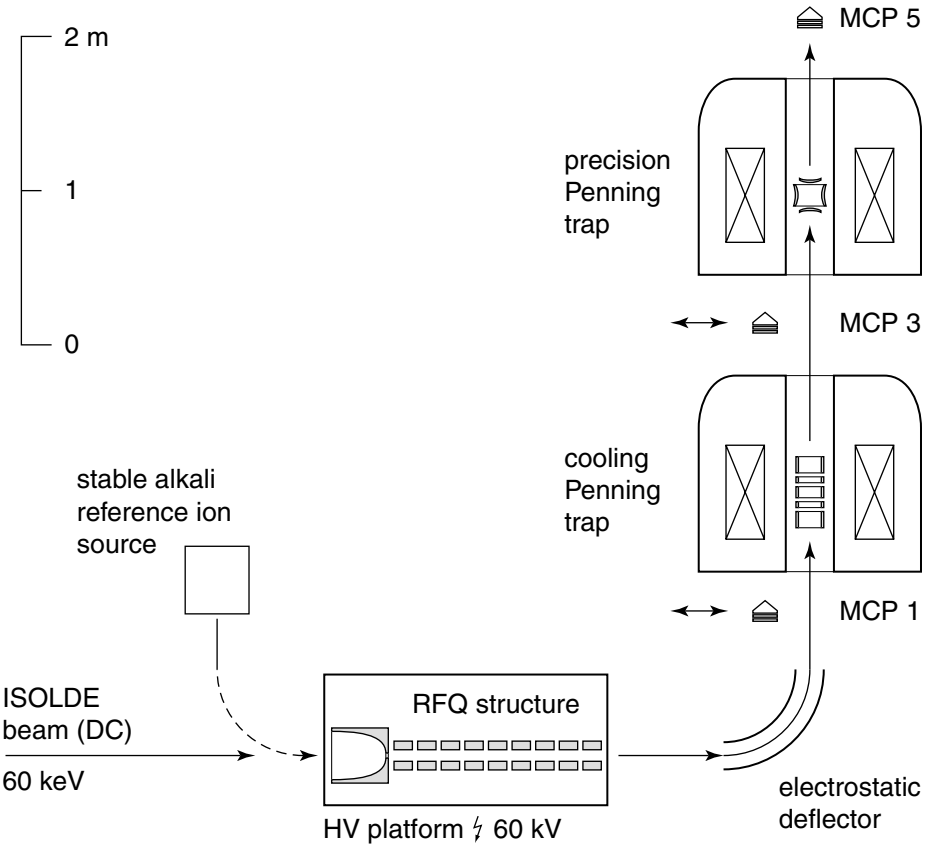


Figure 2.2: Sketch of the complete ISOLTRAP setup, consisting of the stable alkali reference ion source, the RFQ ion beam cooler and buncher, the cooling Penning trap, and the precision Penning trap. Micro-channel-plate (MCP) detectors are located along the trajectory of the ions for beam diagnostics purposes.

Figure 2.3 shows a photograph of the ISOLTRAP platform in the ISOLDE hall. On the bottom left, one can distinguish the high-voltage cage that houses the RFQ ion beam cooler and buncher. On the first and second floor of the platform, the stainless-steel vessels of the superconducting magnets can be seen, in which the two Penning traps are located.

In the following, an overview of the ISOLDE facility as well as a detailed description of all three components of the ISOLTRAP apparatus will be presented. A more in-depth account of the theoretical background of ion trapping in Penning traps is given in App. A.

## 2.1 The on-line isotope separator ISOLDE

The ISOLDE facility is the fourth-generation on-line isotope separator (ISOL) installation at CERN [Kugl2000]. Its purpose is the production of pure beams of low-energy radioactive ions for a large number of different physics and radiochemistry experiments. As far as the production rates of short-lived radionuclides are concerned, ISOLDE is to-

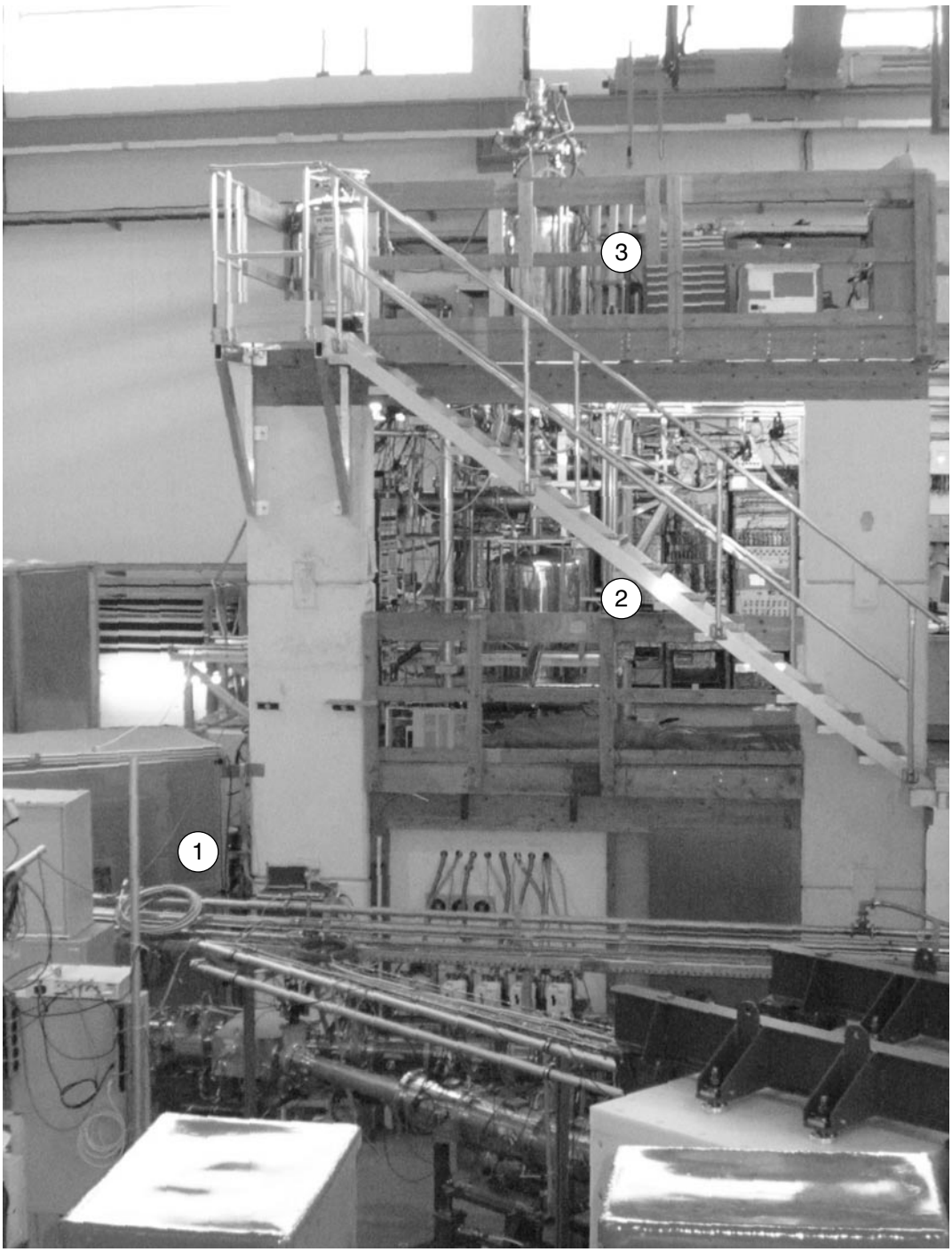


Figure 2.3: Photograph of the ISOLTRAP platform. The locations of three traps are indicated in the figure: (1) The high-voltage cage with the RFQ ion beam cooler and buncher; (2) The vessel of the superconducting magnet of the cooling Penning trap; (3) The vessel of the superconducting magnet of the precision trap.

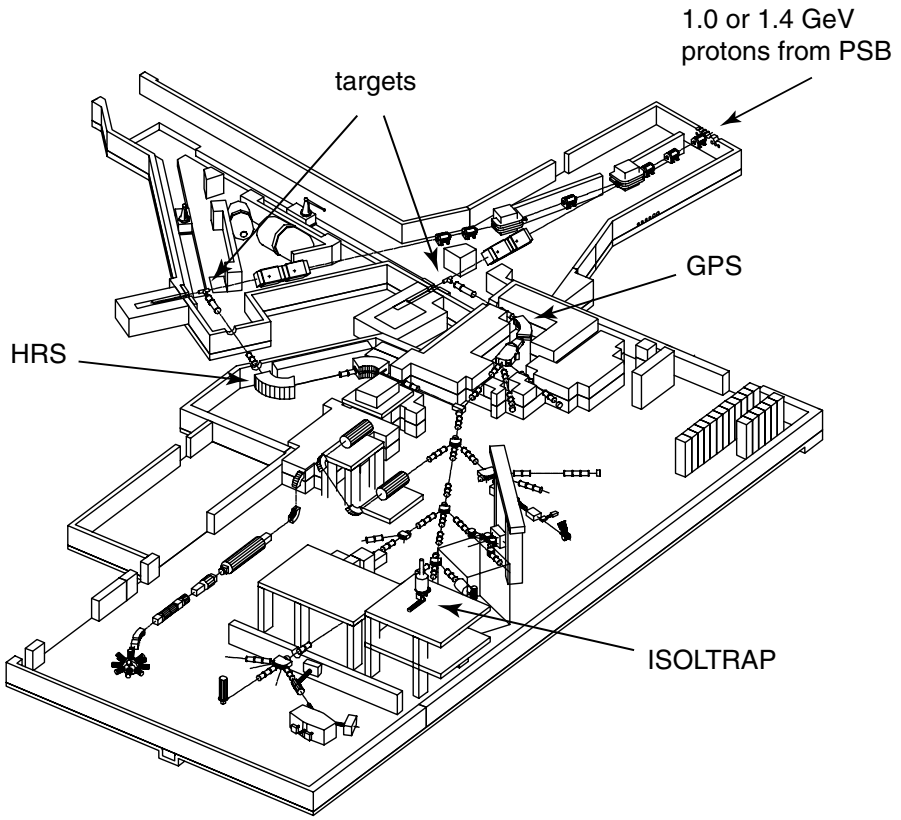


Figure 2.4: Overview of the experimental hall of the ISOLDE facility. The ISOLTRAP experiment is installed at the central beam line. It extends over the three levels of the platform indicated at the bottom of the figure.

day the world's leading radioactive-beam facility. It supplies radioactive ions to more than 300 physicists working on more than 30 experiments in the experimental hall and the surrounding buildings.

Figure 2.4 shows an overview of the ISOLDE hall. In its current configuration, ISOLDE is supplied with protons from the Proton Synchrotron Booster (PSB). The PSB, a stack of four synchrotrons, delivers very short high-intensity proton pulses at a repetition rate of 1.2 s. In the ISOLDE target area, located in the upper left part of the figure, a thick target in one of the two target stations is bombarded with pulses of up to $3 \cdot 10^{13}$ protons at either 1 or 1.4 GeV. The radioactive nuclides are produced through fission, spallation, and fragmentation reactions. Depending on the desired radioactive species, different target materials, such as magnesium oxide or uranium carbide, are used.

After the diffusion of the radionuclides from the target, they reach the ion source. The radioactive atoms are ionized either by surface ionization, in a hot plasma, or by laser ionization before being accelerated into a 60-keV quasi-DC ion beam. The different methods employed for the ionization of the reaction products take advantage of physical or chemical properties of the different species to efficiently ionize the desired nuclide

and heavily suppress all unwanted contaminants. More than 60 elements and about 600 isotopes can presently be produced with the ISOLDE facility.

The two target stations deliver the ion beams to two different sector magnet mass separators. The general purpose separator (GPS) consists of one 90-degree H magnet with a field magnitude of 0.45 T. It achieves a resolving power of about 2400. The more recent high-resolution separator (HRS) is made up of one 60-degree magnet and one 90-degree magnet, both C magnets with 0.7-T fields. It routinely reaches a mass resolving power of 7000; by careful tuning, a resolving power well above 10 000 can be reached.

Downstream of the mass separators, the beam lines are merged into the main beam line which distributes the radioactive ion beam to the experiments located in the experimental hall. The ion-optical elements along the beam lines for focusing and deflection are exclusively electrostatic devices in order to assure a mass independence of the beam transport.

## 2.2 The ISOLTRAP triple trap setup

### 2.2.1 The RFQ ion beam cooler and buncher

The first trap of the ISOLTRAP setup is the RFQ ion beam cooler and buncher, a radiofrequency quadrupole ion guide [Herf2001a, Herf2001b]. Its installation in 1999 constitutes the most recent major improvement to the apparatus. Together with its specially designed injection electrode [Kell2001], its task is the preparation, *i.e.* the cooling, accumulation, and bunching of the ISOLDE DC ion beam. The injection electrode matches the phase space of the ISOLDE ion beam, with a longitudinal energy of 60 keV and an emittance of about 35 $\pi$ mm mrad, to the acceptance of the RFQ ion guide.

Figure 2.5 shows a detailed sketch of the RICB. The ions are electrostatically decelerated from 60 keV to about 100 eV in the injection electrode before being injected into the ion guide. The ion guide is enclosed in a cylindrical vacuum chamber, into which a buffer gas is admitted near the center. The trap is typically operated with helium as buffer gas at a pressure of about 1 Pa. Radially, the ion guide is operated with an RF field only, *i.e.* almost no mass selectivity is obtained.

In the ion guide, the ions are radially confined in the pseudo-potential well of the RF quadrupole field while their radial and remaining longitudinal energy are damped in collisions with the buffer gas. As the kinetic energy of the ions is dissipated, they are dragged along the ion guide by a smooth axial DC field applied to the segmented rods whose potential has a minimum near the end on the exit side. In this three-dimensional well, which constitutes a linear Paul trap within the ion guide, a large number of ions (up to about $10^4$) can be accumulated.

After a cooling and accumulation time of several milliseconds, the axial potential is lowered towards the exit orifice and the ion bunch is ejected. A pulsed drift tube located behind the RICB prevents the ions from being reaccelerated to the full initial energy as they leave the HV platform. The ions are accelerated to the transport energy of about 2.8 keV as they enter the tube, which is initially at a potential of about 57.2 kV. As the ions traverse the drift tube, its potential is switched to ground and the ions are therefore

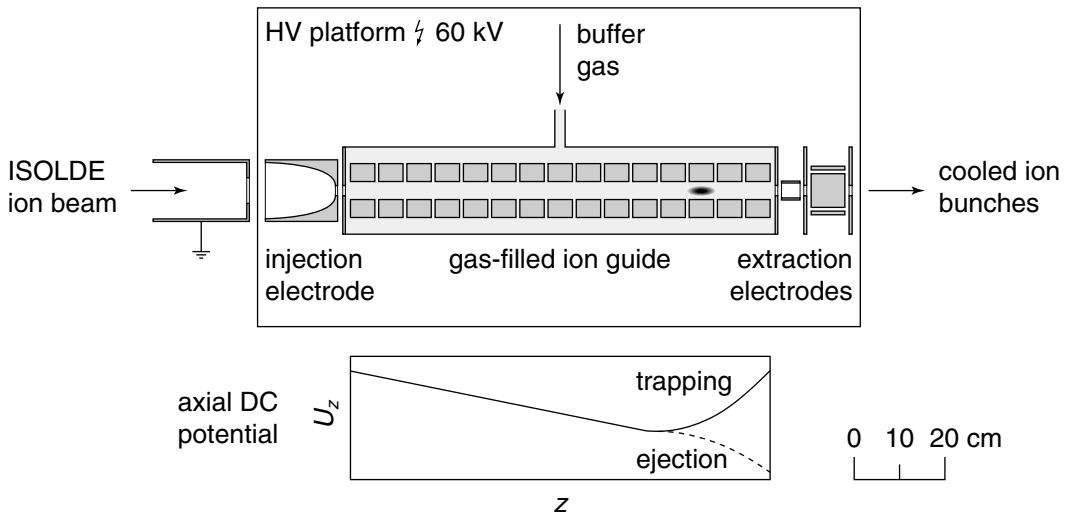


Figure 2.5: Detailed sketch of the RFQ ion beam cooler and buncher. The decelerated ion beam is radially confined by an RFQ field and cooled in buffer gas collisions. The ions are accumulated in a linear-Paul-trap region near the end of the RFQ structure. After a storage time of several 10 ms, the ion bunch is ejected and reaccelerated to the transport energy of about 2.8 keV.

not accelerated again when they exit the tube.

The acceptance of the RICB is carefully matched to the phase space of the ISOLDE beam. This is why an efficiency improvement of more than three orders of magnitude was observed after its installation [Herf2001b]. A DC capture efficiency of up to $\epsilon_{\mathrm{DC}} \approx 35$ % and a total capture, cooling, and bunching efficiency of up to $\epsilon_{\mathrm{tot}} \approx 15$ % were measured. An analysis of the shape of the ejected pulse showed that ions were cooled to close to room temperature after about 20 ms (for $^{133}$Cs). The pulse shape also suggests that the longitudinal emittance of the ejected ion pulse is about $\xi_{\mathrm{long}} \approx 10$ eV $\mu$s. Using a beam observation system, the transverse emittance (at 2.5 keV) was estimated to be $\xi_{\mathrm{trans}} \approx 10\,\pi$ mm mrad. This corresponds to an emittance of about $2\,\pi$ mm mrad at 60 keV which, compared to the original ISOLDE beam, constitutes a more than 15-fold reduction in transverse phase space.

### 2.2.2 The cooling Penning trap

A Penning trap is the combination of an azimuthal quadrupolar electric potential and a strong axial magnetic field. The motion of an ion in such an electromagnetic trap is a superposition of three harmonic eigenmotions, one axial and two radial. The two radial modes, the magnetron motion with frequency $\nu_-$ and the modified cyclotron motion with frequency $\nu_+$, can be coupled by an azimuthal quadrupole excitation at the sum frequency. The sum frequency is in fact the cyclotron frequency $\nu_c$, as introduced in Eq. (2.1), of an

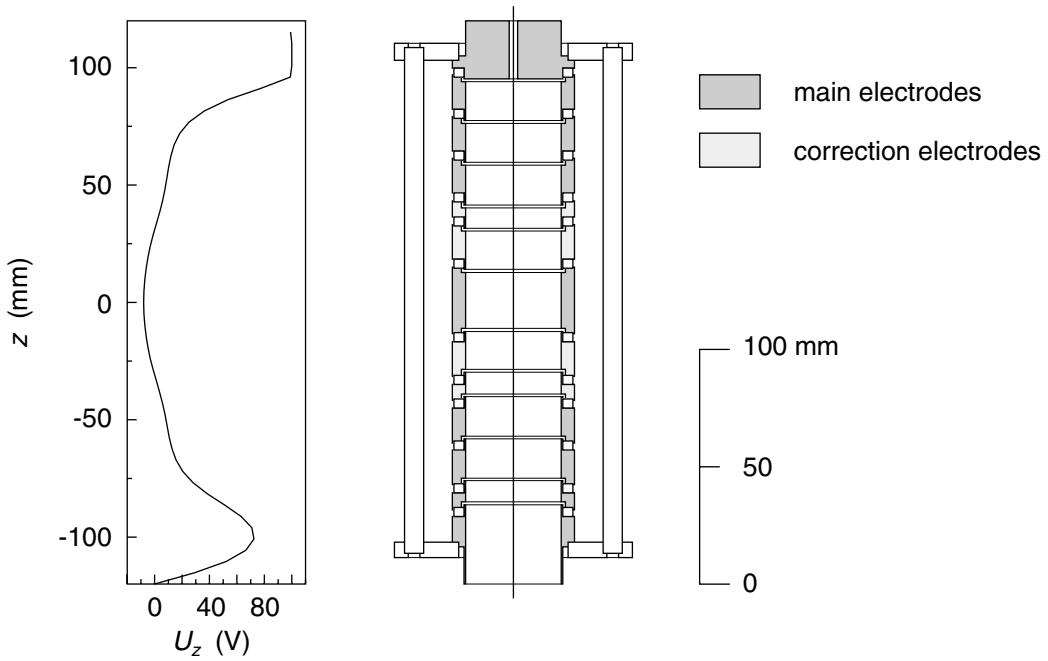


Figure 2.6: Detailed sketch of the cooling Penning trap. The cylindrical trap has an inner diameter of 35 mm and is 250 mm long. The graph on the left shows the potential on the axis which results from the appropriate voltages applied to the cylinder segments.

ion in a pure magnetic field [Brow1986]:

$$\nu_c = \nu_+ + \nu_- . \tag{2.2}$$

This relation is exploited in both Penning traps of the ISOLTRAP setup in the excitation of the ion motion.

In the buffer-gas-filled cooling trap, all three characteristic motions of the ions are cooled in buffer gas collisions. While the amplitudes of the axial and the cyclotron motion are reduced, a cooling of the magnetron motion leads to an increase of its radius. The radial modes of the ions can be excited by means of an azimuthal dipolar or quadrupolar RF field applied to the four-fold segmented ring electrode of the trap. When the ions are excited with a quadrupolar field at the cyclotron frequency $\nu_c$, these motions are coupled and the magnetron motion is constantly converted into modified cyclotron motion, which in turn is cooled. The result is that the radial amplitude is decreased and the ion is brought to the trap center. This cooling and centering technique is mass-selective and can therefore be used for an isobaric cleaning of the ion sample [Sava1991]. The main task of this first Penning trap is thus the removal of contaminant ions from the sample.

Figure 2.6 shows a detailed sketch of ISOLTRAP's cooling trap. It is a cylindrical Penning trap placed in the homogeneous field of a 4.7-T superconducting magnet [Raim1997]. A nested potential well is formed by applying DC potentials to its 13

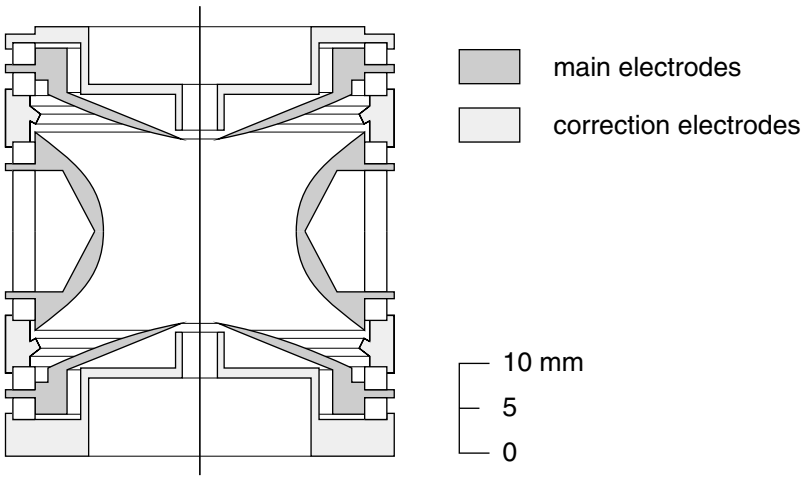


Figure 2.7: Detailed sketch of the precision Penning trap. The precision trap is a hyperboloidal trap placed in the homogeneous field of a 5.9-T superconducting magnet. Its ring electrode has an inner radius of 13 mm. The correction electrodes are designed such as to reduce deviations from the ideal quadrupole field.

cylindrical segments. The outer shape of this trap is optimized for the capture of ion bunches at several 10 eV, while its central part is carefully shaped to achieve a quadrupolar potential over the largest possible volume. This and the large inner radius of the cooling Penning trap of 17.5 mm allow the acceptance of a wide incoming ion bunch and make it possible to store and cool more than $10^4$ ions at a time. The helium buffer gas pressure is typically maintained at about $10^{-4}$ Pa to $10^{-3}$ Pa, which, depending on the cooling time, leads to mass resolving powers of the order of $10^4$ to $10^5$ [Boll1996]. Storage times of several hundred milliseconds without significant losses are easily achieved in the cooling trap.

### 2.2.3 The precision Penning trap

After the isobaric separation in the cooling trap, the selected ion species is further transferred to the precision Penning trap, where the actual mass measurement takes place. The precision trap also has a four-fold segmented ring electrode, but instead of containing a buffer gas, it is operated at a vacuum of about $10^{-5}$ Pa. A detailed sketch of the precision trap is shown in Fig. 2.7. It is a high-precision hyperboloidal Penning trap which is placed in the homogeneous field of a 5.9-T superconducting magnet.

In the precision trap, the ions are first subjected to an azimuthal dipolar excitation at the magnetron frequency which causes an increase of the magnetron radius. An azimuthal quadrupolar RF field at the cyclotron frequency $\nu_c$ then leads to a conversion of the magnetron motion into modified cyclotron motion. Since the reduced cyclotron frequency is considerably larger than the magnetron frequency, the ions gather kinetic energy in the process. When the ion bunch is finally ejected out of the trap towards an MCP detector

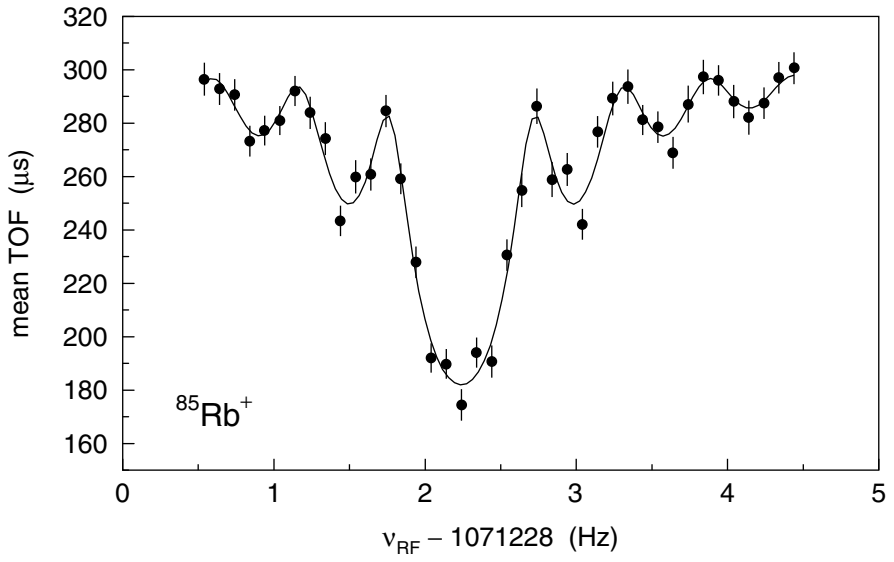


Figure 2.8: Time-of-flight (TOF) resonance curve of $^{85}Rb^{+}$ at an excitation time of $T_{RF} = 1.8$ s. The solid line is a fit of the theoretically expected line shape to the data points [Köni1995]. For this particular resonance, a resolving power of $\nu/(\delta\nu)_{FWHM} \approx 1.5 \cdot 10^6$ is achieved.

(MCP 5 in Fig. 2.2), it passes through the inhomogeneous-magnetic-field region of the superconducting magnet. In an inhomogeneous magnetic field, a force proportional to the magnetic moment is exerted on the ions and their radial energy is converted into longitudinal energy. The ions whose radial motion has been resonantly excited have gained a larger radial energy and thus also a larger magnetic moment. Therefore they reach the detector after a reduced flight time compared to those whose magnetron motion has not been converted into modified cyclotron motion [Gräf1980].

The frequency of the azimuthal quadrupolar excitation is scanned, leading to a TOF cyclotron resonance, of which a typical example for $^{85}Rb^{+}$ ions is shown in Fig. 2.8. The shape of this resonance is well understood [Köni1995] and its functional representation can be used to perform a least-squares fit to the data points and extract the cyclotron frequency of the ion and its experimental standard deviation. The observed sidebands are due to the rectangular envelope of the quadrupolar RF excitation signal. The depth of the main peak is a function of the initial radius of the magnetron motion before the excitation and the completeness of the conversion from magnetron to modified cyclotron motion, which in turn depends on the amplitude and the duration of the excitation.

For a given ion mass, the resolving power attained in the precision trap is essentially proportional to the duration of the RF excitation. For an excitation time of 10 s, a resolving power of about $10^7$ can be achieved with an ion of mass 100 u. This allows the resolution of nuclear ground and isomeric states of radioactive nuclides [Boll1992].

Isobaric contaminations whose mass is too close to the ion of interest to be removed in the cooling trap can be removed in the precision trap by dipolar excitation at the reduced

cyclotron frequency [Beck1997a]. In order to avoid sideband excitation of the desired ions, the excitation signal is modulated by a Gaussian envelope.

## 2.3 Principle of a mass measurement

Assuming that all ion species have the same charge $q = +e$, the atomic mass $m$ of the ion of interest can be calculated from the cyclotron frequency of the reference ion $\nu_{\mathrm{c,ref}}$, the cyclotron frequency of the ion of interest $\nu_{\mathrm{c}}$, the atomic mass of the reference ion $m_{\mathrm{ref}}$, and the electron mass $m_e$:

$$m = \frac{\nu_{\mathrm{c,ref}}}{\nu_{\mathrm{c}}} \, (m_{\mathrm{ref}} - m_e) + m_e \, . \tag{2.3}$$

However, in this manner, the uncertainty of the atomic mass of the reference ion contributes to the uncertainty of the mass result as well.

That is why ISOLTRAP's results are always reported in terms of the ratio $r$ of the cyclotron frequencies:

$$r = \frac{\nu_{\mathrm{c,ref}}}{\nu_{\mathrm{c}}} \, . \tag{2.4}$$

In this way, the mass of the ion of interest can be obtained at any given time using the most up-to-date knowledge of the mass of the reference ion. The primary ISOLTRAP result is independent of any changes in that knowledge.

Currently, the TOF resonances of the two ion species can't be recorded at the same time. Instead, the more rapidly obtained reference measurement is made once before and once after that of the investigated ion. The measured cyclotron frequencies are later interpolated to the time of the measurement of the ion of interest.

A complete ISOLTRAP mass measurement thus consists of three separate cyclotron frequency determinations: That of the ion of interest, preceded and followed by that of the reference ion. The primary measurand is their cyclotron frequency ratio $r$. The combined standard uncertainty of the primary result is determined according to the law of propagation of uncertainty. It is composed of the experimental standard deviations of the frequency measurements as well as the various uncertainties due to systematic effects.

# 3 A study of the accuracy of ISOLTRAP

## 3.1 Pushing the limits of mass accuracy

Mass measurements of stable nuclides with the SMILETRAP apparatus [Frit2001] and with the Penning trap at MIT [Brad1999] have demonstrated that Penning trap mass spectrometry of heavy ions can reach relative uncertainties of a few parts in $10^{-10}$ or better. SMILETRAP is connected to an electron beam ion source which supplies it with highly charged stable ions. As can be seen from Eq. (2.1), the higher charge state leads to a higher cyclotron frequency and thus, for a given frequency precision, to a smaller relative uncertainty. The performance of the MIT Penning trap is reached by placing the trap inside the cold bore of a superconducting magnet. This assures temperature stability of the trap and surrounding material as well as an ultra-high vacuum, thereby allowing long observation times (many hours) of single ions.

Radioactive nuclides, however, with their low production rates and short half-lives, as well as the environment necessary to create them, represent difficult challenges for a high-precision measurement in this field. ISOLTRAP is the apparatus that allows the most precise direct mass measurements of radioactive nuclides today.

In the past, the uncertainty of ISOLTRAP mass measurements due to all known or expected systematic effects was taken into account by the addition of a relative uncertainty to the final result. Based on an earlier study of the contributing effects, the magnitude of this relative uncertainty was conservatively estimated to be $1 \cdot 10^{-7}$ [Boll1996]. This included fluctuations of the magnetic field during the measurement as well as possible imperfections of the magnetic and electric fields. Even in the cases where production rates were high or where a large number of measurements could be conducted, the relative uncertainty of the final result was therefore limited to $1 \cdot 10^{-7}$.

Typical reference ions used in ISOLTRAP mass measurements are $^{39}$K, $^{85}$Rb, $^{87}$Rb, and $^{133}$Cs. These four nuclides can be produced in the surface ionization ion source that is mounted upstream of the ISOLTRAP triple trap setup. Except for $^{39}$K, their masses have been measured with relative uncertainties at the $10^{-10}$ level [Brad1999]. However, for measurements of nuclides whose mass falls outside of the range spanned by these four nuclides or differs by many mass units from the mass of the one nearest to it, an ion that is also produced by ISOLDE must be chosen. The masses of these reference ions are often not known to high precision. As can be seen from Eq. (2.3), this insufficient knowledge of the mass of the reference ion is an additional source of uncertainty when the final result is to be expressed in terms of mass.

The main aim of the present study was to attempt to identify and quantify all effects that contribute to the uncertainty of the primary result. A special emphasis was placed on identifying effects whose importance can be diminished by conducting a larger number of measurements. The ideal test bed for these tests was found in the carbon clusters,

which can be readily produced from the fragmentation of $C_{60}$ fullerenes, the ball-shaped molecules of carbon.

## 3.2 Carbon clusters

The discovery and synthesis of $C_{60}$ and $C_{70}$ [Krot1985, Krät1990] has stimulated exciting scientific studies. The fact that $C_{60}$ fullerenes can now be produced in macroscopic amounts and with high purity has opened the way for a variety of technical developments and fundamental research [Krot2000, Lifs2000]. Ionized carbon clusters produced via laser-induced fragmentation and ionization of $C_{60}$ can now also be readily studied in ISOLTRAP's tandem Penning trap setup [Blau2002a, Kell2002].

Apart from the molecular binding energies, all carbon clusters that are composed solely of the most abundant isotope $^{12}C$ have masses that are exact multiples of the unified atomic mass unit u [Quin1998]. They would therefore be the ideal choice of reference ions. This would allow to perform absolute mass measurements with ISOLTRAP, *i.e.* mass measurements in which the reference ion has no mass uncertainty. In this case, ISOLTRAP's final result could directly be expressed as a mass in atomic mass units.

Since carbon clusters with a wide range of masses and a mass spacing of only 12 u can be produced, they also constitute a dense grid for the investigation of systematic effects. In a cross-reference mass measurement, a measurement which is carried out using carbon clusters both as the reference ion and as the ion of interest, the true value of the ratio of the cyclotron frequencies $\nu_{c,ref}/\nu_c$ is exactly known. This means that cross-reference measurements can be used to identify errors of the apparatus or the measurement procedure and that the knowledge obtained in this way can be used to determine the uncertainties of actual mass measurements.

We have conducted a large number of these cross-reference measurements to verify the validity of a redefined measurement and analysis procedure. As a whole, they provide detailed information on the relative combined standard uncertainty $u_c(r)/r$ of a cyclotron frequency ratio determination. A $\chi^2$ test of that distribution gives insight into the possible presence and magnitude of residual systematic effects beyond those already taken into account in the new analysis procedure.

## 3.3 The carbon cluster ion source

The carbon cluster ion source is mounted about 2 m below the cooling Penning trap. Figure 3.1 shows an overview sketch of ISOLTRAP's tandem Penning trap setup with the carbon cluster source.

Details of the carbon cluster laser ion source are shown in Fig. 3.2. The carbon cluster ions are produced by use of laser-induced desorption, fragmentation, and ionization of $C_{60}$. To this end, the frequency-doubled beam of a Q-switched Nd:YAG laser (Quantel Brilliant B; repetition rate 1–10 Hz; pulse duration 6 ns; frequency 532 nm) is focused on a $C_{60}$ pellet (Aventis; purity of $C_{60} > 99\%$), which is placed at an accelerating potential of 2.8 kV. The focal spot area of the laser is about 0.1 $mm^2$ with a typical pulse energy

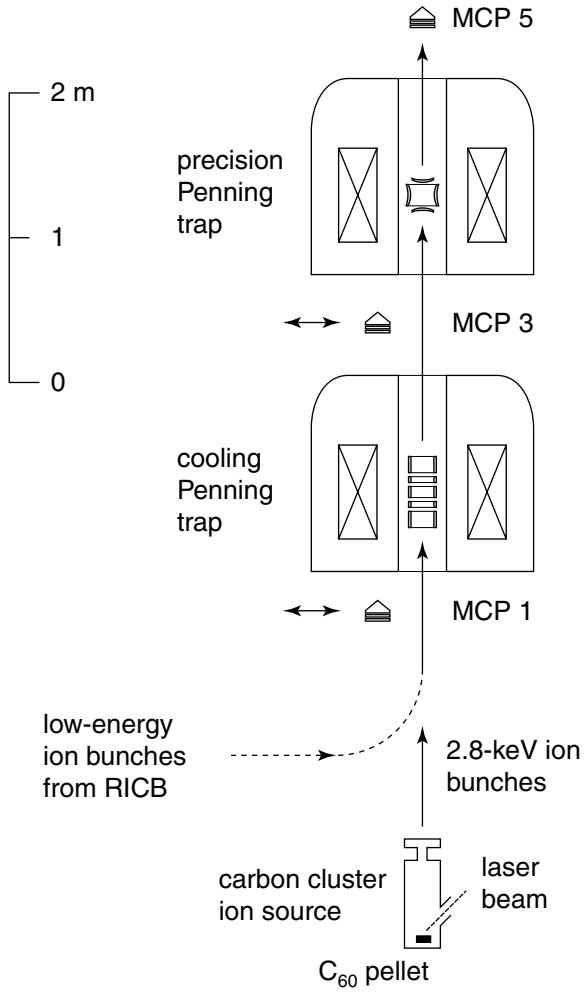


Figure 3.1: Overview sketch of the ISOLTRAP setup with the carbon cluster ion source. The source is mounted about 2 m below the cooling Penning trap.

of 10 mJ at 532 nm, corresponding to an estimated fluence of 10 J/cm$^2$. Desorption and ionization of $C_{60}$ set in at a laser pulse energy of about 5 mJ. At slightly higher pulse energies, the intensity of $C_{60}^+$ increases strongly and small amounts of lighter carbon cluster ions are produced by fragmentation [Sche2002].

The charged fullerene fragments $C_n^+$ are then electrostatically accelerated to 2.8 keV and transferred towards the cooling Penning trap. A typical time-of-flight (TOF) mass spectrum recorded on the micro-channel-plate (MCP) detector MCP 1 at a laser pulse energy of 10 mJ is shown in Fig. 3.3(a). The spectrum is characterized by a strong production of the high-mass, even-numbered fragments (fullerene fragments $C_{34-58}^+$) and the low-mass fragments $C_n^+$, $n \leq 27$. Between these two regions, a gap is observed. These characteristics of the spectrum are experimentally well understood in terms of the geometrical properties of the clusters [Wurz1994].

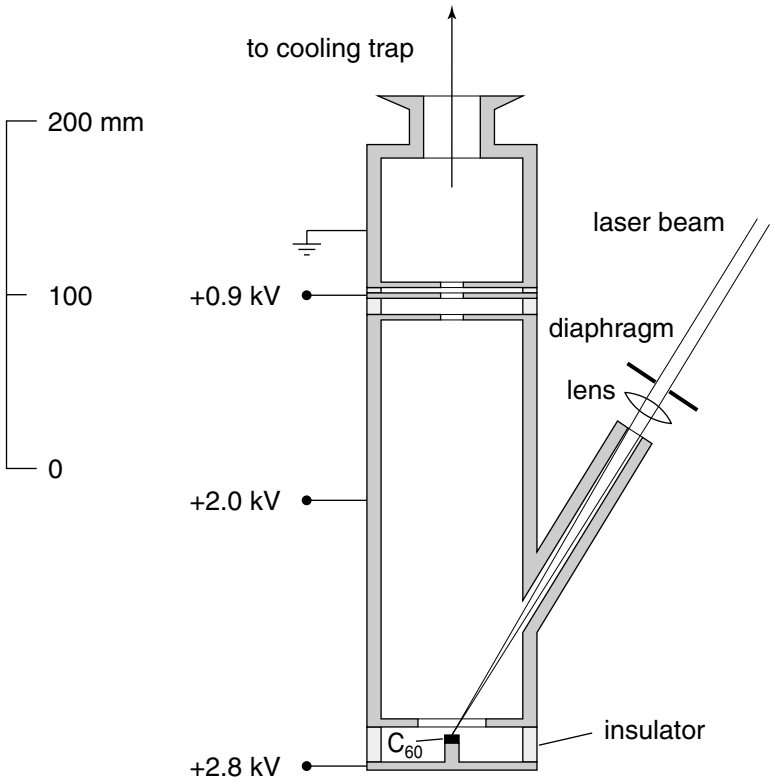


Figure 3.2: Detailed sketch of the carbon cluster ion source [Sche2002]. The carbon cluster ions are obtained from laser desorption, fragmentation, and photo-ionization of a $C_{60}$ pellet and are electrostatically accelerated towards the cooling trap.

As opposed to ion beams that are produced either at the ISOLDE target–ion source combination or at the surface ionization reference source, carbon clusters that are produced in the carbon cluster laser ion source do not pass through the RFQ ion beam cooler and buncher, but are directly transferred to the cooling Penning trap for cleaning. Isobaric contaminants should not be present at this stage, but clusters containing one or more of the other stable carbon isotopes need to be removed. Since the 90-degree bender upstream of the cooling trap has to be dismounted for the installation of the carbon cluster ion source, ions from ISOLDE and from the cluster source cannot yet be used simultaneously.

After being transported to the precision Penning trap, a TOF resonance of the carbon cluster ion is obtained in the standard way described in Chap. 2. A typical example of a cluster TOF resonance recorded in the precision trap obtained with $C_9^+$ ions is shown in Fig. 3.3(b).

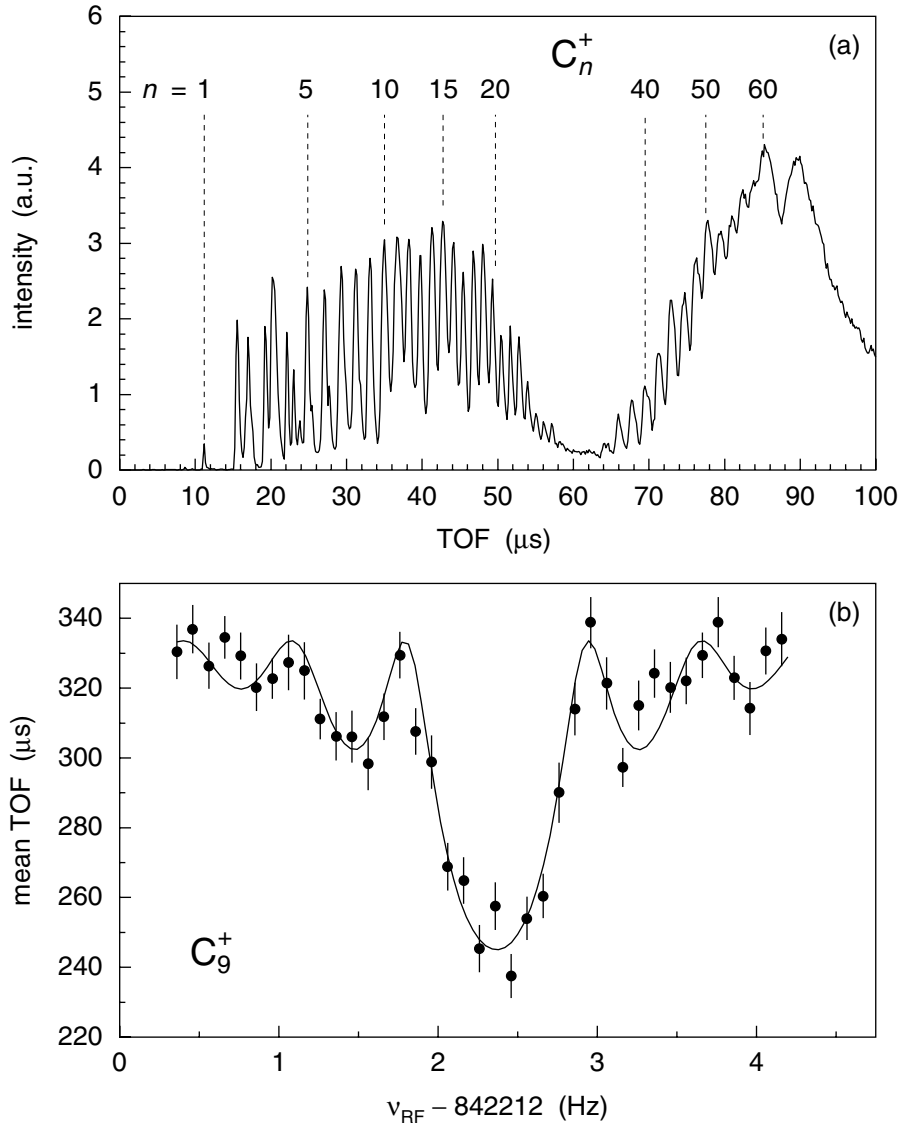


Figure 3.3: (a) Time-of-flight mass spectrum of carbon cluster ions produced by use of laser-induced desorption, fragmentation, and ionization of $C_{60}$ at 532 nm at a laser pulse energy of about 10 mJ, recorded at MCP 1. (b) Time-of-flight resonance curve of $C_9^+$. The solid line is a fit of the expected line shape to the data points [Köni1995].

## 3.4 Uncertainties of the measured quantities

In this section, all identified effects that contribute to the uncertainty of the primary result, the mean cyclotron frequency ratio $\bar{r}$, are discussed. For the sake of consistency, relative uncertainties are used throughout.

### 3.4.1 Cyclotron frequency of the ion of interest

#### Statistical uncertainty

For any recorded TOF resonance, the experimental standard deviation $s(\nu)$ of the cyclotron frequency[1] $\nu$ is a function of the resolving power of the precision trap, *i.e.* the RF excitation time $T_{\mathrm{RF}}$, and the total number $N_{\mathrm{tot}}$ of ions recorded. An empirical formula for this relation has been proposed [Boll2001]:

$$\frac{s(\nu)}{\nu} = \frac{1}{\nu} \cdot \frac{c}{\sqrt{N_{\mathrm{tot}}} \cdot T_{\mathrm{RF}}}\,, \tag{3.1}$$

where $c$ is expected to be a dimensionless constant.

In a series of cyclotron frequency measurements of the nuclide $^{85}$Rb, the functional relation proposed in Eq. (3.1) was verified and $c$ determined. Figure 3.4 shows the result of these measurements for different excitation times $T_{\mathrm{RF}}$ as a function of the number of ions $N_{\mathrm{tot}}$ recorded in a TOF resonance. To obtain records with different numbers of ions, long measurements were subdivided into several parts. It is found that $c$ is in fact independent of the excitation time and the number of ions, with an average value of

$$c = 0.898(8)\,. \tag{3.2}$$

In some special cases, such as for very low count rates or in the presence of contaminations, $c$ may differ from the value found for standard measurements.

#### Contaminations

The reference ions are produced in a dedicated ion source which makes available the ions of a few surface-ionizable elements. The mass separation between these species is sufficient to prevent mutual contaminations from reaching the precision trap. No contaminations stemming from the reference ion source have until now been observed in the precision Penning trap.

In the case of the ions of stable or radioactive nuclides produced in the ion source of the ISOLDE target, however, the presence of contaminations has to be expected. These can be isobaric or isomeric impurities that originate in the target or ion source itself, contaminations that are produced in the ISOLTRAP apparatus through charge exchange reactions with the buffer gas or with rest gas, or decay products of short-lived radioactive ions. Doubly charged ions undergo charge exchange reactions in the RFQ ion beam cooler and buncher where their charge state is either reduced to one or they are neutralized.

[1] In the following, the cyclotron frequency $\nu_{\mathrm{c}}$ will be denoted by the symbol $\nu$ to simplify the notation.

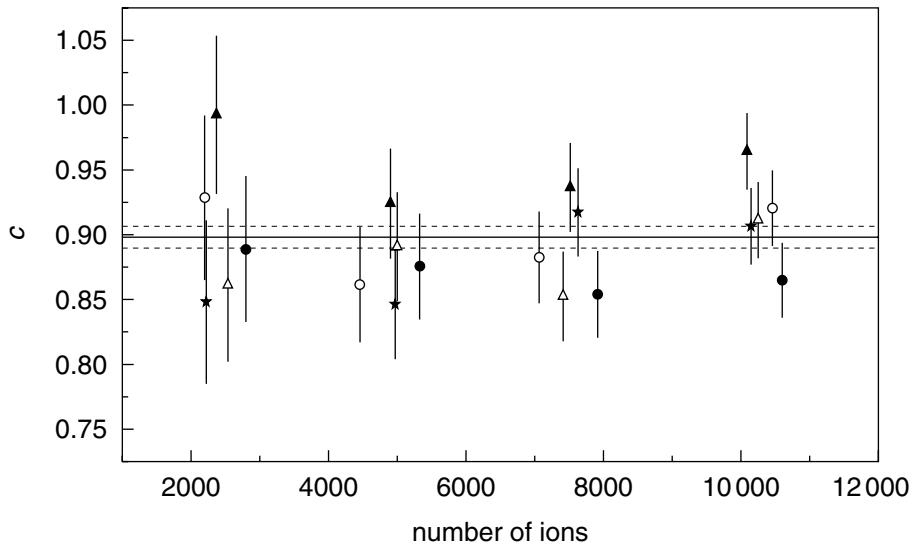


Figure 3.4: Determination of the parameter $c$ of Eq. (3.1) from a series of cyclotron frequency measurements of $^{85}Rb^{+}$. The parameter is plotted as a function of the total number of ions $N_{tot}$ recorded in a TOF resonance. The data labels represent different RF excitation times $T_{RF}$: 300 ms (empty circles), 600 ms (filled circles), 900 ms (empty triangles), 1200 ms (filled triangles), and 1500 ms (stars). The solid horizontal line is the weighted mean of all values and the dashed lines show the $1\sigma$ confidence interval of the mean.

Charge states higher than one have not been observed beyond the cooler and buncher stage.

The effect of the presence of a contaminant ion in the precision Penning trap has been extensively studied [Boll1992, Köni1995]. For a low number of ions in the precision trap, it expresses itself by the appearance of two separate resonance curves (assuming sufficient resolving power), one of which can be outside of the scanning range of the quadrupolar-excitation frequency. As the number of ions in the trap increases, these two resonance peaks successively approach each other. At the same time, the centroids are shifted to lower frequencies.

In order to correct for this contamination shift, $\nu$ is determined for different count rate classes, *i.e.* for different numbers of ions that were present in the precision trap. The centroid frequencies are plotted as a function of the center of gravity of the count rate distribution in that class. An example of such a plot for $^{36}Ar^{+}$ is shown in Fig. 3.5(a). A linear least-squares fit is then applied to the data points, shown as the solid straight line in the figure. The dashed lines represent the $1\sigma$ confidence interval of the fit, which in this case is of the order of $10^{-8}$ in relative uncertainty.

If the detection efficiency $\epsilon$ of the MCP detector of the precision Penning trap were one, a linear extrapolation of these data points to ion number unity would then yield the corrected centroid frequency. In reality, the detection efficiency of an MCP detector

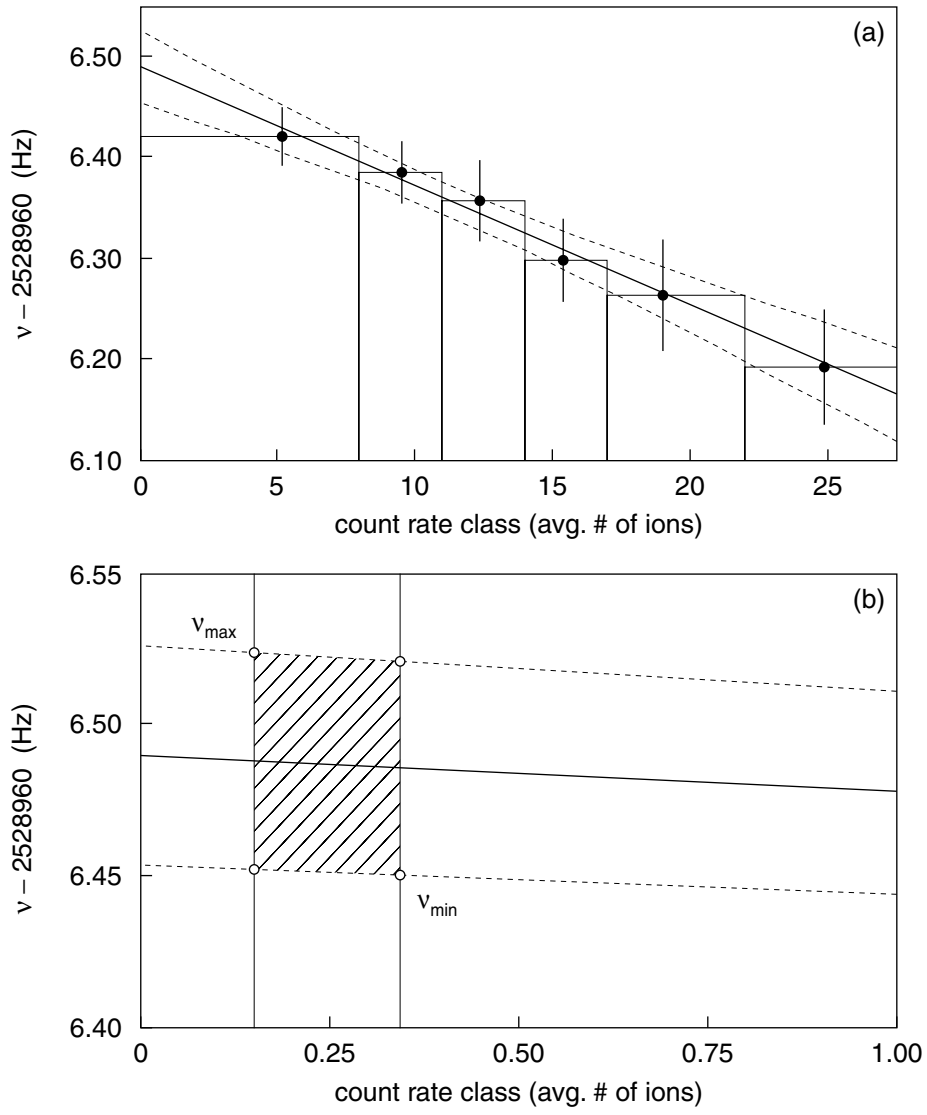


Figure 3.5: (a) Count rate dependence of the observed cyclotron frequency. The measurement was made with $^{36}Ar^{+}$ ions from ISOLDE, the contamination is probably due to $^{36}Cl^{+}$ ions. The count rate classes are indicated by the bins. The straight solid line is a linear least-squares fit to the data points; the dashed lines are the $1\sigma$ confidence bands of the fit. (b) Detail for the extrapolation into the count rate class region between 0 and 1. The two vertical lines enclose the estimated micro-channel-plate detector efficiency of $\epsilon = 0.25(10)$. The labeled points represent the upper and lower bounds of the extrapolated cyclotron frequency.

at an ion energy of about 1 keV is estimated to be only $\epsilon = 0.25(10)$ [Ober1997]. This means that when a single ion is observed in the trap, about four ions were actually present on average. Therefore, the linear fit must be extrapolated beyond unity.

Figure 3.5(b) shows how the extrapolated cyclotron frequency and its uncertainty are obtained from the fit. The open points represent the upper and lower bounds $\nu_{\max}$ and $\nu_{\min}$ of the extrapolated cyclotron frequency. The corrected frequency and its uncertainty are then calculated from

$$\nu = \frac{\nu_{\max} + \nu_{\min}}{2} \tag{3.3}$$

and

$$s(\nu) = \frac{\nu_{\max} - \nu_{\min}}{2}\,, \tag{3.4}$$

which for the example of Fig. 3.5 results in a relative uncertainty of $s(\nu)/\nu = 1.5 \cdot 10^{-8}$.

### 3.4.2 Cyclotron frequency of the reference ion

The magnitude of the magnetic field in the precision Penning trap varies with time. The following mechanisms for a change in the magnetic-field magnitude of a superconducting magnet have been identified:

1. The current in the superconducting coils of the magnet decreases steadily due to a phenomenon called flux creep [Ande1962, Ande1964]. It occurs when flux lines, which are pinned to inhomogeneities of the superconducting material, jump from one pinning site to another. The decrease of the field due to the viscous drag force that results from this phenomenon follows a logarithmic decay of the form $[1 - d\ln(t/\tau_0)]$, where $d$ and $\tau_0$ are phenomenological parameters [Kett1999]. Over short time intervals (up to years), this logarithmic decay can be approximated by a linear decrease.

2. When ferromagnetic or paramagnetic materials are brought within a short distance of a few meters or less of the magnet, they are magnetized. This magnetization removes energy from the field of the magnet. For large metallic objects such as the crane in the ISOLDE hall, the resulting field jumps can be of the order of $10^{-7}$. This effect is easily avoided during measurements by locking the crane in a remote location of the hall and otherwise avoiding to handle ferromagnetic or paramagnetic objects near the magnets.

3. The pressure of the recovery line for evaporated gaseous helium is subject to fluctuations. This directly determines the boiling point of the liquid helium and thus influences its temperature and that of all materials in direct contact with it, including insulator material in the high-magnetic-field region. The temperature dependence of the magnetic permeability of these materials then causes fluctuations in the magnitude of the magnetic field inside the trap [VanD1992].

4. The temperature in the warm bore of the superconducting magnet fluctuates with the temperature of the experimental hall. The magnetic permeability of all materials surrounding the Penning trap, such as the stainless-steel vacuum chamber, varies

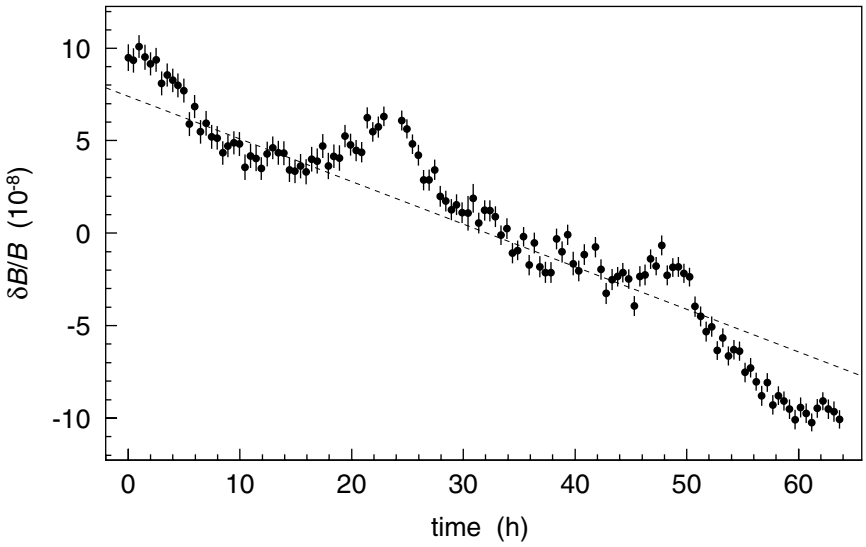


Figure 3.6: Relative change of the magnetic-field magnitude in the precision trap over a time of more than 60 hours. Both the steady decrease and the superimposed random fluctuations can be observed. The measured slope of the slow decay given by Eq. (3.5) is indicated by the dashed line.

with temperature as well, and this also has an effect on the magnetic-field magnitude. An effort to stabilize both the temperature in the warm bore and the pressure in the helium Dewar vessel of the SMILETRAP setup has proven successful in reducing the short-term magnetic-field fluctuations [Berg2002].

In the case of the magnet of ISOLTRAP's precision trap, the total relative field decay has been measured over a period of about 40 days to be

$$\frac{\delta B}{\delta t} \cdot \frac{1}{B} = -2.3 \cdot 10^{-8}/\mathrm{h}\,. \tag{3.5}$$

Figure 3.6 shows the relative change in the magnetic-field magnitude in the precision trap over an interval of more than 60 hours. The data were obtained by a continuous measurement of the cyclotron frequency of one single species of ions, in this case $^{85}Rb^{+}$. Both the long-term trend and the short-term fluctuations can be observed. It can be seen that the random fluctuations are of the same order of magnitude as the steady decay. In this run as well as in some others, there appears to be a 24-hour periodicity in the short-term fluctuations which can be explained by day-night temperature changes in the ISOLDE hall. This effect is, however, not regular enough to allow it to be corrected for. It must be taken into account by the addition of an uncertainty.

Because of the time dependence of the magnetic field, the cyclotron frequencies of the two ions should be measured in as short an interval as possible. Therefore, one reference measurement is carried out just before and one just after the actual measurement. The cyclotron frequency of the reference ion is then interpolated to the time of the actual

Table 3.1: Relative standard deviation of the magnetic-field magnitude $B$ about the interpolated value $B_{\text{int}}$ for different time intervals $\Delta T$ between the two reference measurements, obtained via cyclotron frequency measurements of $^{85}Rb^{+}$.

| $\Delta T$ (min) | $\frac{s(B - B_{\text{int}})}{B}$ |
|---|---|
| 60 | $6.3 \cdot 10^{-9}$ |
| 120 | $6.7 \cdot 10^{-9}$ |
| 180 | $1.1 \cdot 10^{-8}$ |
| 240 | $1.3 \cdot 10^{-8}$ |
| 300 | $2.1 \cdot 10^{-8}$ |

measurement. The linear interpolation represents a weighted mean that gives a stronger weight to the reference that is closer to the measurement of the ion of interest. On average, it also takes into account the slow decay of the magnetic field. The reliability of this interpolation obviously decreases with the time that elapses between the two reference measurements. This additional uncertainty, which must be added to the confidence interval of the interpolation, corresponds to the erratic component of the magnetic-field change.

In order to determine the deviation of the magnetic field from the linear decrease, we have conducted a series of long-term measurements such as the one shown in Fig. 3.6. In these tests, care was taken to accumulate a maximum of statistics by using a fairly high number of ions in the trap at a time ($\approx$ 20 counts). For the analysis, the data files were later subdivided into segments that simulate complete measurements consisting of two references and one simulated measurement of the ion of interest. The deviation of the measured cyclotron frequency from the expected value obtained from the linear interpolation of the two simulated reference measurements is then a measure for the non-linearity of the magnetic-field drift.

The relative standard deviation $s(B - B_{\text{int}})/B$ of the magnetic-field magnitude $B$ about the interpolated value $B_{\text{int}}$ as a function of the time $\Delta T$ elapsed between the two reference measurements[2] is shown in Tab. 3.1. For reasons of simplicity, the duration of each of the reference measurements was always chosen to be about 15 minutes, which is the typical duration of reference measurements in on-line experiments. Figure 3.7 is a graphical representation of these data. The data points agree well with a fitted straight line that by definition has to go through the origin. The fit yields the slope of the linear time dependence of the standard deviation. Because of the proportionality of $B$ and $\nu$ for an ion with given mass and charge that follows from Eq. (2.1), this same time dependence also governs the additional standard uncertainty $u_B(\nu_{\text{ref}})/\nu_{\text{ref}}$ of the cyclotron frequency of the

[2] $\Delta T$ is understood to mean the time difference between the centers of the two measurements. The definition is chosen in this way in order to allow the linear fit of the data to be constrained to pass through the origin.

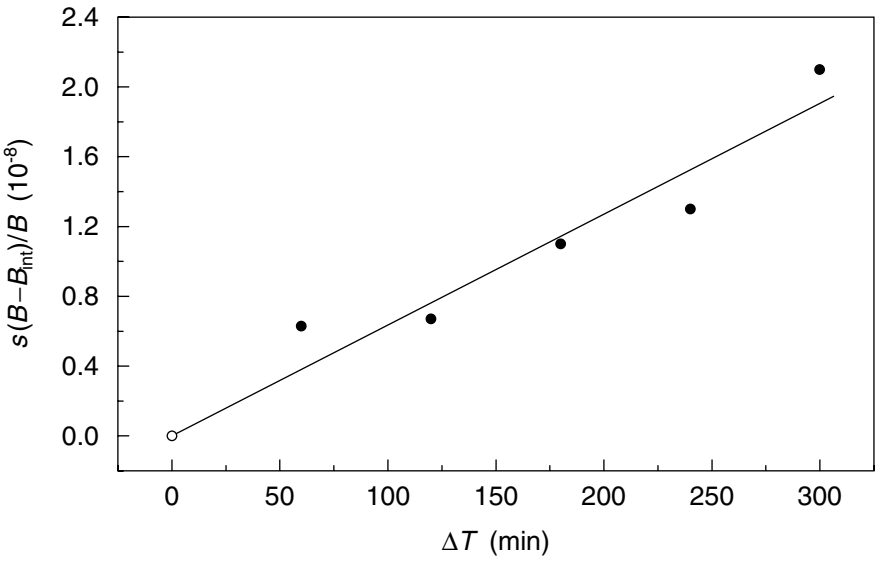


Figure 3.7: A graphical representation of the data from Tab. 3.1. The straight line is a linear fit to the data points constrained to go through the origin. Since the data points represent the standard deviation of a measured quantity, they cannot be assigned an uncertainty and thus have no error bar.

reference ion due to magnetic-field fluctuations:

$$\frac{u_B(\nu_{\mathrm{ref}})}{\nu_{\mathrm{ref}}} = 6.35(45) \cdot 10^{-11}/\mathrm{min} \cdot \Delta T \,. \tag{3.6}$$

This result bears as a consequence for high-precision mass measurements that the total duration of the measurement must be kept as short as possible. In experiments using radionuclides whose production rates are very low, the time required for collecting sufficient statistics for a cyclotron frequency determination can in some cases be as long as several hours. In those instances, a comparatively large uncertainty contribution due to magnetic-field fluctuations can be avoided by interrupting the on-line measurement and quickly obtaining a reference.

### 3.4.3 Cyclotron frequency ratio

#### Cross-reference measurements

Over a time of about three months, more than one hundred cross-reference measurements with carbon clusters were conducted with ISOLTRAP. In three series of measurements, the singly charged ions of $C_{10}$, $C_{12}$, and $C_{20}$ were in turn used as reference ions. All singly charged carbon clusters $^{12}C_n^+$ with $6 \leq n \leq 20$ were used as simulated ions of interest. The ion-optical elements along the path of the carbon cluster ions were optimized to a mass of about 100 u at the beginning of this study. This, together with low production rates [as

seen in Fig. 3.3(a)], caused the count rates of clusters with $n < 6$ and $n > 20$ to be too low for cyclotron frequency determinations within a reasonable amount of time. This is not a principal limitation of the apparatus, however, and can be adjusted in future experiments.

For each individual TOF resonance, about 3000 counts were recorded. The duration of the quadrupolar excitation was varied between 900 ms and 3 s, corresponding to resolving powers between $6 \cdot 10^5$ and $3 \cdot 10^6$; the relative statistical uncertainty $s(\nu)/\nu$ in the determination of the cyclotron frequency was a few $10^{-8}$ for each single measurement. Depending on the production rates and the excitation times, each resonance took between 15 min and 3 h. A count rate dependence of the cyclotron-frequency determination was not observed with carbon clusters. This indicates that all isobaric contaminant ions as well as clusters containing the second most abundant isotope $^{13}C$ were successfully removed in the cooling trap.

The molecular binding energies of the carbon clusters, which are of the order of $|V_b|/(mc^2) \approx 10^{-9}$, cannot be entirely neglected in a high-precision study. However, theoretical calculations suggest a smooth behavior of the binding energies with magnitudes between 5.6 and 7 eV per atom for the clusters $C_n$ with $6 \leq n \leq 20$ [Egge1994, Manb2001]. Therefore, under the assumption that the molecular binding energy *per atom* is approximately constant, its contribution to the cluster ion mass cancels out in the calculation of a cyclotron frequency ratio.

For each individual measurement, the standard uncertainty $u(r)$ of the measured cyclotron frequency ratio, including the uncertainty due to magnetic-field fluctuations according to Eq. (3.6), and its deviation $\varepsilon(r) = r - r_{th}$ from the true value were determined. Figure 3.8 shows the result of the 114 measurements in the form of ideograms. An ideogram is obtained by associating with each individual measurement a Gaussian distribution whose width $\sigma$ is equal to the relative standard uncertainty $u_c(r)$ of the measurement [Agui1986]. The area assigned to each individual measurement was chosen as proportional to the weight $1/u_c^2(r)$. The ideogram for one cluster is then the sum of the Gaussian distributions for that cluster. Several different symbols in the ideogram of one carbon cluster represent measurements with different reference ions; the dashed vertical line is the weighted mean of all measurements for a given cluster.

These ideograms show that in all cases in which a sufficient number of measurements was performed, the distribution of the individual measurements is nearly Gaussian. The only exception is that of $C_6$ with only four data points. Furthermore, Fig. 3.8 graphically shows that the distribution of the individual measurements for a given cluster and the deviations of the weighted means from the true values are all at the level of a few parts in $10^{-8}$, as would be expected from the uncertainties, shown as error bars in the figure.

### Mass-dependent systematic effect

Another way of representing the entire set of the cross-reference measurements is depicted in Fig. 3.9. Here, the data points represent the weighted means of all individual measurements as a function of the mass difference $m - m_{ref}$ between the two carbon clusters involved. The error bars are the uncertainties of the weighted means. As would be expected considering the enormous mass region that is spanned by these data, the figure shows the presence of a mass-dependent systematic effect. By use of a linear fit to the

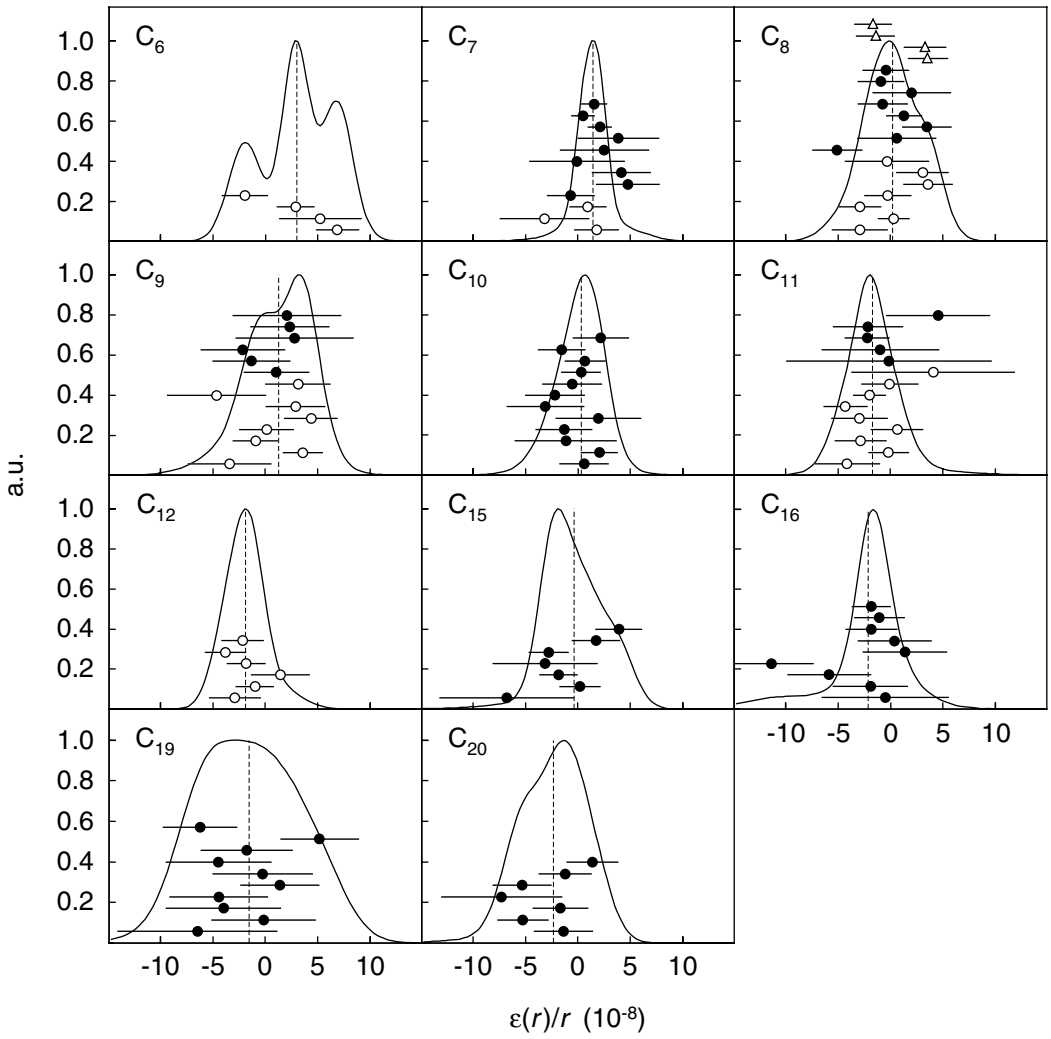


Figure 3.8: Ideograms of all 114 cluster cross-reference measurements. The different symbols represent measurements with different reference ions: $C_{10}^+$ (empty circles), $C_{12}^+$ (filled circles), and $C_{20}^+$ (empty triangles).

data, which by definition was constrained to pass through the origin, the magnitude of the effect was determined to be

$$\frac{\varepsilon_{\mathrm{m}}(r)}{r} = -1.6(4) \cdot 10^{-10}/\mathrm{u} \cdot (m - m_{\mathrm{ref}})\,. \tag{3.7}$$

A mass-dependent frequency ratio shift can be due to imperfections of the electric-quadrupole field or a misalignment of the precision trap's electrostatic trapping fields with respect to the magnetic-field axis [Brow1986, Boll1996]. The upper bound of the magnitude of these effects has previously been estimated [Beck1997b] to be $|\varepsilon_{\mathrm{m}}(r)|/r = 2 \cdot 10^{-9}/\mathrm{u} \cdot (m - m_{\mathrm{ref}})$.

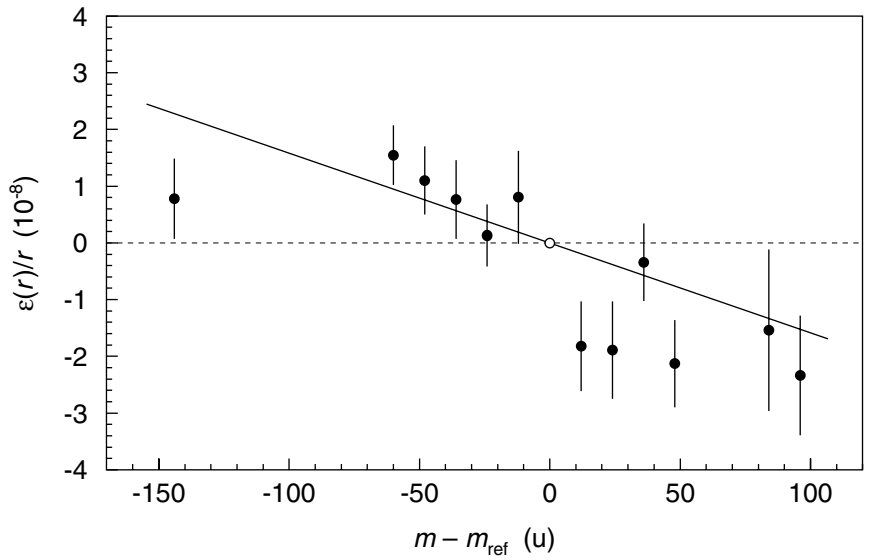


Figure 3.9: Deviation of the weighted mean frequency ratios of all carbon cluster cross-reference measurements as a function of the mass difference $m - m_{\mathrm{ref}}$ between reference ion and ion of interest. The straight line is a linear least-squares fit to the data. The carbon cluster ions $C_{10}^+$, $C_{12}^+$, and $C_{20}^+$ were used as reference ions.

Since the factors contributing to the mass-dependent effect are not completely controllable, it is believed that its magnitude may change in future measurements due to small changes in electrostatic potentials or other trapping parameters. However, the magnitude of the effect did not appear to vary greatly, if at all, during the approximately three months which this study lasted. It was nevertheless decided not to correct for it in evaluating actual measurements, but instead to add a relative standard uncertainty which has the same magnitude:

$$\frac{u_{\mathrm{m}}(r)}{r} = 1.6 \cdot 10^{-10}/\mathrm{u} \cdot (m - m_{\mathrm{ref}})\,. \tag{3.8}$$

This equation shows the importance of choosing a reference ion whose mass is as close as possible to the mass of the ion of interest. In most past measurements, it was possible to keep $m - m_{\mathrm{ref}}$ below 20 u and thus the total relative effect below $5 \cdot 10^{-9}$.

### Residual systematic uncertainty

At the time of the carbon cluster cross-reference measurements, the mass-dependent effect was clearly identified and its magnitude determined. The effect can therefore be corrected for, albeit only for this particular series of measurements. The result of this correction is shown in Fig. 3.10. In this figure, the weighted means of all individual cross-reference measurements are shown as a function of the mass of the simulated ion of interest. The error bars represent the experimental uncertainties of the weighted means. Clearly, these results now agree better with the true values, represented by the solid horizontal line.

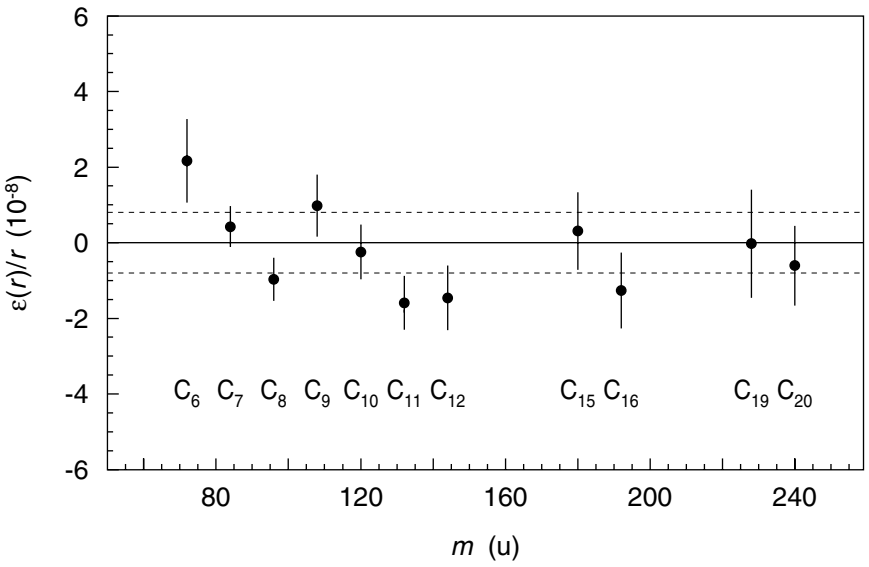


Figure 3.10: Deviations of the weighted means of the cyclotron frequency ratios for all carbon cluster cross-reference measurements from their true value after correction for the mass-dependent effect by use of Eq. (3.7). The dashed lines indicate the residual systematic uncertainty that must be added to the uncertainties of the mean values in order to obtain a reduced $\chi^2$ that obeys the condition $\chi^2/N \leq 1$.

The $\chi^2$ of the experimental distribution of the cyclotron frequency ratios for each carbon cluster were then calculated according to the following formula:

$$\chi^2 = \sum_i \left[ \frac{\varepsilon(r^i)}{u(r^i)} \right]^2 , \tag{3.9}$$

where $\varepsilon(r^i) = r^i - r_{\mathrm{th}}$ is the deviation of the measured frequency ratio from its known true value $r_{\mathrm{th}}$ and $u(r^i)$ is the experimental standard uncertainty of the frequency ratio.

After correction for the mass-dependent effect by use of Eq. (3.7), the reduced $\chi^2$ of the distribution of the individual frequency ratios about their true values[3] for all 114 cross-reference measurements shown in Fig. 3.8 is $\chi^2/N = 0.96$. This indicates that the relative standard uncertainty $u_B(\nu_{\mathrm{ref}})/\nu_{\mathrm{ref}}$ due to the magnetic-field fluctuations was correctly determined and taken into account.

If for the individual data contributing to the mass value of one cluster size the weighted means are calculated as plotted in Fig. 3.10, it becomes obvious that an additional systematic effect is still present. The reduced $\chi^2$ of the distribution of the mean frequency ratios for all eleven carbon cluster species was therefore calculated and found to be $\chi^2/N = 2.02$. The fact that the reduced $\chi^2$ is considerably greater than 1 confirms the presence of a residual systematic effect. Its magnitude can be determined from the condition $\chi^2/N \leq 1$ to

[3]For the calculation of the reduced $\chi^2$, the relation $\chi^2/N$ was used since in Eq. (3.9) no degree of freedom was lost in the calculation of a mean value.

be

$$\frac{u_{\mathrm{res}}(r)}{r} = 8 \cdot 10^{-9}\,. \tag{3.10}$$

This uncertainty also constitutes the limit of mass accuracy of the ISOLTRAP experiment because all other uncertainties, being statistical in nature, can be reduced by an increased number of repeated measurements. This new limit is more than an order of magnitude smaller than the systematic uncertainty previously added to the final results.

## 3.5 Evaluation procedure

In the previous section, all identified effects that contribute to the uncertainties of the measured quantities were presented. Based on these results, the evaluation procedure applied to the data of on-line experiments was adapted. The new procedure is outlined in the following.

### 3.5.1 Individual cyclotron frequencies of the ion of interest

For all TOF resonances recorded with ions that are potentially subject to contamination, *i.e.* all ions delivered by ISOLDE, the cyclotron frequencies are determined using a count rate class analysis. The cyclotron frequencies $\nu^i$ of the individual measurements and their uncertainties $u(\nu^i)$ are determined according to the procedure described in 3.4.1.

### 3.5.2 Individual cyclotron frequencies of the reference ion

For each TOF resonance of the ion of interest recorded at time $t_1$, the cyclotron frequency of the reference ion is determined from the two references just before and just after it (times $t_0$ and $t_2$). All times are understood to mean the center of the interval between the beginning and the end of a TOF resonance measurement. Using the least-squares method, the cyclotron frequency of the two measurements are interpolated to $t_1$, yielding the cyclotron frequency $\nu_{\mathrm{ref}}$ of the reference ion.

For a linear least-squares fit of only two data points, closed formulas are available which allow the calculation of the interpolated cyclotron frequency $\nu^i_{\mathrm{ref}}(t_1)$ and its experimental standard deviation $s(\nu^i_{\mathrm{ref}})(t_1)$:

$$\nu^i_{\mathrm{ref}}(t_1) = t_1 \cdot \frac{\nu_2 - \nu_0}{t_2 - t_0} + \frac{t_2\nu_0 - t_0\nu_2}{t_2 - t_0} \tag{3.11}$$

and

$$s(\nu^i_{\mathrm{ref}})(t_1) = \frac{\sqrt{2\left[t_0^2 s_2^2 + t_2^2 s_0^2 - 2t_1\left(t_0 s_2^2 + t_2 s_0^2\right) + t_1^2\left(s_0^2 + s_2^2\right)\right]}}{t_2 - t_0}\,, \tag{3.12}$$

where $\nu_k$ is shorthand for $\nu^i_{\mathrm{ref}}(t_k)$ and $s_k$ for $s(\nu^i_{\mathrm{ref}})(t_k)$.

The combined relative standard uncertainty of the cyclotron frequency of the reference ion at time $t_1$ is found by quadratically adding the experimental relative standard deviation

from Eq. (3.12) and the relative standard uncertainty due to the fluctuation of the magnetic field $u_B(\nu^i_{\mathrm{ref}})/\nu^i_{\mathrm{ref}}$ which is calculated according to Eq. (3.6):

$$\frac{u_{\mathrm{c}}(\nu^i_{\mathrm{ref}})}{\nu^i_{\mathrm{ref}}} = \sqrt{\left[\frac{s(\nu^i_{\mathrm{ref}})}{\nu^i_{\mathrm{ref}}}\right]^2 + \left[\frac{u_B(\nu^i_{\mathrm{ref}})}{\nu^i_{\mathrm{ref}}}\right]^2}\,. \tag{3.13}$$

### 3.5.3 Cyclotron frequency ratios

For all individual measurements of a given ion species, the cyclotron frequency ratios $r^i$ and their combined relative uncertainties $u_{\mathrm{c}}(r^i)/r^i$ are calculated according to:

$$r^i = \frac{\nu^i_{\mathrm{ref}}}{\nu^i} \tag{3.14}$$

and

$$\frac{u_{\mathrm{c}}(r^i)}{r^i} = \sqrt{\left[\frac{s(\nu^i)}{\nu^i}\right]^2 + \left[\frac{u_{\mathrm{c}}(\nu^i_{\mathrm{ref}})}{\nu^i_{\mathrm{ref}}}\right]^2}\,. \tag{3.15}$$

In the case that two or more measurements of one species of ions were made during the same on-line experiment, the weighted mean $\bar{r}$ of the frequency ratio and its relative standard uncertainty $u(\bar{r})/\bar{r}$ are calculated:

$$\bar{r} = \frac{\sum_i \frac{r^i}{u^2_{\mathrm{c}}(r^i)}}{\sum_i \frac{1}{u^2_{\mathrm{c}}(r^i)}} \tag{3.16}$$

and

$$\frac{u(\bar{r})}{\bar{r}} = \frac{1}{\bar{r}\sqrt{\sum_i \frac{1}{u^2_{\mathrm{c}}(r^i)}}}\,. \tag{3.17}$$

The combined relative standard uncertainty of the mean frequency ratio is found by adding to the relative standard uncertainty calculated by use of Eq. (3.17) the relative uncertainty due to the mass-dependent systematic effect $u_{\mathrm{m}}(\bar{r})/\bar{r}$ and the residual relative uncertainty $u_{\mathrm{res}}(\bar{r}/\bar{r})$:

$$\frac{u_{\mathrm{c}}(\bar{r})}{\bar{r}} = \sqrt{\left[\frac{u(\bar{r})}{\bar{r}}\right]^2 + \left[\frac{u_{\mathrm{m}}(\bar{r})}{\bar{r}}\right]^2 + \left[\frac{u_{\mathrm{res}}(\bar{r})}{\bar{r}}\right]^2}\,, \tag{3.18}$$

where $u_{\mathrm{m}}(\bar{r})/\bar{r}$ is calculated according to Eq. (3.8) and $u_{\mathrm{res}}(\bar{r})/\bar{r}$ is given by Eq. (3.10).

# 4 Mass measurements of neutron-deficient Rb and Kr isotopes

## 4.1 Experimental procedure and results

The data presented here were collected during two distinct data taking periods in October 2000 that lasted about one week each. For the production of the krypton isotopes, a zirconium oxide target was used in combination with a hot-plasma ion source. A certain degree of chemical selectivity was achieved by cooling the transfer line between the target and the ion source. The rubidium isotopes were produced from a niobium foil target in conjunction with a tungsten surface ionization ion source. Both targets were bombarded with proton pulses containing up to $3 \cdot 10^{13}$ protons each at kinetic energies of 1.0 or 1.4 GeV. The high-resolution separator (HRS) of ISOLDE, which was used for both these data taking periods, was operated at a mass resolving power of $m/\delta m \approx 4000$.

Except for $^{74}$Rb, all nuclides under investigation have half-lives longer than 25 s. They were measured using RF excitation times in the precision Penning trap of 300 to 1800 ms. In the special case of $^{74}$Rb with a half-life of only 65 ms, a very short measurement cycle, such as that already used for $^{33}$Ar had to be employed [Herf2001c]. In that scheme, the total cycle time from the injection of the ions into the RFQ ion beam cooler and buncher to the mass measurement takes less than 200 ms. The duration of the RF excitation was varied between 60 and 120 ms, corresponding to mass resolving powers of $m/\delta m \approx 80\,000$ to 160 000.

The reference measurements were carried out with the stable nuclide $^{85}$Rb produced in ISOLTRAP's reference ion source. An RF excitation time of 900 ms was chosen, yielding a mass resolving power of about $10^6$. References were obtained between all measurements, thereby minimizing the uncertainty due to magnetic-field fluctuations (see Chap. 3). To achieve the highest possible precision for the mass of $^{74}$Kr, seven individual measurements were carried out. The intervals between reference measurements were kept below 3 hours for all of them.

In order to exclude systematic shifts caused by unknown sources, the masses of five other nuclides with rather well-known masses were also measured: $^{75}$As and $^{133}$Cs during the krypton data taking period and $^{74}$Ga, $^{88}$Sr, and $^{133}$Cs during the rubidium data taking period. They were found in good agreement with the literature values. In fact, in the case of $^{74}$Ga, the uncertainty of the literature value was improved by more than a factor of three and the ISOLTRAP measurement now fully determines its mass excess.

The $^{74}$Rb measurement with a mass uncertainty of 18 keV falls somewhat short of the uncertainty of 10 keV that had been aimed for. The transmission of the ISOLTRAP apparatus was particularly low ($< 10^{-4}$) during that experiment due to a misalignment of the beam line, leading to a shortfall in the statistics. During more than 33 hours of measurement time, a total of 550 $^{74}$Rb ions were detected. Reference measurements were carried out about every 6 hours.

Table 4.1: Half-lives $T_{1/2}$ (from NUBASE [Audi1997]) and measured cyclotron frequency ratios $r = \nu_{c,ref}/\nu_c$ for the nuclides measured during the Kr (first set) and Rb (second set) data taking periods in 2000. In all cases, $^{85}$Rb was used as the reference mass. The experimental masses $m$ from the ISOLTRAP measurements and their relative uncertainties were calculated according to Eq. (2.3) using current values for the mass of $^{85}$Rb, the electron mass, and the unified atomic mass unit, all given in the text. The RF excitation times $T_{RF}$ and the total number of detected ions $N_{tot}$ are also shown. Uncertainties (in parentheses) refer to the least significant digits of a quantity. The uncertainties of the frequency ratios are given to three figures to reduce rounding errors in subsequent calculations such as the atomic-mass evaluation.

| Nucl. | $T_{1/2}$ | $T_{RF}$ (ms) | $N_{tot}$ | $r$ | $m$ (u) | $u(m)/m$ |
|---|---|---|---|---|---|---|
| $^{73}$Kr | 28.6 s | 300 | 107 | 0.858 999 829(114) | 72.939 2902(97) | $1.3 \cdot 10^{-7}$ |
| $^{74}$Kr | 11.5 min | 300[a] | 11 298 | 0.870 703 7618(303) | 73.933 0857(26) | $3.5 \cdot 10^{-8}$ |
| $^{75}$As | *stable* | 300 | 1969 | 0.882 345 4661(889) | 74.921 5972(76) | $1.0 \cdot 10^{-7}$ |
| $^{75}$Kr | 4.29 min | 300 | 1492 | 0.882 455 563(102) | 74.930 9457(86) | $1.2 \cdot 10^{-7}$ |
| $^{76}$Kr | 14.8 h | 300[a] | 3433 | 0.894 173 3117(557) | 75.925 9143(47) | $6.2 \cdot 10^{-8}$ |
| $^{77}$Kr | 74.4 min | 300 | 35 639 | 0.905 935 6611(248) | 76.924 6700(21) | $2.7 \cdot 10^{-8}$ |
| $^{78}$Kr | *stable* | 300[a] | 64 604 | 0.917 661 9688(159) | 77.920 3653(13) | $1.7 \cdot 10^{-8}$ |
| $^{80}$Kr | *stable* | 1400[a] | 11 510 | 0.941 169 0366(199) | 79.916 3796(17) | $2.1 \cdot 10^{-8}$ |
| $^{82}$Kr | *stable* | 900[a] | 9032 | 0.964 688 9212(305) | 81.913 4822(27) | $3.3 \cdot 10^{-8}$ |
| $^{133}$Cs | *stable* | 300 | 6862 | 1.565 221 5360(792) | 132.905 4519(67) | $5.1 \cdot 10^{-8}$ |
| $^{74}$Ga | 8.12 min | 120 | 104 | 0.870 631 490(265) | 73.926949(22)[b] | $3.0 \cdot 10^{-7}$ |
| $^{74}$Rb | 64.8 ms | 120[a] | 550 | 0.870 835 571(226) | 73.944278(19) | $2.6 \cdot 10^{-7}$ |
| $^{76}$Rb | 36.5 s | 90[a] | 15 286 | 0.894 281 1649(232) | 75.9350722(20) | $2.6 \cdot 10^{-8}$ |
| $^{88}$Sr | *stable* | 90 | 3258 | 1.035 258 054(233) | 87.905595(20) | $2.2 \cdot 10^{-7}$ |
| $^{133}$Cs | *stable* | 1800 | 15 758 | 1.565 221 5168(190) | 132.9054503(16) | $1.2 \cdot 10^{-8}$ |

[a] Other excitation time(s) also used.
[b] An isomeric contamination cannot be excluded. See 4.2.1 for details.

All cyclotron frequency ratios of the two data taking periods are given in Tab. 4.1. The half-lives of the nuclides (from NUBASE [Audi1997]) are indicated in the second column; the measured cyclotron frequency ratios are shown in the fifth column. In addition, the RF excitation time $T_{RF}$ and the total number of detected ions $N_{tot}$ are given.

From the primary result of an ISOLTRAP mass measurement, the cyclotron frequency ratio $r$, the atomic mass $m$ of the studied nuclide can be calculated according to Eq. (2.3) using the currently best available values for the masses of the reference atom $m_{ref}$ and the mass of the electron $m_e$. The values that were used in the calculation of the results presented here are[1] $M(^{85}\text{Rb}) = 84.911\,789\,738(12)$ u [Brad1999, Audi2002],

[1] The unit V used here is the standard volt rather than the international volt. For a justification, see [Audi2001].

$m_e$ = 510.998 902(21) keV [Mohr1999], and 1 u = 931 494.009(7) keV [Audi2001]. The mass thus obtained and its relative uncertainty are shown in the sixth and seventh column of Tab. 4.1.

The relative uncertainties that were achieved range from $1.2 \cdot 10^{-8}$ to $3.0 \cdot 10^{-7}$. In most cases, they are not yet limited by the residual systematic uncertainty of $8.0 \cdot 10^{-9}$ that was found in Chap. 3. This means that with better statistics, an improvement by ISOLTRAP of almost all these measurements is still possible. This is especially true for $^{74}$Rb, where a reduction of the mass uncertainty by as much as a factor of five could be achieved in future measurements.

## 4.2 Atomic-mass evaluation

The mass excess $D$ of a nuclide is defined by the relation

$$D = m - A \text{ u}, \tag{4.1}$$

where $A$ is the atomic mass number of the nuclide, $m$ is its atomic mass, and u is the unified atomic mass unit which is in turn defined as 1/12 of the atomic mass of the most abundant carbon isotope $^{12}$C. The mass excesses of all known nuclides are tabulated in the Atomic-Mass Evaluation (AME), which is constantly updated and published every few years [Audi1993, Audi1995]. It is the result of a least-squares adjustment of all available experimental data on mass measurements and decay and reaction energies.

Only in a very small minority of mass measurements does the measured quantity connect the mass of the studied nuclide directly to $^{12}$C, the microscopic mass standard. In these so-called absolute mass measurements, the mass of the reference ion is exactly known and doesn't contribute to the uncertainty of the final result. In most cases, however, a measurement supplies a value for the mass difference between any two nuclides; sometimes more than two nuclides are involved, for instance when the calibration is explicitly treated as part of the measured quantity. For the purpose of the AME, the frequency ratios of the ISOLTRAP mass results must be expressed as linear equations. The exact procedure for this transformation is described in detail in [Otto1993].

The ensemble of these connections spans a web of mass relations over the entire chart of the nuclides; mathematically, they represent an over-determined set of linear equations. Before the least-squares optimization is carried out, some similar measurements between the same nuclides are pre-averaged. Some others, which have been superseded by measurements with a much smaller uncertainty, are labeled as "weight much less than that of a combination of other data." These equations are not used for the following step of the evaluation. As the central step in the AME, a least-squares analysis is carried out on the remaining several hundred linear equations.

### 4.2.1 Treatment of the input values

An overview of the difference between the Kr and Rb mass measurements presented here (Tab. 4.1) and the literature values of the AME 1995 is shown in Fig. 4.1. A critical

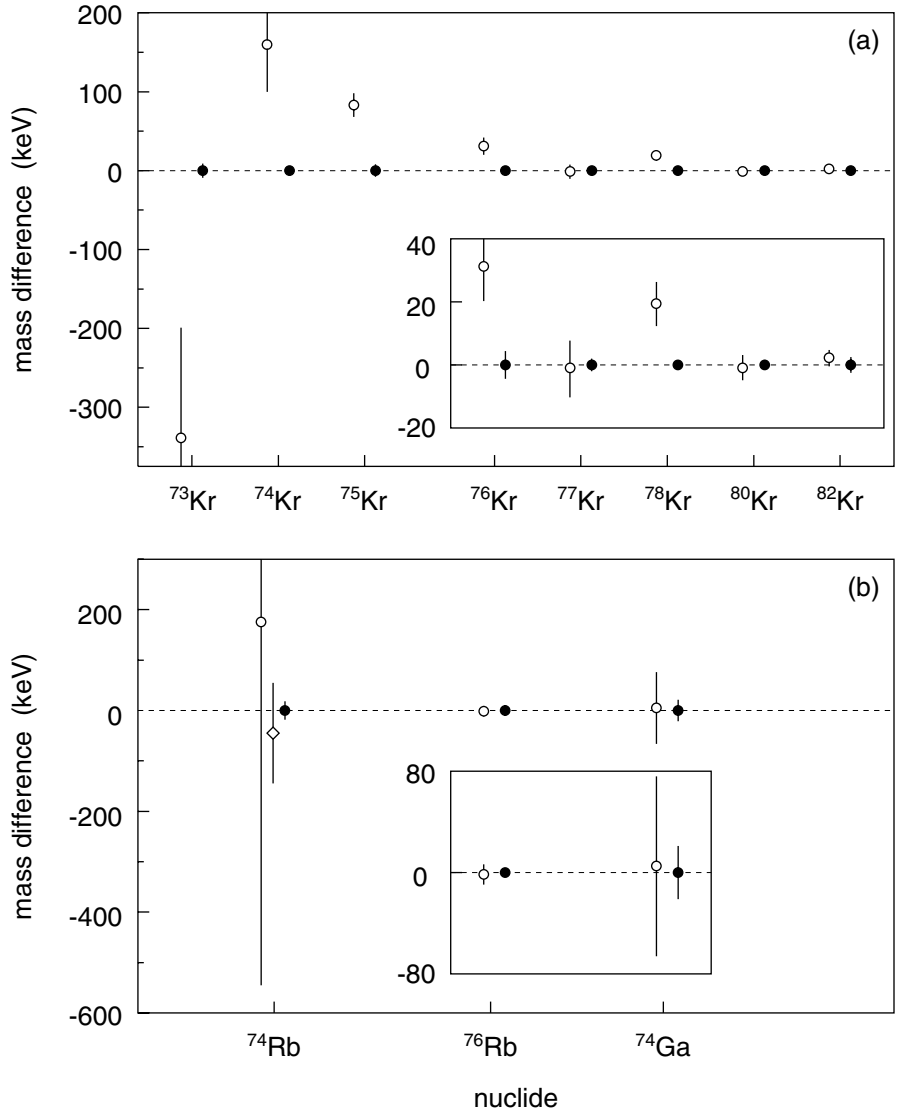


Figure 4.1: Overview of the measured mass excesses and their deviation from the values of the 1995 Atomic-Mass Evaluation: (a) Kr data taking period; (b) Rb data taking period. The empty circles are the AME 1995 and the filled circles the ISOLTRAP data. For $^{74}$Rb, the MISTRAL measurement is also shown (empty diamond; see the discussion in the text). The insets are enlarged portions of the graph where the differences or error bars are too small to be seen at full scale.

analysis of the mass data was carried out in close collaboration with G. Audi, the evaluator and editor of the mass tables. In the following, the deviations will be discussed in detail for all measured nuclides in order of mass number $A$, then proton number $Z$.

### $^{73}$Kr

The mass excess of $^{73}$Kr was determined by two experiments, one using the $^{73}$Kr($\beta^+$)$^{73}$Br decay [Schm1973] and the other the $^{73}$Kr(e,p)$^{72}$Se reaction [Hard1981]. In the work of Schmeing *et al.*, $^{73}$Kr was produced as a by-product of directing a 55-MeV $^{16}$O beam onto an enriched $^{58}$Ni target for the production of $^{72}$Kr. The energy spectrum of the positrons was recorded in coincidence with the 178-keV $\gamma$ ray from the daughter nucleus. The $\beta$ end point energy $E_0$ was measured to be 5590(350) keV, corresponding to a total decay energy[2] of $Q_{\mathrm{EC}}$ = 6790(350) keV and a mass excess of $D = -56\,740(370)$ keV.

Hardy *et al.* produced $^{73}$Kr by bombarding a $^{60}$Ni target with a 75-MeV $^{16}$O beam. They recorded the energy spectrum of the proton emitted from the intermediate highly excited $^{73}$Br state. The proton end point energy then yielded a reaction energy of $Q_{\mathrm{EC}} - B_p$ = 3700(150) keV (for an explanation of the notation, see App. B), corresponding to a mass excess of $D = -56\,850(150)$ keV.

The mass excess found in this work is 340 keV larger than the weighted average of the two previous data. It is in fact in agreement with the value from [Schm1973] and disagrees by 2.4$\sigma$ from the value of [Hard1981]. Although no apparent flaw in that work could be identified, both previous values are outweighed and the ISOLTRAP datum now completely determines the adjusted value.

### $^{74}$Ga

The nuclide $^{74}$Ga is believed to have an isomeric state with a half-life of 9.5 s and an excitation energy of 59.6 keV [Farh1995]. However, Nb foil targets are known to exhibit a slow release (minutes) for the element Ga. Furthermore, measurements of the yield of $^{74}$Ga have shown no evidence for the isomeric state whatsoever [Köst2002]. It is therefore inferred that the ISOLDE yield of the isomer is no larger than 10 % of that of the ground state. When both the ground state and an excited nuclear state of a nuclide are populated, the experimentally measured mass excess $D^*_{\mathrm{exp}}$ is shifted from the ground state value $D_{\mathrm{exp}}$ [Audi1982]:

$$D^*_{\mathrm{exp}} = D_{\mathrm{exp}} + \frac{R}{R+1} \cdot \Delta E\,, \tag{4.2}$$

where $R = Y_{\mathrm{m}}/Y_{\mathrm{g}}$ is the ratio of the yield of the nuclide in the isomeric state to that in the ground state and $\Delta E$ is the excitation energy of the isomeric state. The measured mass excess must therefore be corrected by the quantity $-R/(R+1) \cdot \Delta E$. Based on the yield estimate stated above, the ratio $R$ is presumed to follow a uniform probability distribution between 0 and 0.1 in the case of $^{74}$Ga, corresponding to a central value of 0.05

[2] The uncertainty of the total decay energy was given as 440 keV, possibly to compensate for the incomplete knowledge of the exact level scheme. For the AME, the smaller value of 350 keV from the end point determination was retained.

and a standard uncertainty of $0.05/\sqrt{3}$. The correction for the mass excess then becomes −2.8(1.6) keV, and the corrected mass excess is $D = -68\,049(21)$ keV.

The mass of $^{74}$Ga was previously determined in equal parts by beta endpoint measurements of the two $\beta^-$ decays that link the nuclide to the decay chain from $^{74}$Co to the stable $^{74}$Ge [Eich1962, Erda1972]. In the experiment of Eichler *et al.*, $^{74}$Ga was produced from the $^{74}$Ge$(n,p)^{74}$Ga reaction. The beta spectrum of the $^{74}$Ga$(\beta^-)^{74}$Ge decay was first recorded without a coincidence condition and two groups with beta endpoint energies of 2450(100) keV and 3800(300) keV were found. Using a coincidence with 2350-keV $\gamma$ rays, the lower-energy group was then identified as populating the 2950-keV level in $^{74}$Ge. This leads to a decay energy of $Q_{\beta^-} = 5400(100)$ keV, corresponding to a mass excess for $^{74}$Ga of $D = -68\,020(100)$ keV.

Erdal *et al.* produced $^{74}$Zn from the $^{76}$Ge$(p,3p)^{74}$Zn reaction by bombarding a molten germanium target with 600-MeV protons and recorded the electron spectrum from the $^{74}$Zn$(\beta^-)^{74}$Ga decay in coincidence with $\gamma$ rays at 70–200 keV. From this, the beta endpoint energy was found to be $E_0 = 2100(100)$ keV. Using the additional information that the $\beta$ decay populates the 251.8-keV level in the daughter nucleus, a total decay energy of $Q_{\beta^-} = 2350(100)$ keV was deduced and entered into the AME. This corresponds to a mass excess of −68 060(110) keV.

The ISOLTRAP measurement is in excellent agreement with both these previous results. Since the ISOLTRAP datum is five times more precise than either of the older measurements, they are outweighed.

### $^{74}$Kr

The ISOLTRAP datum for the mass excess of $^{74}$Kr deviates by $2.7\sigma$ from the previously accepted value, which was determined by three measurements [Roec1974, Schm1975, Molt1982]. A comparison between the previous data, the AME 1995 value, and our result is shown in Fig. 4.2.

The most precise previous datum, obtained from a determination of the $Q$ value of the $^{78}$Kr$(^4$He,$^8$He$)^{74}$Kr reaction [Molt1982], shows a $1.4\sigma$ disagreement with the ISOLTRAP mass excess, even after taking into account the change in the $^{78}$Kr mass brought about by our measurement. The energy calibration in that experiment was obtained through the $^{64}$Ni$(^4$He,$^8$He$)^{60}$Ni reaction. Although the accepted masses of the two nuclides $^{64}$Ni and $^{60}$Ni have changed by −2.1 keV and −1.9 keV, respectively, the mass difference has remained practically unchanged and the calibration thus remains valid.

The reaction energy of $Q = 41\,120(75)$ keV, corresponding to a mass excess for $^{74}$Kr of $D = -62\,213(76)$ keV, was extracted from a gated $^8$He position spectrum which is reproduced in Fig. 4.3. The expected peak width of about 280 keV, indicated by a bracket in the figure, is correctly estimated from the energy straggling in the target, and that width is also found in the peaks of the $^6$He position spectrum observed for a different reaction in that same paper. However, the assignment of the peak with a total of only four events and the adoption of a peak centroid uncertainty of only 75 keV seem ambitious. The bin width of about 22 keV should not contribute significantly to the final uncertainty, but the poor statistics do not allow a clear assignment of the peak, if any. If, for instance, only the right peak containing three events is chosen, a reaction energy of −41 080 keV is found.

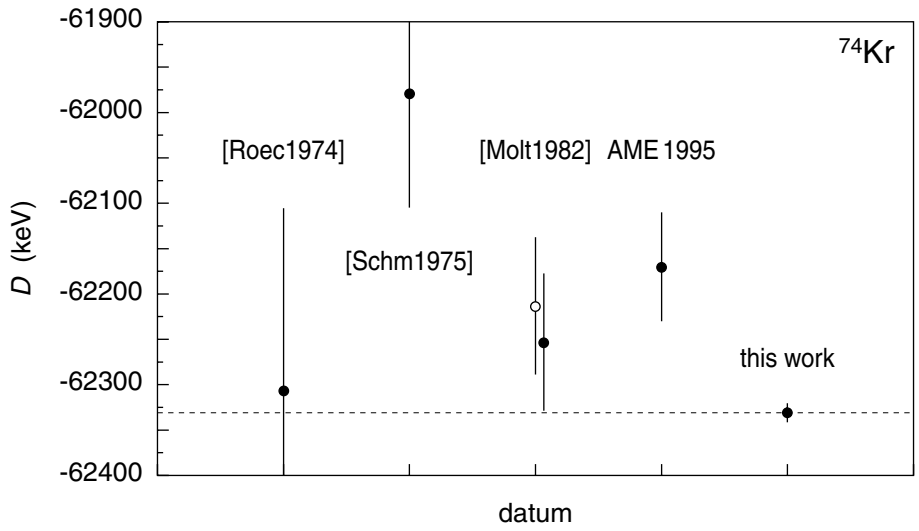


Figure 4.2: Comparison of previous measurements with the ISOLTRAP result for $^{74}$Kr. The mass excesses are calculated from the measured reaction or decay energies using the AME 1995 data for the masses of the other nuclides involved. The dashed horizontal line represents the ISOLTRAP datum. The empty and the filled circle for the measurement of [Molt1982] correspond to the original and the corrected value, respectively. See the explanation in the text.

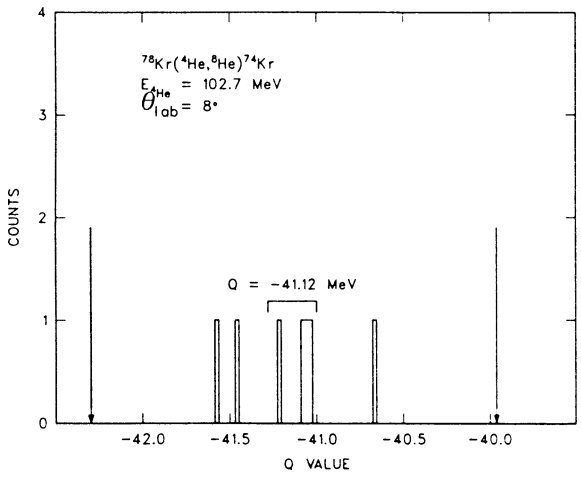


Figure 4.3: Figure 3 from [Molt1982]. The figure represents the gated $^{8}$He position spectrum from the $^{78}$Kr($^{4}$He,$^{8}$He)$^{74}$Kr reaction. The bracket indicates the four counts that were identified as stemming from the reaction. The other three are expected to be background. The abscissa of the graph is in MeV.

That $Q$ value leads to a mass excess of −62 253(76) keV, in reasonable agreement with our result. For the purpose of the AME, the datum of Moltz *et al.* was labeled with the comment "Original value for 4 events included one background event," the energy was corrected, and the value excluded from the adjustment. The original and the corrected datum are displayed in Fig. 4.2 as an empty and a filled circle, respectively.

The correction of the datum from Moltz *et al.* improves its agreement with the previous measurement from [Roec1974] and worsens the disagreement with another value [Schm1975]. Finally, considering the much smaller uncertainty of the ISOLTRAP datum, all other measurements are outweighed.

### $^{74}$Rb

The mass of $^{74}$Rb had previously been measured only once, using a mass spectrometer [Audi1982]. In fact, two separate measurements reported in that paper contribute to the $^{74}$Rb datum. The two measurements, using the triplets $^{74,75,76}$Rb and $^{74,75,77}$Rb, agree well with each other. The new ISOLTRAP mass is in very good agreement with the combined value, but improves the uncertainty by a factor of 40. A measurement also made at ISOLDE in 2000, using the transmission mass spectrometer MISTRAL, yielded a mass excess of −51 950(100) keV [Viei2002], confirming our mass using a different measurement principle. The AME 1995 value and the MISTRAL datum are shown alongside our result in Fig. 4.1(b). Due to the higher precision of our datum, the other two are outweighed.

### $^{75}$As

The stable nuclide $^{75}$As has in the past been measured by a large number of groups employing many different techniques. Out of the most precise of them [Goss1959, John1964, Zumb1982, Hoyl1990], only the mass excess obtained by Johnson *et al.* from the $Q$ value of the $^{75}$As$(p,n)^{75}$Se reaction [$D$ = −73 033.7(1.9)] deviates notably from the weighted average of −73 032.5(1.6) keV. The ISOLTRAP result agrees perfectly with the AME 1995 value, but is four times less precise.

### $^{75}$Kr

The previous value for the mass excess of $^{75}$Kr was determined by one measurement, obtained from the $^{78}$Kr($^{3}$He,$^{6}$He)$^{75}$Kr reaction [Molt1987]. The measurement, whose mass uncertainty was about three times as large as that of the new ISOLTRAP value, deviates by an enormous 4.5$\sigma$ from it. In that work, Moltz *et al.* directed a 70-MeV $^{3}$He beam onto an enriched $^{78}$Kr gas target. The position spectrum of the reaction product $^{6}$He at a scattering angle of $\theta_{\mathrm{lab}} = 7.25°$ was recorded at the focal plane of a split-pole spectrograph. The reaction $^{18}$O($^{3}$He,$^{6}$He)$^{15}$O was used for the calibration of the detector. The $^{6}$He position spectrum from Fig. 3 of [Molt1987] is shown in Fig. 4.4. The peaks labeled (1), (2), and (3) were identified as representing the population of the $7/2^-$ state at 611 keV, the $5/2^-$ state at 358 keV, and the $5/2^+$ ground state, respectively. That assignment appears to be correct, but the reported uncertainty of 14 keV seems underestimated considering that it

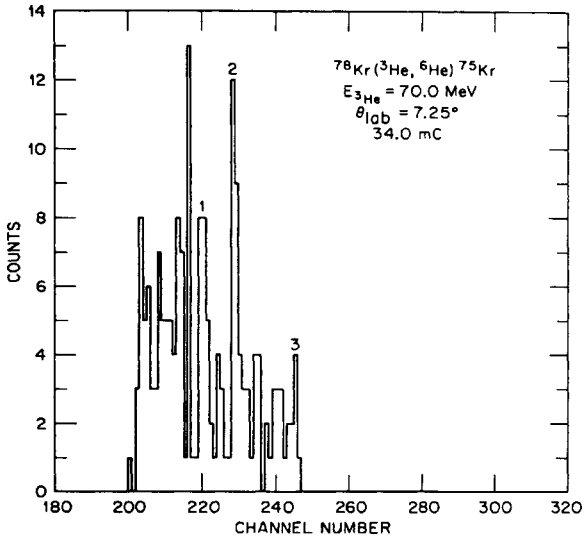


Figure 4.4: Figure 3 from [Molt1987]. The figure shows the $^{6}$He position spectrum from the $^{78}$Kr($^{3}$He,$^{6}$He)$^{75}$Kr reaction. The reported uncertainty of the reaction energy corresponds to one half channel in the figure.

corresponds to only about one half channel. The analogous measurement of the reaction energy of the $^{82}$Kr($^{3}$He,$^{6}$He)$^{79}$Kr reaction agrees well with the accepted value. The third described analogous measurement, however, that of the $^{80}$Kr($^{3}$He,$^{6}$He)$^{77}$Kr reaction, also deviates by several standard deviations from the current value. This supports the assumption that the uncertainties were underestimated. Interestingly, although the statistics seem to be very similar for all three measurements, the uncertainty assigned to the $Q$ value of the $^{78}$Kr($^{3}$He,$^{6}$He)$^{75}$Kr reaction is much smaller than that of the two other measurements. The datum from Moltz *et al.* is excluded from the adjustment.

### $^{76}$Kr

The mass of $^{76}$Kr was determined at 31 % by a measurement of the reaction energy of $^{78}$Kr($p$,$t$)$^{76}$Kr [Mats1981] and at 69 % from the $Q$ value of the $^{78}$Kr($^{4}$He,$^{6}$He)$^{76}$Kr reaction [Molt1982]. These two measurements had a very good internal consistency of $\pm 0.1\sigma$.

The new ISOLTRAP value is in acceptable agreement ($1.0\sigma$ deviation) with the ($p$,$t$) datum of Matsuki *et al.*, but it deviates by $1.7\sigma$ from the original datum of Moltz *et al.* A closer study of that paper revealed that the $Q$ value was in fact measured on a relative scale, with respect to that of the $^{80}$Kr($^{4}$He,$^{6}$He)$^{78}$Kr reaction. This means that the measurement really connects the three masses of $^{80}$Kr, $^{78}$Kr, and $^{76}$Kr. The $Q$ values of the two ($^{4}$He,$^{6}$He) reactions are (see App. B for a derivation of these relations):

$$Q_1 = D(^{80}\mathrm{Kr}) - D(^{78}\mathrm{Kr}) + D(^{4}\mathrm{He}) - D(^{6}\mathrm{He}) \tag{4.3a}$$

$$Q_2 = D(^{78}\mathrm{Kr}) - D(^{76}\mathrm{Kr}) + D(^{4}\mathrm{He}) - D(^{6}\mathrm{He})\,. \tag{4.3b}$$

The measured quantity is $\Delta Q = Q_1 - Q_2$, the difference between these reaction energies:

$$\Delta Q = D(^{80}\mathrm{Kr}) + D(^{76}\mathrm{Kr}) - 2D(^{78}\mathrm{Kr})\,. \tag{4.4}$$

Unfortunately, this value is not given in the paper, but using the reported value of $Q_2 = -20351(10)$ keV and the mass excesses of $^{80}$Kr, $^{78}$Kr, $^{6}$He, and $^{4}$He available in 1978 [Waps1977], one can calculate back and obtain $\Delta Q = 1432$ keV.

The AME datum for this reaction was therefore changed to reflect the relation of Eq. (4.4) and assigned a value of 1432(10) keV. This replacement, however, does not cure the disagreement with the ISOLTRAP datum. It is even slightly worsened to $1.8\sigma$ and remains as such. Interestingly, the replacement increases the influence of the measurement of [Molt1982] on the mass of $^{76}$Kr from 10 to 15 %. An influence on $^{78}$Kr of 5 % and a marginal influence on $^{80}$Kr are also introduced. Only the more precise of the two previously used measurements, the value from [Molt1982], is retained as an input parameter for the mass evaluation alongside the new ISOLTRAP value.

### $^{76}$Rb

$^{76}$Rb is the only nuclide of those presented here whose mass had previously been measured by ISOLTRAP. The former Penning trap measurement with a relative uncertainty of $1.0 \cdot 10^{-7}$ [Otto1994] completely determined the mass excess. The $^{74,75,77}$Rb triplet datum of Audi *et al.* mentioned above is in very good agreement with that value. Our present measurement reproduces the previous ISOLTRAP datum very well and reduces its uncertainty by a factor of four. Due to the much smaller uncertainty of the new result, the old values are outweighed.

### $^{77}$Kr

Before the new ISOLTRAP datum, the mass of $^{77}$Kr was determined by two different measurements made by the same group [Molt1987]. The more precise of the two was obtained from the $Q$ value of the $^{78}$Kr($d$,$t$)$^{77}$Kr reaction. The second value was obtained by an analogous measurement to the ($^{3}$He,$^{6}$He) reaction described above for $^{75}$Kr. The two data are in good agreement with each other. An older value from a beta end point measurement [Thul1955] deviates from their average by $1.9\sigma$. A comparison of the mass excesses obtained from these three measurements with the AME 1995 value and our datum is shown in Fig. 4.5.

Our measurements of $^{77}$Kr and $^{78}$Kr destroy the good agreement between the two measurements from [Molt1987]. The ($^{3}$He,$^{6}$He) datum agrees well with our value, but the ($d$,$t$) $Q$ value now deviates from the ISOLTRAP value by $2.5\sigma$. Moltz *et al.* bombarded a $^{78}$Kr gas target with a 29.1-MeV deuteron beam and observed the triton position spectrum in a split-pole spectrograph. The focal plane was calibrated with tritons from the $^{22}$Kr($d$,$t$)$^{21}$Ne$^{*}$ (351 keV) and the $^{40}$Ar($d$,$t$)$^{39}$Ar$^{*}$ (1267, 1517, and 2358 keV) reactions. The triton position spectrum from [Molt1987] is shown in Fig. 4.6. The double peak towards the higher-energy (right) side of the spectrum was identified as corresponding to the ground and first excited state (66 keV) of $^{77}$Kr. The predominant 66-keV peak has a

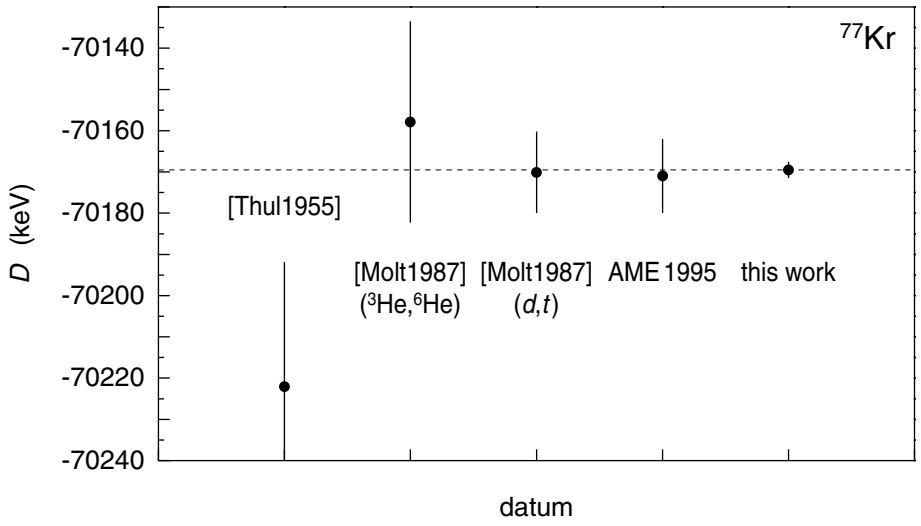


Figure 4.5: Comparison of previous measurements with the ISOLTRAP result for $^{77}$Kr. The mass excesses are calculated from the measured reaction or decay energies using the AME 1995 data for the masses of the other nuclides involved. The dashed horizontal line corresponds to the ISOLTRAP datum.

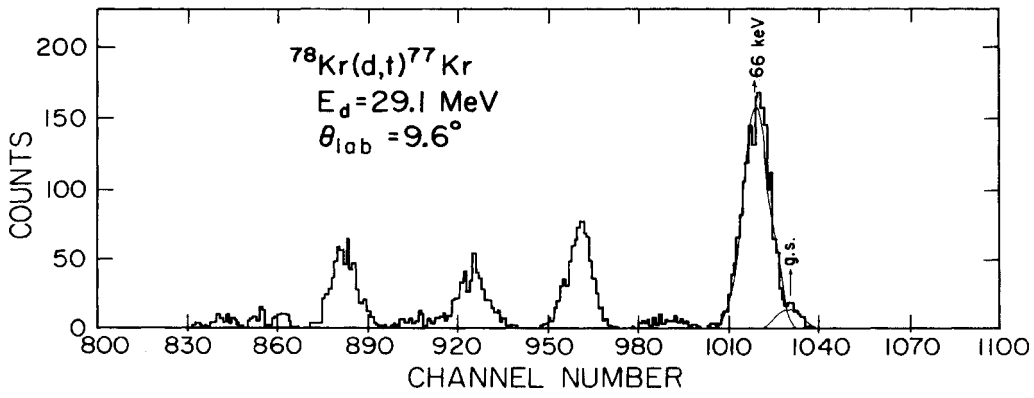


Figure 4.6: Figure 4 from [Molt1987]. The figure shows the triton position spectrum from the $^{78}$Kr($d$,$t$)$^{77}$Kr reaction. See the discussion in the text.

full width at half maximum of about 65 keV, which means that the reported uncertainty of 7 keV is reasonable. No obvious flaw could therefore be found in the reference and the disagreement remains. Because the uncertainty of the value from the (*d*,*t*) is only about half that of the new ISOLTRAP datum, it retains some weight while the value from the ($^3$He,$^6$He) reaction is outweighed.

The deviation of the value of [Thul1955] is reduced from 1.9$\sigma$ to 1.7$\sigma$ with our new $^{77}$Kr mass. In his paper, Thulin only gave a beta end point energy of 1860 keV, without uncertainty, suggesting that the decay populates the ground state of $^{77}$Br. When the datum was entered into the AME, it was re-interpreted as populating the 129.6-keV level and was assigned an uncertainty of 30 keV. Considering the complexity of the Fermi analysis that led to the end point energy, the uncertainty of the energy was possibly underestimated.

### $^{78}$Kr

The masses of the stable isotopes of an element are often well-known because the isotopes are easily obtained and can be made available to a large number of experiments. It is even the more surprising when an ISOLTRAP measurement of such a stable nuclide deviates by a large amount from the accepted value. This is the case with $^{78}$Kr, where the mass reported here shows a 2.7$\sigma$ disagreement with the previous adjusted value. An overview of the previous values for the mass excess and the ISOLTRAP value from this work is shown in Fig. 4.7.

Before our new datum, the adjusted mass excess of $^{78}$Kr was determined by three measurements [Ries1963, Molt1987, Step1987]. The first datum is from a measurement of the mass difference between $C_6H_6$ and $^{78}$Kr with a double-focusing mass spectrometer, the second from a measurement of the reaction energy of $^{78}$Kr(*d*,*t*)$^{77}$Kr, and the third from a *Q* value determination of the $^{78}$Kr($^3$He,*d*)$^{79}$Rb reaction. A somewhat less precise measurement via the *Q* value of the $^{78}$Kr($^3$He,$^6$He)$^{75}$Kr reaction, also from [Molt1987], supports the (*d*,*t*) result from the same paper.

The mass spectrometry datum from Ries *et al.*, shown as an empty circle in Fig. 4.7, seemed to deviate quite strongly from the other data. This was in reality not the case. Instead, their value had been incorrectly transcribed into the AME from the original publication. That error also in part explains the discrepancy between the AME 1995 value and our result. After correction, the result from [Ries1963] is in good agreement with the other three values and in excellent agreement with our datum. The ISOLTRAP mass also agrees well with the mass from the paper of Stephans *et al.* but is in disagreement with both measurements of [Molt1987].

### $^{80}$Kr

Our new datum for the mass of $^{80}$Kr agrees well with the previously accepted value. The six measurements that contribute to the adjusted value of AME 1995 agree very well with each other; their maximum deviation from it is 0.6$\sigma$. In particular the three most precise previous determinations [Ries1963, Kato1969, Burk1986] agree well with the ISOLTRAP result and will therefore not be discussed in detail. The *Q* value of the $^{80}$Kr($^3$He,$^6$He)$^{77}$Kr reaction from [Molt1987], being the least precise of all measurements, is removed from

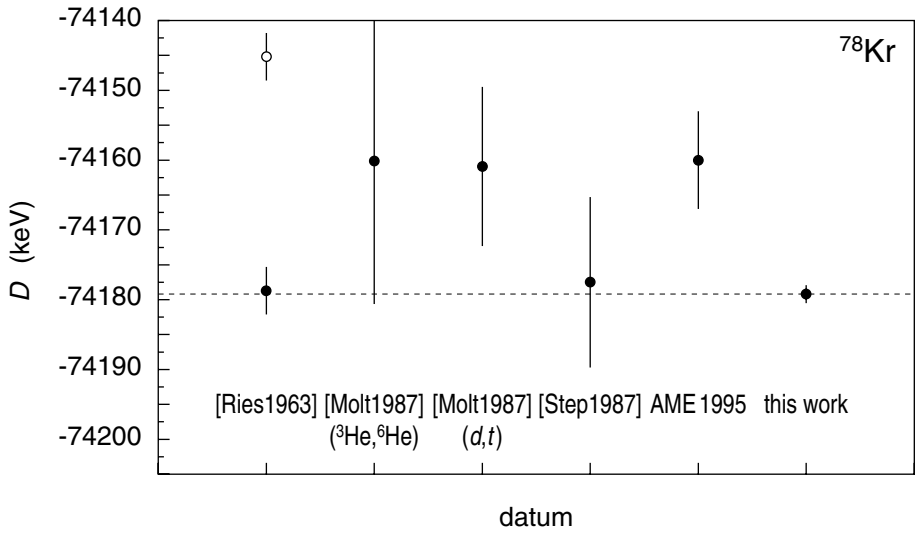


Figure 4.7: Comparison of previous measurements with the ISOLTRAP result for $^{78}$Kr. The mass excesses are calculated from the measured mass difference or reaction energies using the AME 1995 data for the masses of the other nuclides involved. The dashed horizontal line corresponds to the ISOLTRAP datum. The empty circle for the measurement of [Ries1963] represents a datum that was incorrectly transcribed into the AME 1995. The filled circle is the correct value.

the adjustment calculation of the AME; all other remain included. An additional datum due to the modified ($^4$He,$^6$He) value from [Molt1987] is newly introduced. Its disagreement with our result is of course the same (in opposite direction) as that for the mass of $^{76}$Kr and has already been discussed there.

### $^{82}$Kr

The AME 1995 mass of $^{82}$Kr receives contributions from six different measurements using a wide range of techniques and mass relations. They all agree with each other within $\leq 0.9\sigma$. The new ISOLTRAP mass value, whose uncertainty is slightly smaller than that of the previous accepted value, deviates mildly from it by $0.7\sigma$. A direct comparison with the three most precise previous measurements is even more favorable: The result from a beta end point determination of the $^{82}$Br($\beta^-$)$^{82}$Kr decay [Wadd1956], a mass-spectrometry measurement [Ries1963], and the fairly recent datum from a high-resolution deflection mass spectrometer [Nxum1993] are in excellent agreement with our value. For the adjustment, all old input parameters are kept and the ISOLTRAP datum is added.

### $^{88}$Sr

The ISOLTRAP value for the mass excess of the stable $^{88}$Sr stems from a single TOF cyclotron resonance recorded during the Rb data taking period in 2000. This accounts for

the rather large uncertainty of our datum. The measurement deviates by exactly one standard deviation from the accepted value which is essentially derived from the $Q$ value of the $^{87}$Sr($n$,$\gamma$)$^{88}$Sr reaction measured at the ILL in Grenoble [Wint1987]. Since a deviation larger or equal to $1\sigma$ is expected in about one out of three measurements, this is no reason to question the validity of the other data taken during either of the data taking periods. Since the uncertainty of the ISOLTRAP mass excess is ten times larger than that of the previous value, it is outweighed.

**$^{133}$Cs**

The MIT Penning trap mass measurements of the stable nuclides $^{85}$Rb and $^{133}$Cs reached relative uncertainties of $1.6{\cdot}10^{-10}$ and $2.0{\cdot}10^{-10}$, respectively [Brad1999]. A determination of the cyclotron frequency ratio of these two nuclides by ISOLTRAP can therefore not contribute to the final result of the AME. However, such a measurement is an excellent supplementary test of the accuracy of the apparatus. The resonance recorded during the Kr data taking period is in perfect agreement with the MIT value while the datum from the Rb run deviates from it by $1\sigma$. As was said in the case of $^{88}$Sr, such a deviation is expected in one out of three cases and is certainly acceptable. For the reasons mentioned above, the ISOLTRAP values are outweighed and are included in the AME merely for consistency checks.

### 4.2.2 Result of the evaluation

The result of the least-squares adjustment is given in Tab. 4.2. In the first column, the mass excesses obtained in this work are presented. The second column gives the previous literature value [Audi1995] and the third column the difference between the two. The fourth column shows the new mass excess after the mass evaluation including the ISOLTRAP results. The influence of the ISOLTRAP data on the final mass excesses is given in the last column. The second column is the result of a calculation according to Eqs. (2.3) and (4.1) using the current best values for the mass of the reference ion, the unified atomic mass unit, and the mass of the electron, all given in Sec. 4.1. For the nuclide $^{74}$Ga, the correction due to a possible presence of an isomer has been applied.

In the cases of $^{75}$As and $^{88}$Sr, the difference in mass excess between the third and the fifth column is due to other measurements that have been added to the AME since its last publication in 1995. They reflect the status of March 2002.

**$^{73-75}$Kr, $^{74}$Ga, $^{74,76}$Rb**

The ISOLTRAP frequency ratios obtained in the Kr and Rb data taking periods in 2000 completely determine the mass excess values for these nuclides. The deviations from previous measurements discussed in 4.2.1 remain unchanged.

Table 4.2: Result of the atomic-mass evaluation. The experimental mass excess $D_{\mathrm{exp}}$ from the ISOLTRAP cyclotron frequency ratio measurements was calculated using the most recent values for the mass of $^{85}$Rb, the electron mass, and the unified atomic mass unit, all given in the text. Uncertainties (in parentheses) refer to the least significant digits of a quantity. The literature values $D_{\mathrm{lit}}$ are from [Audi1995], except the one for $^{133}$Cs, which is from the recent MIT Penning trap measurement [Brad1999, Audi2002]. The adjusted mass excess $D_{\mathrm{new}}$ is the result of the atomic-mass evaluation and reflects the status of March 2002. In the cases of $^{75}$As and $^{88}$Sr, the difference in mass excess between the third and the fifth column is due to other measurements that have been added to the AME since its last publication in 1995. The last column shows the influence of the ISOLTRAP measurements on the final value. The slight change in the uncertainty between the ISOLTRAP result and the AME value for $^{75}$Kr and $^{76}$Rb is due to rounding errors that may occur in the additional calculation steps of the AME.

| Nuclide | $D_{\mathrm{exp}}$ (keV) | $D_{\mathrm{lit}}$ (keV) | $D_{\mathrm{exp}} - D_{\mathrm{lit}}$ (keV) | $D_{\mathrm{new}}$ (keV) | Infl. (%) |
|---|---|---|---|---|---|
| $^{73}$Kr | −56 550.8(9.0) | −56 890(140) | 339 | −56 550.8(9.0) | 100 |
| $^{74}$Kr | −62 330.3(2.4) | −62 170(60) | −160 | −62 330.3(2.4) | 100 |
| $^{75}$As | −73 031.7(7.0) | −73 032.5(1.6) | 0.8 | −73 032.9(1.6) | 0 |
| $^{75}$Kr | −64 323.6(8.0) | −64 241(15) | −83 | −64 323.6(8.1) | 100 |
| $^{76}$Kr | −69 010.4(4.4) | −68 979(11) | −31 | −69 013.8(4.0) | 85 |
| $^{77}$Kr | −70 169.5(2.0) | −70 171.0(9.0) | 1.5 | −70 170.8(1.9) | 93 |
| $^{78}$Kr | −74 179.2(1.3) | −74 160.0(7.0) | −19.2 | −74 178.1(1.2) | 91 |
| $^{80}$Kr | −77 891.9(1.6) | −77 893.0(4.0) | 1.1 | −77 892.3(1.3) | 86 |
| $^{82}$Kr | −80 590.8(2.5) | −80 588.6(2.6) | −2.2 | −80 589.6(1.7) | 48 |
| $^{133}$Cs | −88 071.0(6.3) | −88 070.960(22) | 0.0 | −88 070.960(22) | 0 |
| $^{74}$Ga | −68 049(21) | −68 044(71) | −5 | −68 049(21) | 100 |
| $^{74}$Rb | −51 905(18) | −51 730(720) | −175 | −51 905(18) | 100 |
| $^{76}$Rb | −60 479.8(1.8) | −60 481.0(8.0) | 1.2 | −60 479.8(1.9) | 100 |
| $^{88}$Sr | −87 938(18) | −87 919.7(2.2) | −18 | −87 920.8(1.1) | 0 |
| $^{133}$Cs | −88 072.5(1.5) | −88 070.960(22) | −1.6 | −88 070.960(22) | 0 |

### $^{76-78,80,82}$Kr

After the adjustment calculation, the mass of $^{76}$Kr is influenced at 85 % by our new value and at 15 % by the value of [Molt1982]. Our result deviates by $0.8\sigma$ and the datum of Moltz *et al.* by $1.8\sigma$ from the adjusted value. The measurement of [Mats1981] is now off by $1.0\sigma$ from the best value.

The $^{77}$Kr mass is now almost completely determined by ISOLTRAP with an influence of 93 %. Due to the strong disagreement with the mass from [Molt1987] ($2.5\sigma$ from the adjusted mass), our value is off by $0.7\sigma$ from the new best value. The other measurements, now outweighed, are in acceptable agreement with the new mass.

The ISOLTRAP measurement of $^{78}$Kr contributes 91 % to the current value. The two measurements of [Molt1987] deviate by 4.5$\sigma$ and 2.5$\sigma$ from the new mass, but in opposite directions. The disagreement of the measurement of [Step1987] with the previous adjusted value is now cured, and the corrected datum from [Ries1963] also agrees well with the new value.

For the nuclide $^{80}$Kr, four out of five contributing measurements are in good agreement with the adjusted value, to which our datum contributes 86 %. The conflict of the modified entry for the $^{78}$Kr($^{4}$He,$^{6}$He)$^{76}$Kr reaction of Moltz *et al.* that creates a 1.8$\sigma$ conflict for $^{76}$Kr appears here as well, but with opposite sign.

The influences of various experiments on the mass of $^{82}$Kr is more broadly distributed: ISOLTRAP contributes 48 %, the mass spectrometry datum from [Nxum1993] 27 %, the measurement from [Wadd1956] 16 %, and a second mass spectrometry value from [Ries1963] 5 %. All mentioned data are in excellent agreement with each other and with the adjusted value.

### $^{75}$As, $^{88}$Sr, $^{133}$Cs

The present AME mass excesses for these nuclides remain unaffected by the new ISOLTRAP values. As was discussed in 4.2.1, they are in excellent to acceptable agreement, confirming the validity of the other results.

### Influences on other nuclides

Due to the fact that the studied nuclides occupy a very small region of the nuclear chart only and that none of them are used as mass references (except among themselves), the measurements presented here have had no appreciable effect on the adjusted mass excesses of other nuclides.

# 5 Standard-Model tests with superallowed beta decays

## 5.1 Superallowed beta decay and the Standard Model

### 5.1.1 The $Ft$ value of superallowed beta decay

According to the conserved-vector-current (CVC) hypothesis, an important postulate of the Standard Model, the vector current part of the weak interaction is not influenced by the strong interaction. The intensity of a superallowed $\beta$ transition between $J^\pi = 0^+$ analog states therefore depends only on two quantities: The Fermi matrix element $\langle M_\mathrm{V} \rangle$ that connects the two states and the vector coupling constant $G_\mathrm{V}$ [Orma1989]:

$$ft = \frac{K}{G_\mathrm{V}^2 \langle M_\mathrm{V} \rangle^2}\,, \tag{5.1}$$

where $f$ is the statistical rate function, $t$ is the partial half-life, and $K$ is a product of fundamental constants given by

$$\frac{K}{(\hbar c)^6} = \frac{2\pi^3 \hbar \ln 2}{(m_e c^2)^5}\,. \tag{5.2}$$

If the final and initial state were identical, the model-independent matrix element could be calculated exactly and the coupling constant determined directly from experimental data. Two effects, however, disturb the simple picture of Eq. (5.1):

1. Radiative corrections due to bremsstrahlung and related effects must be applied to the statistical rate function:
$$f_\mathrm{R} = f(1 + \delta_\mathrm{R})\,. \tag{5.3}$$

2. The nuclear matrix element must be corrected due to the presence of isospin-nonconserving forces (Coulomb and nuclear). This correction, which expresses the fact that final and initial state are not completely identical, must be applied to the matrix element:
$$\langle M_\mathrm{V} \rangle^2 = \langle M_{\mathrm{V},0} \rangle^2 (1 - \delta_\mathrm{C})\,, \tag{5.4}$$
where $\delta_\mathrm{C}$ is called the isospin symmetry breaking correction and
$$\langle M_{\mathrm{V},0} \rangle^2 = T(T+1) - T_{z,\mathrm{i}} T_{z,\mathrm{f}} \cdot \delta_\mathrm{if} = 2\,, \tag{5.5}$$
where $T$ is the total nuclear isospin and the indices i and f refer to the initial and final states, respectively.

The so-called corrected $ft$ value, denoted by the symbol $Ft$, which includes these two nucleus-dependent corrections, is then given by:

$$Ft = ft \cdot (1 + \delta_R) \cdot (1 - \delta_C) . \tag{5.6}$$

The partial half-life $t$ is in turn given by the relation

$$t = \frac{T_{1/2} \cdot (1 + P_{EC})}{R} , \tag{5.7}$$

where $T_{1/2}$ is the total nuclear half-life, $R$ is the measured branching ratio for the superallowed channel, and $P_{EC}$ is the calculated electron-capture fraction of the decay [Hard1990]. Except for $^{10}$C, $P_{EC}$ is typically slightly below 0.1 %.

The overall expression for the $Ft$ value then becomes:

$$Ft = \frac{f \cdot T_{1/2}}{R} \cdot (1 + P_{EC}) \cdot (1 + \delta_R) \cdot (1 - \delta_C) . \tag{5.8}$$

The three quantities $f$, $T_{1/2}$, and $R$ are accessible via experiments, while the electron capture fraction $P_{EC}$ and the two corrections $\delta_R$ and $\delta_C$, which are both of the order of 1 %, must be calculated. For each investigated decay, a total of three separate measurements must therefore be conducted and three independent calculations carried out.

While the calculations of the radiative correction are well founded [Hard1990], the theoretical investigations of $\delta_C$ for $^{74}$Rb based on different models yield greatly varying results. The values of the parameter $\delta_C$ for the different superallowed beta decays are shown in Fig. 5.1. It is striking how much larger the uncertainty for the 74Rb($\beta^+$)74Kr decay is compared to the other nuclides. This is due to the fact that the nine lighter nuclides share the same nuclear shell model space, while those with $A \geq 62$ are in a completely different nuclear region for which reliable nuclear-model calculations don't currently exist. The error bar for $^{74}$Rb in Fig. 5.1 spans the values obtained by two groups that employ different models [Orma1995, Saga1996]. Calculations by Ormand *et al.* are based on the shell model and full-parentage expansions in terms of Woods-Saxon radial wave functions or a self-consistent Hartree-Fock model. Those by Sagawa *et al.* use a Hartree-Fock or a random-phase approximation model in conjunction with Skyrme-type parametrizations of charge symmetry breaking and charge independence breaking forces. It becomes apparent from Fig. 5.1 that the large uncertainty of $\delta_C$ will also contribute to the uncertainty of $Ft$ and may prevent a decisive test of the CVC hypothesis at this time.

### 5.1.2 Check of the corrections to the $ft$ value

Under the assumption that the CVC hypothesis is in fact true, one may use the current world average $\overline{Ft}$ for all measured nuclides and try to determine the isospin mixing correction from the experimentally determined $ft$ value and the other calculated corrections. If the experimental precision on $ft$ is high enough, it may allow to discriminate between the presently two conflicting calculations and encourage further work in the hope of obtaining a solid value for future measurements.

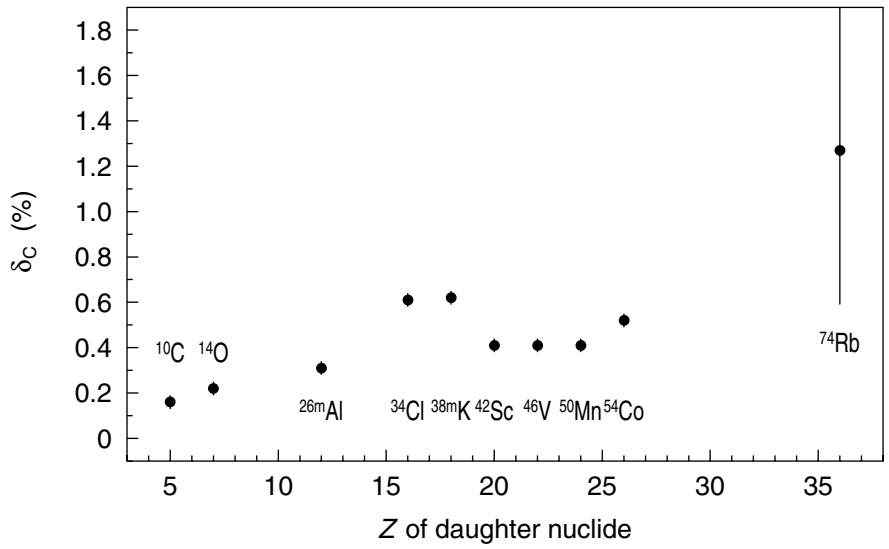


Figure 5.1: The calculated isospin symmetry breaking parameter for the superallowed beta decays of nine lighter nuclides [Town1999] and for $^{74}$Rb. The error bar for $^{74}$Rb spans the values obtained by two groups that employ different models [Orma1995, Saga1996]. See the discussion in 5.3.1.

### 5.1.3 Unitarity of the CKM matrix

Another important postulate of the Standard Model is the unitarity of the Cabibbo-Kobayashi-Maskawa (CKM) matrix, which relates the quark eigenstates of the weak interaction (primed) with their mass eigenstates (unprimed):

$$\begin{bmatrix} d' \\ s' \\ b' \end{bmatrix} = \begin{bmatrix} V_{ud} & V_{us} & V_{ub} \\ V_{cd} & V_{cs} & V_{cb} \\ V_{td} & V_{ts} & V_{tb} \end{bmatrix} \cdot \begin{bmatrix} d \\ s \\ b \end{bmatrix} . \tag{5.9}$$

The unitarity can, for instance, be evaluated by verifying that the sum of the squares of the elements of the first row is equal to one.

The most precise value for the up-down quark mixing element $V_{ud}$ can be extracted from the mean $Ft$ value of nuclear beta decay in conjunction with the axial-vector coupling constant $G_{\mathrm{A}}$ from muon decay. The matrix element in terms of the axial-vector coupling constant $G_{\mathrm{A}}$ and the mean $Ft$ value is [Hard2001]:

$$V_{ud}^2 = \frac{G_{\mathrm{V}}^2}{G_{\mathrm{A}}^2} = \frac{K}{2G_{\mathrm{A}}^2(1+\Delta_{\mathrm{R}})}\overline{Ft}\,, \tag{5.10}$$

where $\Delta_{\mathrm{R}}$ is a nucleus-independent radiative correction. The other two matrix elements of the first row, $V_{us}$ and $V_{ub}$, are obtained in high-energy-physics experiments from $K_{e3}$ decays and from semileptonic $B$ meson decays, respectively.

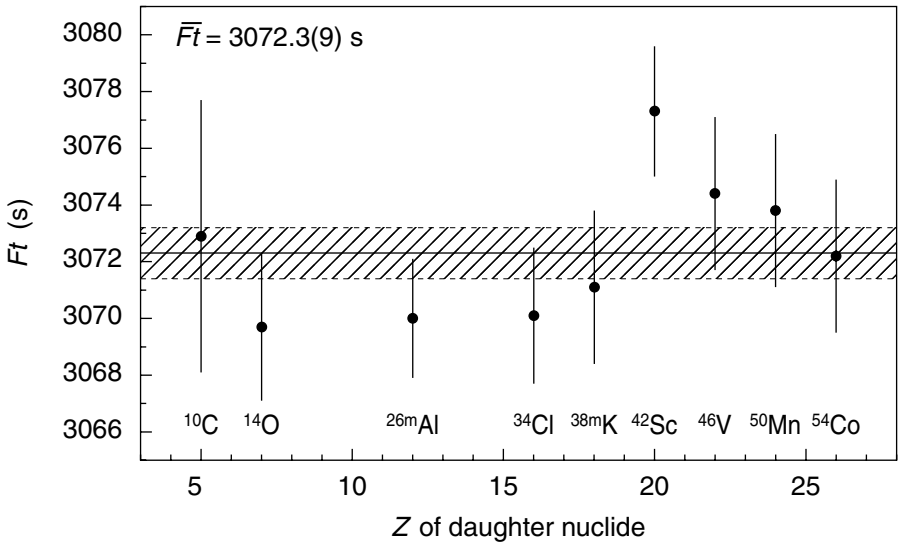


Figure 5.2: Present world status of $Ft$ values from nuclear beta decay, taken from [Town1999]. The hatched confidence interval of the mean represents only the statistical uncertainty.

## 5.2 Present status

All available high-precision data sets for $Ft$ values from nuclear beta decay have been collected for the first time in 1989 by Hardy and Towner [Hard1990] and have since been regularly updated. The most recent survey was conducted in 1998 [Town1999]. The $Ft$ values calculated from these more than 100 sets of data are shown in Fig. 5.2. The solid horizontal line is the weighted mean of all measurements, $\overline{Ft}$ = 3072.3 s. The hatched area encloses the $1\sigma$ confidence interval of the mean, representing only the statistical uncertainty of 0.9 s. Hardy and Towner add to this an uncertainty of 1.1 s due to the systematic difference in two different calculations of $\delta_C$ that were used. For the calculations performed later in this chapter, the two uncertainties are quadratically added to yield a combined uncertainty of 1.4 s.

The $\overline{Ft}$ thus obtained leads to an up-down quark mixing matrix element of $|V_{ud}|$ = 0.9740(5). Together with the high-energy physics results [Groo2000], the unitarity sum becomes [Hard2001]

$$|V_{ud}|^2 + |V_{us}|^2 + |V_{ub}|^2 = 0.9968(14)\,, \tag{5.11}$$

which differs from unity by more than $2\sigma$.

It may be worth noting that a value for $|V_{ud}|$ and for the unitarity sum can also be extracted from experimental data on free-neutron decay [Abel2000]. This decay has the advantage that there are no nuclear-structure-dependent corrections that need to be taken into account. But on the other hand, this decay has both a vector and an axial-vector part, requiring an additional correlation experiment to separate the two contributions. The matrix element from neutron decay is found to be $|V_{ud}|_n$ = 0.976(2) and the unitarity sum

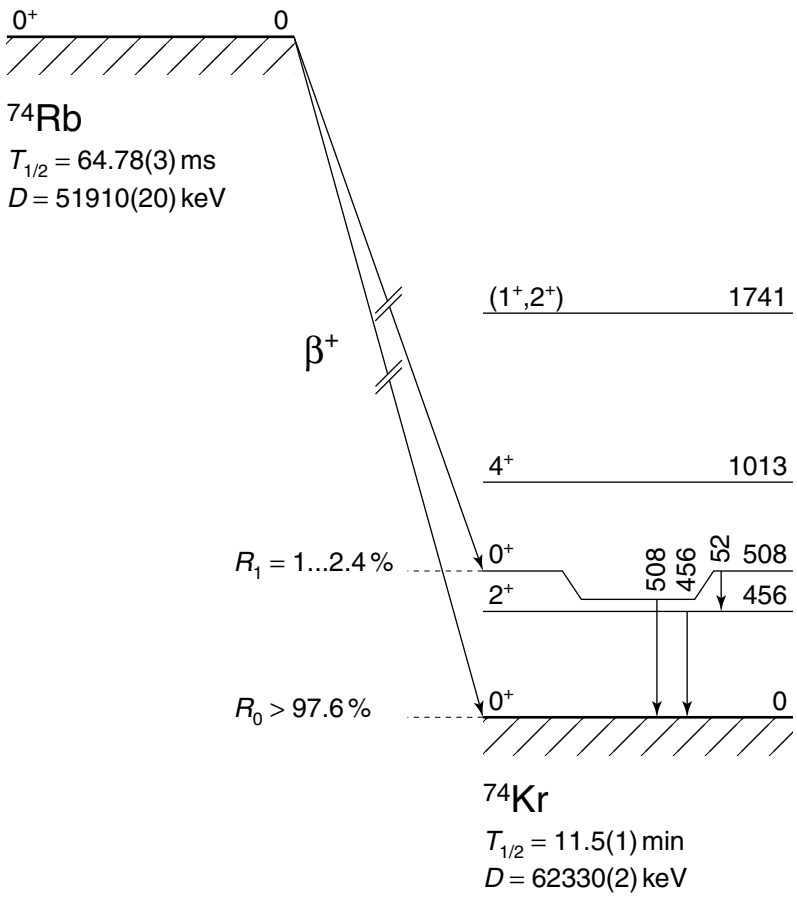


Figure 5.3: Decay scheme for $^{74}$Rb. Level energies are given in keV. The levels in $^{74}$Kr are from measurements in [Rudo1997, Chan1997, Beck1999]. The expected branching ratio to the first excited $0^+$ state is obtained from theoretical calculations from [Orma1995]. A detailed explanation is given in the text.

then becomes $|V_{ud}|^2_{\mathrm{n}} + |V_{us}|^2 + |V_{ub}|^2 = 1.001(4)$ [Hard2001].

The result from neutron decay agrees both with unity and with the unitarity sum from nuclear beta decay, but its uncertainty is three times higher. This shows how important new experimental data along both these fronts of research will be.

## 5.3 Experimental results

The decay scheme shown in Fig. 5.3 represents the present knowledge of the low-lying levels of $^{74}$Kr. The mass excesses $D$ given in the figure are those measured by us, the half-life of $^{74}$Rb is the weighted average of two recent measurements, details of which are given in 5.3.1.

The level structure of the daughter nucleus $^{74}$Rb has been specifically studied for its

high-spin rotational states [Rudo1997] and its low-lying $0^+$ states predicted by theoretical calculations [Chan1997, Beck1999]. The presence of an isomeric $0^+$ state was first observed at GANIL [Chan1997] and later confirmed in an experiment at the Vivitron accelerator [Beck1999]. In that experiment, its excitation energy was also measured to be 508 keV.

In addition to the superallowed decay to the ground state of $^{74}$Kr, a population of the low-lying $0^+$ state at 508 keV could be possible [Saga1996, Anto1997]. That state decays either via a 52-keV $0_2^+ \longrightarrow 2_1^+$ E2 transition, which subsequently decays by 456-keV E2 $\gamma$ emission, or directly by a 508-keV $0_2^+ \longrightarrow 0_1^+$ E0 transition. In addition to the fully converted ground-state transition, the low-energy E2 transition also largely decays by conversion electron emission with the energy of 38 keV.

The expected branching ratio of the allowed Fermi decay indicated in the figure was deduced from theoretical calculations of the isospin mixing correction parameter $\delta_{\mathrm{IM}}$ from [Orma1995]. The branching ratio $R_1$ to the first excited $0^+$ state can be calculated from $\delta_{\mathrm{IM}}$ using the relation [Hagb1994]

$$R_1 \approx \frac{f_1}{f_0} \cdot \delta_{\mathrm{IM}} \,, \tag{5.12}$$

where $f_0$ and $f_1$ are the statistical rate functions of the decays to the ground and excited states, respectively. According to a prescription also given in [Orma1995], the $\delta_{\mathrm{IM}}$ parameter can be scaled by a factor $(\Delta E_{01}^{\mathrm{th}}/\Delta E_{01}^{\mathrm{exp}})^2$ to improve the prediction, where $\Delta E_{01}^{\mathrm{th}}$ and $\Delta E_{01}^{\mathrm{exp}}$ are the calculated and the measured level energy of the first excited $0^+$ state, respectively. Using the statistical rate function calculated according to [Town1973] (see details in 5.3.2), the calculated isospin mixing parameter of Ormand *et al.*, and applying the correction for the measured level energy of 508 keV, a theoretical branching ratio of $R \approx 1 \ldots 2.4$ % is obtained.

## 5.3.1 Input parameters

### Decay energy

The decay energy or $Q$ value of the $^{74}$Rb($\beta^+$)$^{74}$Kr decay was measured indirectly via a determination of the atomic masses of the mother and the daughter nuclide. These measurements were carried out by us with the ISOLTRAP mass spectrometer during two distinct on-line experiments in October 2000. They are described in detail in Chap. 4.

As is explained in more detail in App. B, the $Q$ value of $\beta^+$ decay is given either as the actual decay energy or as the $Q$ value that the same decay would have if it were to take place via electron capture. The quantity used in the calculations of the statistical rate function $f$ is the electron capture decay energy $Q_{\mathrm{EC}}$, which is identical to the difference in the mass excesses of mother and daughter nuclide.

The result of the ISOLTRAP measurement is

$$Q_{\mathrm{EC}} = 10\,425(18) \ \mathrm{keV} \tag{5.13}$$

with a relative uncertainty of $1.7 \cdot 10^{-3}$.

### Half-life

The half-life of $^{74}$Rb was measured at TRIUMF [Ball2001] and at ISOLDE [Oino2001]. The group working at the ISAC facility at TRIUMF obtained a half-life of $T_{1/2}$ = 64.761(31) ms [Ball2001]. The measurement at ISOLDE was based on a determination of the time dependence of observed events in a thin scintillator detector. Two separate values were extracted from two sets of data, one without any condition and one with an energy condition of $E_{\beta^+} > 5.2$ keV. The two methods yielded half-lives of 64.90(9) ms and 64.77(17) ms, respectively. Due to the smaller uncertainty of the datum without energy condition, the value $T_{1/2}$ = 64.90(9) was adopted [Oino2001].

The TRIUMF and ISOLDE results deviate by $1.5\sigma$ from each other. For the purpose of the calculations presented here, the weighted average of the two measurements is used:

$$T_{1/2} = 64.776(29) \text{ ms} \tag{5.14}$$

with a relative uncertainty of $4.5 \cdot 10^{-4}$.

### Branching ratio

During the measurement of the half-life of $^{74}$Rb at ISOLDE, an attempt was also made to determine the branching ratio into the allowed beta channel to the first excited $0^+$ state at 508 keV. In that measurement, a peak identified as corresponding to the K conversion of the 508-keV E0 transition was observed. Its relative intensity compared to the total number of beta decays was measured to be $3.7(1.1) \cdot 10^{-4}$. A possible 38-keV peak due to conversion electron emission was not observed at all and therefore an upper limit of $1.6 \cdot 10^{-4}$ was deduced for its intensity. Combining these two numbers, it was only possible to deduce an *upper* limit of 99.947 % for the population of the $0^+$ ground state.

A group working at the ISAC facility at TRIUMF also attempted to measure the branching ratios to non-analog channels [Zgan2002]. They found that the branching ratio to the $0^+$ 508-keV state is smaller than $3 \cdot 10^{-4}$, thus supporting the ISOLDE result. However, they also found that the depopulation of the $2^+$ state at 456 keV is twenty times higher than its feeding from the 508-keV state. Supported by the observation of still unassigned $\gamma$ rays at 1198 and 4244 keV, they infer that appreciable Gamow-Teller $\beta$ decay feeding to higher-lying $1^+$ states must also take place. Zganjar *et al.* conclude that more complete spectroscopy is required to complete our knowledge of the decay scheme and they refrain from giving a number for the branching ratio to the ground state.

Based on both these results, however, it seems reasonable to assume that the total branching to states other than the ground state is much smaller than $5 \cdot 10^{-3}$. We therefore proceed with the conservative estimate for the branching ratio into the superallowed channel of

$$R = 0.995(5) \tag{5.15}$$

with a relative uncertainty of $5.0 \cdot 10^{-3}$.

**Electron capture fraction**

The fraction of the beta decays that occur via electron capture is not experimentally observed, but they must be taken into account for the calculation of the branching ratio by multiplication with the factor $(1 + P_{\mathrm{EC}})$ in Eq. (5.8).

The parameter $P_{\mathrm{EC}}$ can be calculated from an equation given in [Bamb1977]. In that paper, the calculated values are compared to experimental values and an agreement within a few percent is found. The calculated electron capture fraction for the superallowed decay of $^{74}$Rb is $P_{\mathrm{EC}} = 0.19$ % [Town2002], and the value adopted for the calculations here, with a conservatively estimated relative uncertainty of 10 %, is therefore

$$P_{\mathrm{EC}} = 0.001\,9(2)\,. \tag{5.16}$$

**Radiative correction**

The parameter $\delta_{\mathrm{R}}$ can be evaluated to first order in $\alpha$ with standard quantum electrodynamics [Sirl1978]. An analytic expression for the second-order term (order $Z\alpha^2$) was calculated independently by two groups [Sirl1986, Jaus1987, Sirl1987], who agree on the result, including the estimated third order (order $Z^2\alpha^3$) correction. Hardy and Towner use the formulas of Sirlin, but additionally incorporate a Fermi charge density distribution for the nucleus [Hard1990]. For the decaying nucleus $^{74}$Rb, they obtain [Town2002]

$$\delta_{\mathrm{R}} = 0.0150(12)\,, \tag{5.17}$$

where the relative uncertainty of $7.9 \cdot 10^{-2}$ corresponds to the component of order $Z^2\alpha^3$.

**Isospin symmetry breaking correction**

Two groups have published calculated values for the isospin symmetry breaking correction $\delta_{\mathrm{C}}$ in the last few years [Orma1995, Saga1996]. Both of them propose an array of values, based upon different forces and models used for the calculations. In the work of Ormand *et al.*, the numbers range from 0.91 to 1.94 %, Sagawa *et al.* give lower values between 0.59 and 0.74 %.

Neither group expresses a preference for any of their values; furthermore, no uncertainties are given. Pending further theoretical work, one must therefore adopt the center point of all given $\delta_{\mathrm{C}}$ values and assign an error bar that covers the whole range:

$$\delta_{\mathrm{C}} = 0.013(7)\,. \tag{5.18}$$

This corresponds to a relative uncertainty of 54 %.

### 5.3.2 The $Ft$ value of the $^{74}$Rb($\beta^+$)$^{74}$Kr decay

The statistical rate function $f$ of the $^{74}$Rb($\beta^+$)$^{74}$Kr decay was calculated according to the definition [Town1973]

$$f = \int_1^{W_0} pWq^2F(Z,W)C(W)\,\mathrm{d}W\,, \tag{5.19}$$

Table 5.1: Contributions of the relative uncertainties of the input parameters to the relative uncertainty of $Ft$ for the $^{74}$Rb case.

| Parameter | Rel. uncertainty | Reference | Contribution to rel. uncertainty of $Ft$ |
|---|---|---|---|
| $Q$ | $1.7 \cdot 10^{-3}$ | this work | $9.0 \cdot 10^{-3}$ |
| $T_{1/2}$ | $4.5 \cdot 10^{-4}$ | [Oino2001, Ball2001] | $4.5 \cdot 10^{-4}$ |
| $R$ | $5.0 \cdot 10^{-3}$ | [Oino2001, Zgan2002] | $5.0 \cdot 10^{-3}$ |
| $P_{\mathrm{EC}}$ | $1.0 \cdot 10^{-1}$ | [Town2002] | $1.9 \cdot 10^{-4}$ |
| $\delta_{\mathrm{R}}$ | $8.0 \cdot 10^{-2}$ | [Town2002] | $1.2 \cdot 10^{-3}$ |
| $\delta_{\mathrm{C}}$ | $5.4 \cdot 10^{-1}$ | [Orma1995, Saga1996] | $6.9 \cdot 10^{-3}$ |
| total | | | $1.2 \cdot 10^{-2}$ |

where $W$ is the total electron energy, $W_0$ is the maximum total electron energy, $p = \sqrt{W^2 - 1}$ is the electron momentum, $q$ is the neutrino momentum (all in units of $m_e$), $F(Z, W)$ is the Fermi function, and $C(W)$ is the shape correction factor. The exact expression for $F(Z, W)C(W)$ is given in [Town1973] and will not be repeated here. The evaluation of the integral in Eq. (5.19) yields [Town2002]

$$f = 47\,600(430)\,. \tag{5.20}$$

Using the statistical rate function thus obtained and the other input values enumerated in 5.3.1, the following result for the $Ft$ value of the superallowed $^{74}$Rb($\beta^-$)$^{74}$Kr decay is obtained:

$$Ft = 3111(39)\ \mathrm{s}\,. \tag{5.21}$$

In Fig. 5.4, this result is shown in comparison with the previous status. Figure 5.4(a) shows that the value obtained by use of the $Q$ value determined by ISOLTRAP is in agreement with the confidence band of the mean $Ft$ from all other measurements; our $Ft$ value is larger by 39 s than $\overline{Ft}$. It is obvious, however, that the precision of the datum is not high enough to make a definitive statement about the nucleus-independence of $Ft$.

In Fig. 5.4(b), the $Ft$ values calculated using the $Q$ values from AME 1995 (empty circle) and the MISTRAL measurement (empty diamond) are shown alongside the ISOLTRAP value. Note the change of factor 25 in the vertical scale between (a) and (b). The figure illustrates the enormous improvement brought about by our determination of the masses of $^{74}$Rb and $^{74}$Kr.

It is interesting to examine which of the input parameters limit the precision of the $Ft$ result for $^{74}$Rb. The contributions of the relative uncertainties of the input parameters to the relative uncertainty of $Ft$ are shown in Tab. 5.1. Currently, the decay energy $Q$ contributes the largest part to the overall uncertainty (56 %), followed by the isospin mixing correction $\delta_{\mathrm{C}}$ with 33 % and the branching ratio $R$ with 17 %.

If one wanted to achieve an $Ft$ value for $^{74}$Rb with an uncertainty comparable to those of the other nuclides for which high-precision measurements exist ($\approx$ 3 s), and assuming

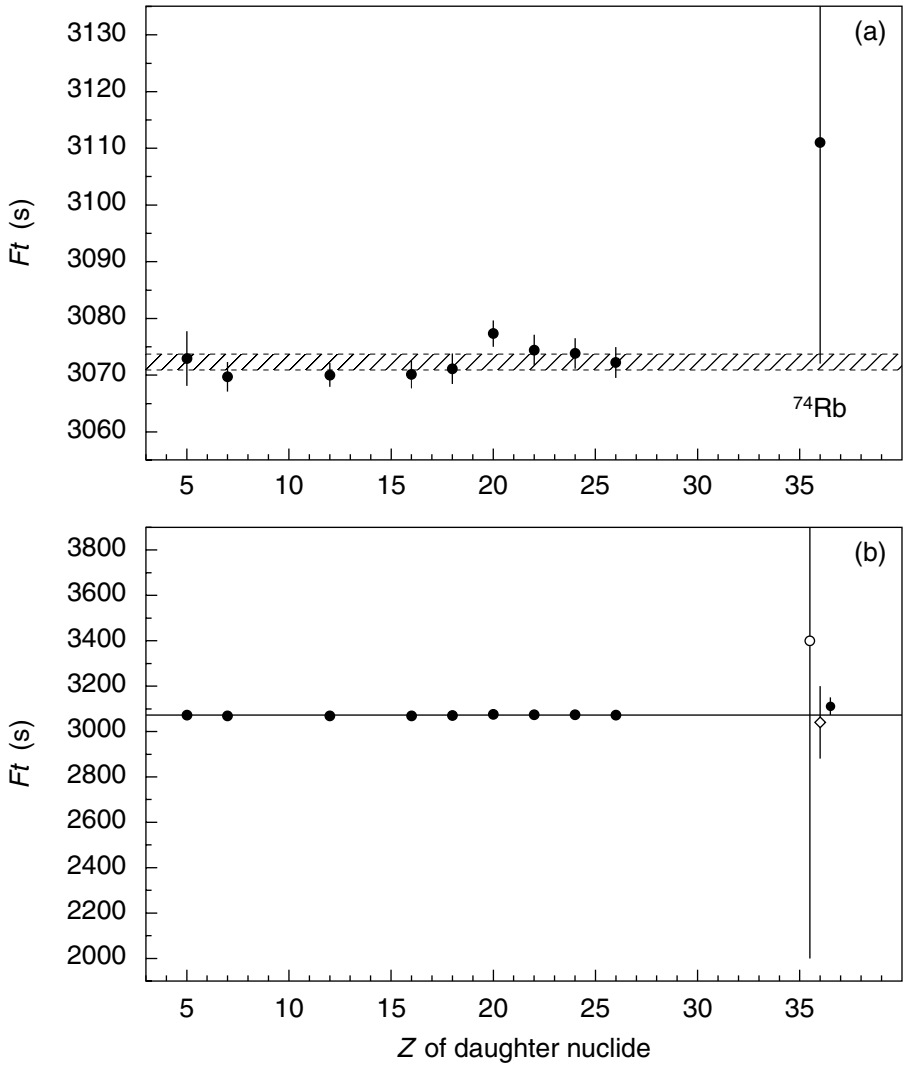


Figure 5.4: The same graph as shown in Fig. 5.2, but now including the $^{74}$Rb result. (a) $Ft$ value for the $^{74}$Rb($\beta^+$)$^{74}$Kr decay calculated by use of the $Q$ value measured by ISOLTRAP. The hatched area encloses the confidence interval of the weighted mean of the other data, now including the systematic uncertainty added in quadrature. (b) The same comparison, but including two data points for the previously known $Q$ values of the $^{74}$Rb($\beta^+$)$^{74}$Kr decay: AME 1995 (empty circle) and MISTRAL (empty diamond) in addition to the datum using the ISOLTRAP $Q$ value (filled circle). Note the change in scale by a factor of 25 between (a) and (b).

that all input parameters would be allowed to contribute equal uncertainties to the final result, the reaction energy $Q$ would have to be measured to about 0.9 keV (factor of 20 reduction of the uncertainty). But also the knowledge of $\delta_C$ would need to be improved by a factor of 17, that of $R$ by a factor of 13, and $\delta_R$ would need to be computed to a three times higher precision. In fact, given the current knowledge of the other input parameters, the uncertainty of $Ft$ would still be larger than 25 s even if $Q$ was known exactly. The precisions of the half-life $T_{1/2}$ and the electron capture fraction $P_{EC}$ are already sufficient for an uncertainty of the $Ft$ value of the order of 3 s.

### 5.3.3 A check of the correction $\delta_C$ with the ISOLTRAP $f$ value

In 5.3.2, it was shown that the insufficient knowledge of the magnitude of the isospin mixing correction $\delta_C$ also limits the precision of the current value for $Ft$. Further theoretical work will be necessary to complete our knowledge of the exact magnitude of that correction. As was pointed out in 5.1.2, however, under the explicit assumption that $Ft$ is in fact constant, the statistical rate function $f$ from the ISOLTRAP measurement calculated above may be used to determine which of the calculated values of $\delta_C$ for $^{74}$Rb describes the experimental results best.

Using the current experimental average of $\overline{Ft} = 3072.3(1.4)$ s and $f = 47\,600(430)$ from our measurement, the parameter $\delta_C$ can then be calculated from (5.8):

$$\delta_C = 0.025(10)\,. \tag{5.22}$$

In Fig. 5.5, this result is compared with the calculations of [Orma1995] and [Saga1996]. The experimental datum for $\delta_C$ is larger than all those obtained from the quoted theoretical calculations. It tends to exclude all values proposed by Sagawa *et al.* and slightly favors those of Ormand *et al.*, especially the ones obtained by use of Woods-Saxon single-particle wave functions.

The contributions of the relative uncertainties of the input parameters to the relative uncertainty of $\delta_C$ are shown in Tab. 5.2. Again, the uncertainty in the decay energy $Q$ is the dominant factor with a contribution of 73 %, but the insufficient knowledge of the branching ratio $R$ also contributes 23 % to the final uncertainty. All other input parameters are not presently of any concern since their relative uncertainties are at least one order of magnitude smaller than those of $Q$ and $R$. If the error bars on these two parameters were reduced by a factor of five each, $\delta_C$ could be given with a relative uncertainty of better than 10 %, thereby allowing to discriminate clearly between the different calculated values.

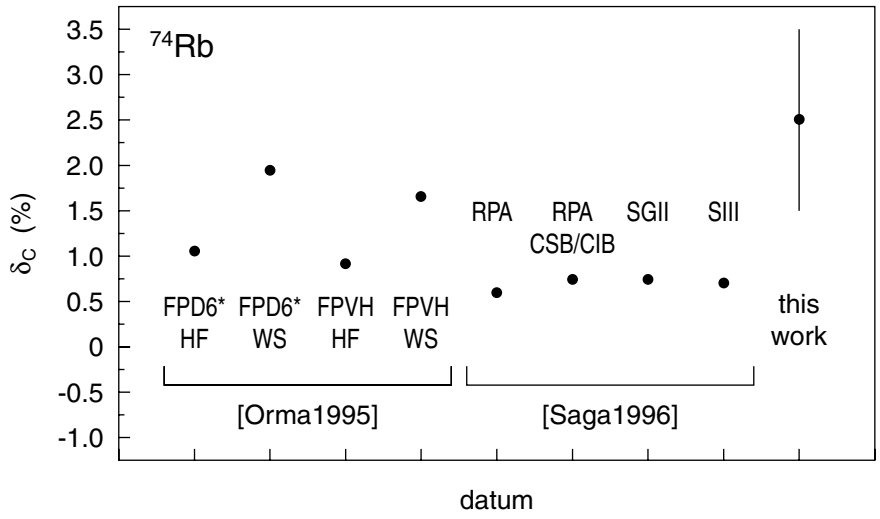


Figure 5.5: The isospin symmetry breaking parameter $\delta_C$ calculated by use of the $Q$ value measured by ISOLTRAP compared with the calculated values [Orma1995, Saga1996].

Table 5.2: Contributions of the relative uncertainties of the input parameters to the relative uncertainty of $\delta_C$ for the $^{74}$Rb case.

| Parameter | Rel. uncertainty | Reference | Contribution to rel. uncertainty of $Ft$ |
|---|---|---|---|
| $Q$ | $1.7 \cdot 10^{-3}$ | this work | $3.5 \cdot 10^{-1}$ |
| $T_{1/2}$ | $4.5 \cdot 10^{-4}$ | [Oino2001, Ball2001] | $1.8 \cdot 10^{-2}$ |
| $R$ | $5.0 \cdot 10^{-3}$ | [Oino2001, Zgan2002] | $2.0 \cdot 10^{-1}$ |
| $P_{EC}$ | $1.0 \cdot 10^{-1}$ | [Town2002] | $7.4 \cdot 10^{-3}$ |
| $\delta_R$ | $8.0 \cdot 10^{-2}$ | [Town2002] | $4.6 \cdot 10^{-2}$ |
| $\overline{Ft}$ | $4.6 \cdot 10^{-4}$ | [Town1999] | $1.8 \cdot 10^{-2}$ |
| total | | | $4.1 \cdot 10^{-1}$ |

# 6 Conclusion

**A study of the accuracy of ISOLTRAP**

A detailed study of the various contributions to the uncertainty of a measurement with the ISOLTRAP mass spectrometer was conducted. Several distinct effects were identified and their magnitudes measured where possible.

A technique was developed that allows an estimate of the uncertainty of a cyclotron frequency determination in the presence of contaminant ions in the precision trap. The contributions of random magnetic-field fluctuations to the uncertainty of a cyclotron frequency measurement were determined. These fluctuations were found to contribute a relative uncertainty which is directly proportional to the total time required for the three cyclotron frequency determinations that constitute one complete measurement.

A carbon cluster ion source was built and installed at the ISOLDE apparatus. Carbon clusters $^{12}C_n$ ($6 \leq n \leq 20$) were used to quantify systematic effects in the mass measurement procedure with ISOLTRAP. A mass-dependent systematic shift was identified and its magnitude found to be $-1.6(4)\cdot 10^{-10}/\mathrm{u}\cdot(m - m_{\mathrm{ref}})$. The residual systematic uncertainty after correction for the mass-dependent effect was determined to be $u_{\mathrm{res}}(r)/r = 8 \cdot 10^{-9}$, which also represents the present limit of mass accuracy of the ISOLTRAP system.

Based on the results of these measurements, modifications to the measurement procedure as well as a new evaluation procedure were defined. After these procedural changes, the limit of mass accuracy in ISOLTRAP measurements is more than an order of magnitude smaller than the systematic uncertainty previously added to the final results and about a factor of four smaller than the former best-case estimate [Beck1997b]. Overall mass uncertainties of close to $10^{-8}$ have been reached for the first time in the work reported here. In the mass region below that covered by the carbon cluster cross-reference data, our recent mass measurements of the stable argon isotopes $^{36}$Ar and $^{38}$Ar [Herf2002] are in excellent agreement with other experimental data [Berg2002, Audi1995], indicating that the conclusions from the carbon cluster results can be extended to lower masses.

Investigations of the efficiency of cluster production with the matrix-assisted laser desorption and ionization time-of-flight (MALDI-TOF) apparatus at Mainz indicate that the commercial material Sigradur® may be better suited for the production of carbon clusters $C_n$, $n \leq 20$ [Blau2002b]. Sigradur® is a material with ceramic properties that consists of pure carbon. It is obtained by thermal decomposition of a synthetic resin. Using this material, the present study could easily be extended to lighter clusters $C_n$, $n \leq 5$.

In the future, it will be possible to perform absolute mass measurements of radioactive nuclides using carbon clusters as reference ions. As an added benefit, the masses of these clusters are evenly spaced at intervals of 12 u throughout the entire chart of the nuclides such that the maximal mass difference $m - m_{\mathrm{ref}}$ will be 6 u. As a consequence, the relative mass-dependent shift will be smaller than $1 \cdot 10^{-9}$ in future high-precision mass measurements.

This study has also made apparent some weaknesses in the experimental setup and

measurement procedure. An improved vacuum in the precision trap may reduce the amount of contamination created by charge exchange reactions and would allow even longer observation times, such as are needed to resolve contaminations by isomers with excitation energies smaller than 100 keV. A stabilization of the gaseous-helium pressure of the magnet cryostat holds the prospect of greatly reducing the observed magnetic-field fluctuations. Finally, a modified measurement cycle in which reference ion and ion of interest are observed alternatingly in quick succession will effectively eliminate the effect of any remaining such fluctuations. Improvements of the setup that address these issues are currently being studied.

### Mass measurements of neutron-deficient Rb and Kr isotopes

Atomic mass measurements on Kr and Rb isotopes were carried out with the main goal of determining the mass difference between $^{74}$Rb and $^{74}$Kr to better than 10 keV. The final mass uncertainty of $^{74}$Rb did not quite match that goal, but with a half-life of under 65 ms, $^{74}$Rb is the shortest-lived nuclide ever studied in a Penning trap.

The new ISOLTRAP measurements of $^{73-75}$Kr, $^{74}$Ga, and $^{74,76}$Rb completely determine the mass excesses of these nuclides obtained from the atomic-mass evaluation. In the case of $^{76-78,80,82}$Kr, our values make contributions to the adjusted value between 48 and 93 %. The mass measurements of the well-known nuclides $^{75}$As, $^{88}$Sr, and $^{133}$Cs agree with the accepted values and confirm the results of the study of the accuracy of the apparatus.

### Standard-Model tests with superallowed beta decays

The mass measurements of $^{74}$Rb and $^{74}$Kr have for the first time allowed the determination of the $Ft$ value of the superallowed beta decay of $^{74}$Rb. A value of $Ft = 3111(39)$ s was found, higher than the world average $\overline{Ft}$ of the other high-precision data but still in a $1\sigma$ agreement with it. While this result doesn't clearly confirm the nuclide independence of $Ft$, the uncertainty of the result is too large to make a definitive statement. This is due in part to the insufficient precision of our measurement of the mass of $^{74}$Rb, but also the uncertainty of the branching ratio $R$ into the superallowed channel needs to be further reduced by other measurements.

The calculation of the isospin symmetry breaking parameter $\delta_C$ in this subshell is not yet fully understood and the results of different groups vary greatly, also contributing to the large uncertainty of $Ft$. Under the assumption that the weak vector current is conserved, our measurement can be used to obtain an experimental value for the parameter of $\delta_C = 0.025(10)$, supporting the calculations of Ormand *et al.*, particularly those employing Woods-Saxon single-particle wave functions. It is highly desirable, however, that the different groups working on these calculations arrive at self-consistent and comparable results that may be used for an experimental check of the CVC hypothesis.

A complete realignment of the beam lines between the RFQ ion beam cooler and buncher and the cooling Penning trap as well as changes in the beam optics based on ion-optical calculations have recently led to an increase in the total efficiency of the apparatus of about a factor of 50. New measurements of the mass of $^{74}$Rb with a more than five times

better precision are therefore now possible and are in fact planned for this year. While the precision of the results presented here was not yet sufficient to contribute to a check of the unitarity of the CKM matrix, such new mass measurements may contribute considerably to tests of the Standard Model.

# A Penning trap theory

Most aspects of ion motion in a Penning trap necessary for an understanding of the functioning of ISOLTRAP, including sideband cooling of the radial motions, have been fully theoretically described by Brown and Gabrielse [Brow1986]. The summary treatment presented here mostly follows the overview given by Ghosh in his comprehensive book on ion traps [Ghos1995]. The notation based on so-called velocity vectors, introduced by Brown and Gabrielse, is abandoned in favor of the more comprehensible Cartesian and cylindrical coordinates.

## A.1 Equations of motion of a charged particle in an ideal Penning trap

A Penning trap is an electromagnetic trap that is obtained from the superposition of a static quadrupolar electric potential and a homogeneous magnetic field. The electric potential $\Phi$ has the form

$$\Phi = \frac{U_0}{4d^2}\left(2z^2 - x^2 - y^2\right), \tag{A.1}$$

where

$$d = \sqrt{\frac{1}{2}\left(z_0^2 + \frac{r_0^2}{2}\right)} \tag{A.2}$$

is the so-called characteristic trap parameter whose magnitude is determined by the distances $r_0$ and $z_0$ from the trap center to the ring electrodes and the end caps, respectively, and $U_0$ is the potential difference applied between them. Figure A.1 shows two typical examples of electrode configurations for the realization of a Penning trap. Electrodes can be machined such that they approximate the equipotential lines of the quadrupolar potential as shown in Fig. A.1(a), though they cannot, of course, extend to infinity. The ideal shape of the potential can also be reproduced reasonably well using hollow cylinder segments, such as those in Fig. A.1(b). In both configurations, traps are often equipped with compensation electrodes that correct for electric-field imperfections due to the shape of the main electrodes.

The electric field $\mathbf{E}$ due to the potential of Eq. (A.1) has the form

$$\mathbf{E} = -\boldsymbol{\nabla}\Phi = \frac{U_0}{2d^2}\begin{bmatrix} x \\ y \\ -2z \end{bmatrix} \tag{A.3}$$

and the magnetic field $\mathbf{B}$ is oriented in the positive $z$ direction:

$$\mathbf{B} = \begin{bmatrix} 0 \\ 0 \\ B \end{bmatrix}. \tag{A.4}$$

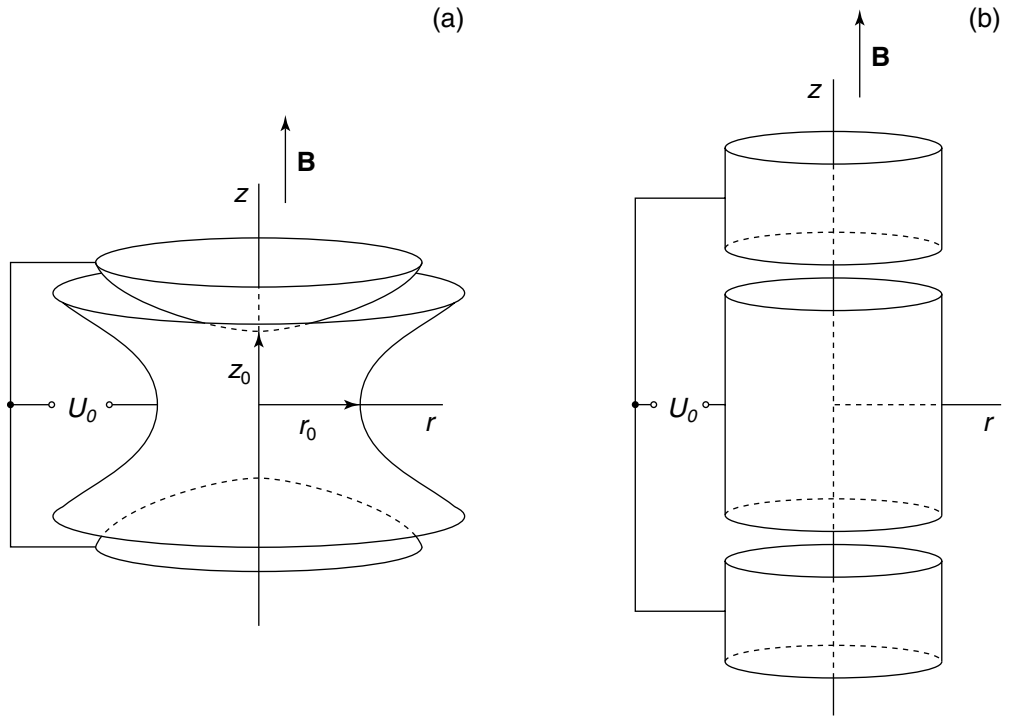


Figure A.1: Sketch of the two typical mechanical realizations of a Penning trap. (a) Hyperboloidal trap. The electrodes approximate the equipotential surfaces of a static quadrupolar potential; (b) Cylindrical Penning trap. The dimensions of the cylinder segments can be chosen such that the electric field on axis near the trap center approaches that of a hyperboloidal trap. In both configurations, correction electrodes may be installed to improve the shape of the electric potential.

A charged particle exposed to this combination of fields experiences a Lorentz force that leads to the following Newtonian equations of motion:

$$\ddot{\mathbf{x}} = \frac{q}{m}\left(\mathbf{E} + \dot{\mathbf{x}} \times \mathbf{B}\right) . \tag{A.5}$$

Using the definitions

$$\omega_z = \sqrt{\frac{qU_0}{md^2}} \tag{A.6}$$

and

$$\omega_c = \frac{qB}{m} , \tag{A.7}$$

these can be rewritten as

$$\begin{bmatrix} \ddot{x} \\ \ddot{y} \\ \ddot{z} \end{bmatrix} - \frac{\omega_z^2}{2} \begin{bmatrix} x \\ y \\ -2z \end{bmatrix} - \omega_c \begin{bmatrix} \dot{y} \\ -\dot{x} \\ 0 \end{bmatrix} = 0 . \tag{A.8}$$

It is obvious from these relations that the radial and axial modes are decoupled. Their equations of motions can therefore be solved independently.

The axial motion is a simple harmonic motion. Its solution has the form

$$z = A_z \cos(\omega_z t - \phi_z)\,. \tag{A.9}$$

The amplitude $A_z$ and phase $\phi_z$ of the oscillation are determined by the initial conditions, *i.e.* the axial position $z(0)$ and velocity $\dot{z}(0)$ at time zero.

In order to solve the equations for the radial motion of the particle, the radial part of Eq. (A.8) is combined into one complex equation by use of the transformation $u = x + iy$:

$$\ddot{u} + i\omega_c \dot{u} - \frac{\omega_z^2}{2} u = 0\,. \tag{A.10}$$

Using the ansatz $u = \mathrm{e}^{-i\omega t}$, one finds the characteristic frequencies $\omega_\pm$:

$$\omega_\pm = \frac{1}{2}\left(\omega_c \pm \sqrt{\omega_c^2 - 2\omega_z^2}\right). \tag{A.11}$$

The general solution for the radial motion of the particle is thus

$$u = A_+ \,\mathrm{e}^{-i\omega_+ t} + A_- \,\mathrm{e}^{-i\omega_- t} \tag{A.12}$$

with the arbitrary complex constants $A_\pm$. Backward transformation to Cartesian coordinates yields the solutions

$$\begin{bmatrix} x \\ y \end{bmatrix} = R_- \begin{bmatrix} \cos(\omega_- t - \phi_-) \\ -\sin(\omega_- t - \phi_-) \end{bmatrix} + R_+ \begin{bmatrix} \cos(\omega_+ t - \phi_+) \\ -\sin(\omega_+ t - \phi_+) \end{bmatrix}. \tag{A.13}$$

The ion thus describes a superposition of three independent and uncoupled oscillations. The radial motions are circular with constant radii $R_\pm$ and frequencies $\omega_\pm$. Figure A.2 shows how the overall motion of an ion is composed of the three independent radial and axial modes. The low-frequency radial mode is called the magnetron motion, the high-frequency oscillation is called the modified cyclotron motion. Since the frequency $\omega_+$ of the cyclotron motion is slightly lower than the cyclotron frequency $\omega_c$ in a purely magnetic field, it is called the reduced cyclotron frequency.

Because of the typical operating conditions of a Penning trap, with a very strong magnetic field and weak electric potential, a hierarchy of the magnitudes of the frequencies of motion is established:

$$\omega_c \approx \omega_+ \gg \omega_z \gg \omega_-\,. \tag{A.14}$$

A Taylor expansion of Eq. (A.11) in $\omega_z$ then yields the following approximate relations for the radial frequencies of motion:

$$\omega_- \approx \frac{U_0}{2d^2 B} \tag{A.15}$$

and

$$\omega_+ \approx \omega_c - \frac{U_0}{2d^2 B}\,, \tag{A.16}$$

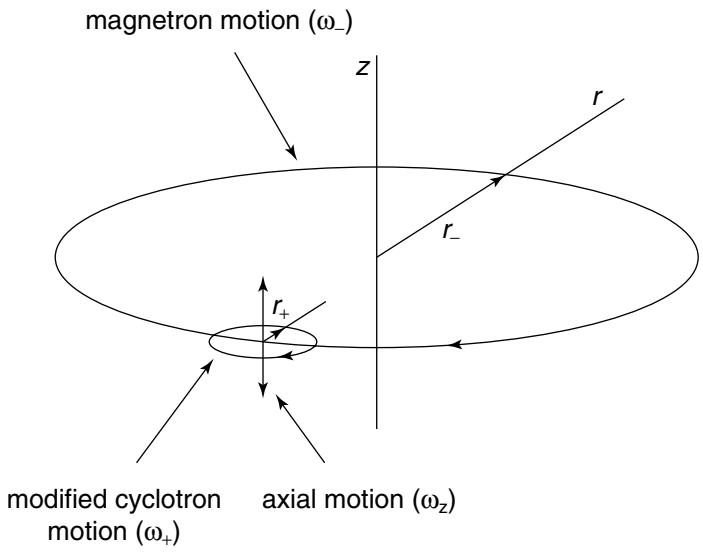


Figure A.2: Motion of a positively charged particle in a Penning trap, composed of the magnetron motion with frequency $\omega_-$, the modified cyclotron motion with frequency $\omega_+$, and the axial motion with frequency $\omega_z$. The configuration of the electric potential and the magnetic field is as in Fig. A.1.

showing that the magnetron frequency $\omega_-$ is approximately independent of the mass and charge of the particle. Furthermore, one can also deduce from Eq. (A.11) the fact that the sum of the magnetron and the reduced cyclotron frequencies of the radial motion of the ion is exactly the cyclotron frequency of an ion in a purely magnetic field:

$$\omega_+ + \omega_- = \omega_c \,. \tag{A.17}$$

This relation is of central importance in the operation of ISOLTRAP and is at the basis both of the buffer gas cooling technique and the TOF resonance technique used for the mass determination. The principle of both these techniques is explained below.

## A.2 Frictional damping

In a gas-filled Penning trap, trapped ions lose kinetic energy in collisions with the buffer gas. For an analytical treatment of the effect of these collisions, the average force exerted on the particle is approximated by a viscous damping force:

$$\mathbf{F}_d = -\delta \dot{\mathbf{x}} \,, \tag{A.18}$$

where the damping coefficient $\delta$ is given by [McDa1973]

$$\delta = \frac{q}{M_{ion}} \cdot \frac{p}{p_N} \cdot \frac{T_N}{T} \,. \tag{A.19}$$

The parameter $M_{\mathrm{ion}}$, the reduced ion mobility coefficient, is tabulated for different ion species and gases [Elli1976, Elli1978]. The fractions $p/p_{\mathrm{N}}$ and $T/T_{\mathrm{N}}$ are the pressure and temperature of the buffer gas, respectively, with respect to normal pressure and temperature.

The equations of motion after addition of this new force become

$$\begin{bmatrix}\ddot{x}\\ \ddot{y}\\ \ddot{z}\end{bmatrix} - \frac{\omega_z^2}{2}\begin{bmatrix}x\\ y\\ -2z\end{bmatrix} - \begin{bmatrix}\omega_{\mathrm{c}}\dot{y} - \frac{\delta}{m}\dot{x}\\ -\omega_{\mathrm{c}}\dot{x} - \frac{\delta}{m}\dot{y}\\ -\frac{\delta}{m}\dot{z}\end{bmatrix} = 0\,. \tag{A.20}$$

The axial motion is still decoupled from the radial motion; it is now simply that of a damped harmonic oscillator. The solution of the axial equation of motion is

$$z = A_z'\,\mathrm{e}^{-(\delta/2m)t}\cos(\omega_z' t - \phi_z') \tag{A.21}$$

with

$$\omega_z' = \sqrt{\omega_z^2 - \left(\frac{\delta}{2m}\right)^2}\,. \tag{A.22}$$

The solution for the radial part of the equations of motion can be obtained in much the same way as in the undamped case. The two equations are combined into one complex equation:

$$\ddot{u} + \left(i\omega_{\mathrm{c}} + \frac{\delta}{m}\right)\dot{u} - \frac{\omega_z^2}{2}u = 0\,. \tag{A.23}$$

Using the ansatz $u = \mathrm{e}^{-i(\omega t-\alpha)}$, the characteristic frequencies $\omega_{1/2}$ and the general solutions of the complex equations of motion are found:

$$\omega_{1/2} = \frac{1}{2}\left\{i\frac{\delta}{m} - \omega_{\mathrm{c}} \pm \sqrt{i\left(\frac{\delta}{m} - \omega_{\mathrm{c}}\right)^2 - 2\omega_z^2}\right\}, \tag{A.24}$$

$$u = A_1\,\mathrm{e}^{-i(\omega_1 t-\alpha_1)} + A_2\,\mathrm{e}^{-i(\omega_2 t-\alpha_2)}\,. \tag{A.25}$$

The complex solution can once again be split into its real and imaginary part to recover the Cartesian solution:

$$\begin{bmatrix}x\\ y\end{bmatrix} = R_-\,\mathrm{e}^{\alpha_- t}\begin{bmatrix}\cos(\omega_- t - \phi_-)\\ -\sin(\omega_- t - \phi_-)\end{bmatrix} + R_+\,\mathrm{e}^{\alpha_+ t}\begin{bmatrix}\cos(\omega_+ t - \phi_+)\\ -\sin(\omega_+ t - \phi_+)\end{bmatrix}. \tag{A.26}$$

with

$$\omega_\pm' = \omega_\pm \pm \Delta\omega\,, \quad \Delta\omega = \frac{1}{16}\cdot\left(\frac{\delta}{m}\right)^2\cdot\frac{8\omega_z^2 + \left(\frac{\delta}{m}\right)^2}{(\omega_{\mathrm{c}}^2 - 2\omega_z^2)^{\frac{3}{2}}}\,. \tag{A.27}$$

The radial motion in the presence of a damping force is thus still a superposition of two circular motions. However, compared to the undamped case, their frequencies are shifted down and up, respectively, by $\Delta\omega$ from the magnetron and reduced cyclotron frequencies $\omega_\mp$. These frequency shifts are however very small and can be neglected in most

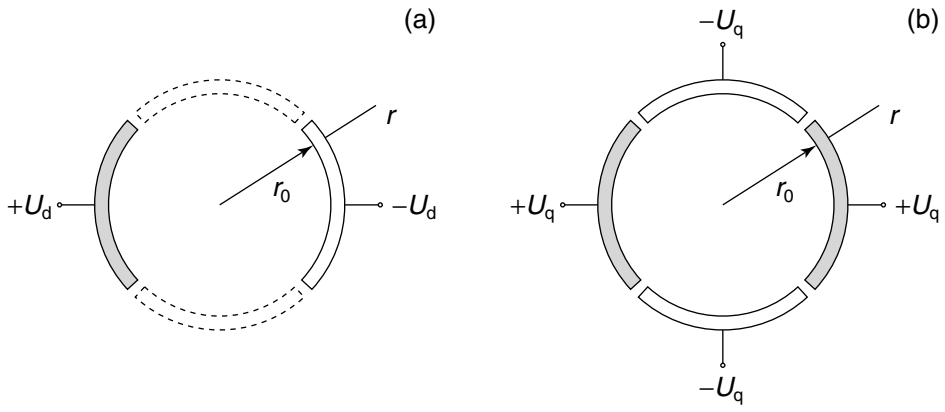


Figure A.3: Electrode geometry for the application of a dipolar and quadrupolar RF potential. The figure shows an azimuthal cut through the ring electrode of a Penning trap, which is four-fold segmented to allow both a dipolar and a quadrupolar excitation. (a) An RF voltage is applied to two opposing segments, leading to a dipolar potential. (b) When the RF potential is applied between the two pairs of opposing segments, the resulting potential has approximately a quadrupolar shape.

cases. More importantly, since the shifts of the two frequencies are equal in magnitude, the sum relation of Eq. (A.17) still holds exactly.

The radii of the motions change exponentially with time constants $\alpha_\pm$ given by

$$\alpha_\pm = -\frac{\delta}{2m}\left\{1 \pm \left(1 + \frac{1}{8}\cdot\frac{8\omega_z^2 + \left(\frac{\delta}{m}\right)^2}{\omega_c^2 - 2\omega_z^2}\right)\right\}. \tag{A.28}$$

While the radius of the modified cyclotron motion decays with a time constant $\alpha_+ \approx -\delta/m$, the radius of the magnetron motion increases with a much smaller time constant $\alpha_- \approx (\delta/2m)\cdot(\omega_z/\omega_c)^2$. Eventually, the particle will be lost from the trap due to the steady increase of its magnetron radius.

## A.3 Dipolar excitation of the motion of the charged particle

The trajectories of particles trapped in a Penning trap can be influenced by the application of additional time-varying electric fields. Two configurations of azimuthal electric RF potentials have proven useful for Penning trap mass spectrometry. They are shown in Fig. A.3. The figure shows azimuthal cuts through the ring electrode, which is segmented four-fold in order to allow the application of dipolar or quadrupolar fields. Figure A.3(a) shows how an RF source is connected in order to achieve dipolar excitation of the trapped

ions. An oscillating dipolar potential has the form

$$\Phi_\mathrm{d} = a\frac{U_\mathrm{d}}{r_0}\cos(\omega_\mathrm{d}t - \phi_\mathrm{d})\cdot x\,, \tag{A.29}$$

where $a$ is a geometric factor that takes into account the fact that in the azimuthal plane the shape of the ring electrode segments doesn't follow the equipotential lines of the dipolar potential. The potential gives rise to an additional electric field:

$$\mathbf{E}_\mathrm{d} = -\boldsymbol{\nabla}\Phi_\mathrm{d} = -a\frac{U_\mathrm{d}}{r_0}\cos(\omega_\mathrm{d}t - \phi_\mathrm{d})\cdot\begin{bmatrix}1\\0\\0\end{bmatrix}, \tag{A.30}$$

which adds an inhomogeneous part to the equations of motion:

$$\begin{bmatrix}\ddot{x}\\ \ddot{y}\\ \ddot{z}\end{bmatrix} - \frac{\omega_z^2}{2}\begin{bmatrix}x\\ y\\ -2z\end{bmatrix} - \omega_\mathrm{c}\begin{bmatrix}\dot{y}\\ -\dot{x}\\ 0\end{bmatrix} = \begin{bmatrix}-k_0\cos(\omega_\mathrm{d}t - \phi_\mathrm{d})\\ 0\\ 0\end{bmatrix} \tag{A.31}$$

with

$$k_0 = a\cdot\frac{q}{m}\cdot\frac{U_\mathrm{d}}{r_0}\,. \tag{A.32}$$

As would be expected, the axial motion remains unaffected. The radial part of the equations of motion can again be combined into one complex equation:

$$\ddot{u} + i\omega_\mathrm{c}\dot{u} - \frac{\omega_z^2}{2}u = -k_0\cos(\omega_\mathrm{d}t - \phi_\mathrm{d})\,. \tag{A.33}$$

It is found that the solution to the radial equations of motion is identical to that in Eq. (A.13), except that the radii of the excited motions, instead of being constant, now are time-varying functions:

$$\begin{bmatrix}x\\ y\end{bmatrix} = R_-(t)\begin{bmatrix}\cos(\omega_- t - \phi_-)\\ -\sin(\omega_- t - \phi_-)\end{bmatrix} + R_+(t)\begin{bmatrix}\cos(\omega_+ t - \phi_+)\\ -\sin(\omega_+ t - \phi_+)\end{bmatrix}. \tag{A.34}$$

For an excitation exactly at the magnetron or the reduced cyclotron frequency, one finds the following result for the time evolution of the radius of the respective motion:

$$R_\pm(t) = \sqrt{R_\pm^2(0) + \frac{k_0^2 t^2}{4(\omega_+ - \omega_-)^2} \mp \frac{R_\pm(0)k_0 t\sin(\phi_\mathrm{d} - \phi_\pm)}{\omega_+ - \omega_-}}\,. \tag{A.35}$$

If furthermore the phase shift $\phi_\mathrm{d} - \phi_\pm$ between the excitation and the resonantly excited motion is exactly equal to $3\pi/2$ (modified cyclotron motion) or to $\pi/2$ (magnetron motion), the relation simplifies to

$$R_\pm(t) = R_\pm(0) + \frac{k_0}{2(\omega_+ - \omega_-)}\cdot t\,. \tag{A.36}$$

The increase of the radial amplitude of the excited motion is then proportional to the duration $T_\mathrm{d}$ of the dipolar excitation and to the amplitude $U_\mathrm{d}$ of the applied dipolar field.

## A.4 Quadrupolar excitation of the motion of the charged particle

Figure A.3(b) shows the electrode configuration for a quadrupolar excitation. An oscillating quadrupolar potential has the form

$$\Phi_\mathrm{q} = a\frac{U_\mathrm{q}}{r_0^2}\cos(\omega_\mathrm{q}t - \phi_\mathrm{q})\cdot(x^2 - y^2)\,, \tag{A.37}$$

where $a$ is again a geometric factor that stems from the shape of the electrode segments. The electric field due to this potential is given by

$$\mathbf{E}_\mathrm{q} = -\boldsymbol{\nabla}\Phi_\mathrm{q} = -2a\frac{U_\mathrm{q}}{r_0^2}\cos(\omega_\mathrm{q}t - \phi_\mathrm{q})\cdot\begin{bmatrix} x \\ -y \\ 0 \end{bmatrix}. \tag{A.38}$$

The equations of motion then become

$$\begin{bmatrix} \ddot{x} \\ \ddot{y} \\ \ddot{z} \end{bmatrix} - \omega_\mathrm{c}\begin{bmatrix} \dot{y} \\ -\dot{x} \\ 0 \end{bmatrix} - \begin{bmatrix} \left\{\frac{\omega_z^2}{2} - 2k_0\cos(\omega_\mathrm{q}t - \phi_\mathrm{q})\right\}x \\ \left\{\frac{\omega_z^2}{2} + 2k_0\cos(\omega_\mathrm{q}t - \phi_\mathrm{q})\right\}y \\ -\omega_z^2 z \end{bmatrix} = 0\,, \tag{A.39}$$

where $k_0$ is now given by

$$k_0 = a\frac{q}{m}\cdot\frac{U_\mathrm{q}}{r_0^2}\,. \tag{A.40}$$

Once again, the axial motion remains unaffected. The radial part of the equations of motion can again be combined into one complex equation:

$$\ddot{u} + i\omega_\mathrm{c}\dot{u} - \left\{\frac{\omega_z^2}{2} - 2ik_0\cos(\omega_\mathrm{q}t - \phi_\mathrm{q})\right\}u = 0\,. \tag{A.41}$$

The solution to the radial equations of motion has the same form as that obtained with dipolar excitation [Eq. (A.34)], but with different time-varying radii $R_\pm(t)$. If the frequency of the exciting RF field is exactly equal to the sum of the frequencies of the radial motion, the radial amplitudes follow the evolution

$$R_\pm(t) = R_\pm(0)\cos\left(\frac{\omega_\mathrm{conv}}{2}t\right) \mp R_\mp(0)\sin\left(\frac{\omega_\mathrm{conv}}{2}t\right)\cos(\phi_\mathrm{q} - \phi_+ - \phi_-)\,, \tag{A.42}$$

where

$$\omega_\mathrm{conv} = \frac{k_0}{2\,(\omega_+ - \omega_-)}\,. \tag{A.43}$$

This type of resonant excitation is also called sideband excitation. If furthermore the phase shift $\phi_\mathrm{q} - \phi_+ - \phi_-$ between the excitation and the radial motions is equal to $\pi$, the relation simplifies to

$$R_\pm(t) = R_\pm(0)\cos\left(\frac{\omega_\mathrm{conv}}{2}t\right) \pm R_\mp(0)\sin\left(\frac{\omega_\mathrm{conv}}{2}t\right). \tag{A.44}$$

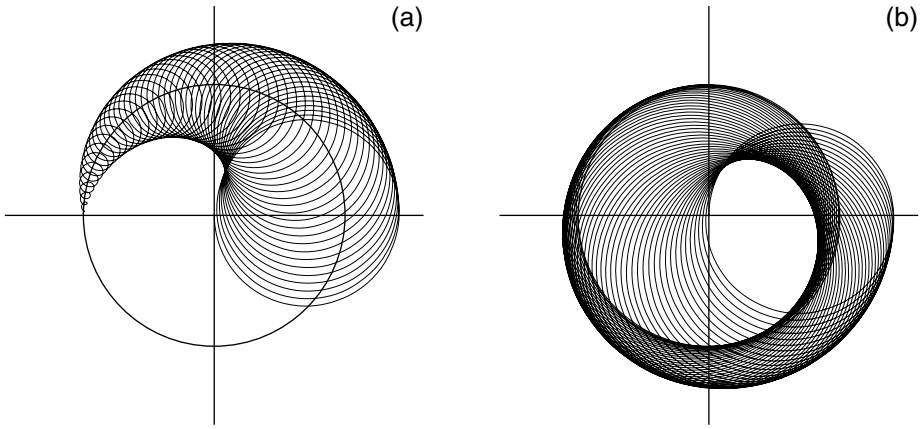


Figure A.4: Conversion of pure magnetron motion into pure cyclotron motion due to an azimuthal quadrupolar excitation at the cyclotron frequency. (a) and (b) show the first and second half of one full conversion. The initial magnetron radius is shown as a circle in both parts of the figure.

This means that the two radial motions are coupled by an excitation at the sum of their frequencies: They are continuously converted into one another with the conversion frequency $\omega_{\mathrm{conv}}$. A complete conversion of one motion into the other is achieved after an excitation duration $T_{\mathrm{q}} = \pi/\omega_{\mathrm{conv}}$. Figure A.4 shows the trajectory of an ion whose motion is excited in this way. The initial pure magnetron motion, indicated by a circle in both parts of the figure, is completely converted into pure modified cyclotron motion. For reasons of clarity, the first part of the conversion ($0 < t \leq \pi/2\omega_{\mathrm{conv}}$) is shown in Fig. A.4(a) and the second part ($\pi/2\omega_{\mathrm{conv}} < t \leq \pi/\omega_{\mathrm{conv}}$) is shown in Fig. A.4(b).

## A.5 Mass-selective buffer gas cooling

As was derived in Sec. A.2, collisions of ions in a Penning trap with buffer gas lead to an increase of their magnetron radius. Eventually, all ions hit the ring electrode and are lost, as shown in Fig. A.5(a). However, we have seen that the radius of the cyclotron motion decreases with a much smaller time constant than the increase of the magnetron radius. A quadrupolar excitation at the cyclotron frequency $\omega_{\mathrm{c}} = \omega_{+} + \omega_{-}$ can be used to continuously convert the magnetron motion into modified cyclotron motion, leading to an overall centering of the trajectories [Sava1991].

The effect of this cooling technique is illustrated in Fig. A.5(b). The combination of a buffer-gas-filled Penning trap with a quadrupolar azimuthal excitation at $\omega_{\mathrm{c}}$ can thus be used to cool ions without losses. Since in reality the viscous damping force of Eq. (A.18) is only an approximation of the collisions with buffer gas atoms or molecules that are really at the origin of the damping, the ions can only be cooled down to the temperature of the buffer gas.

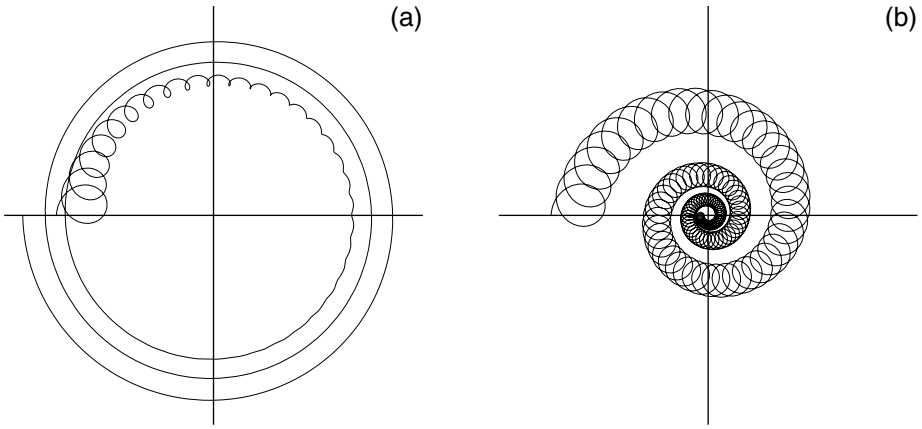


Figure A.5: Azimuthal projection of the trajectory of an ion in a buffer-gas-filled Penning trap. (a) Without excitation, both radial motions of the ion are cooled, leading to an increased magnetron radius. The ion eventually hits the ring electrode and is lost; (b) Resonant quadrupolar excitation at the cyclotron frequency $\omega_c = \omega_+ + \omega_-$ leads to a continuous conversion of magnetron motion into modified cyclotron motion. The radii of both motions are decreased.

Since the cyclotron frequency depends on the mass of the ion [see Eq. (A.7)], this principle can also be used to remove unwanted ion species from the trap. For this purpose, the quadrupolar cooling excitation is preceded by a mass-independent dipolar excitation at the magnetron frequency. This leads to a large initial magnetron radius of all ions. In the subsequent mass-selective cooling step, only the desired species is re-centered. When the ions are ejected through the small orifice in one of the end cap electrodes, the contaminant ions hit the electrode and are not transmitted.

## A.6 Time-of-flight resonance technique

The principle of time-of-flight (TOF) cyclotron resonance detection was originally proposed by Bloch [Bloc1953] and first applied to precision mass measurements by Gräff *et al.* [Gräf1980]. It is a destructive technique whose merit lies in the fact that it can be used to study single ions or samples of very few ions at a time. In this way, changes in the ion motion due to space charge effects are excluded. Moreover, this technique is very well suited for the study of radioactive ions that are only produced in small quantities and that may decay before a large number can be accumulated.

Before being excited with azimuthal RF fields, the ions are essentially at rest in the center of the trap. They are then first subjected to an azimuthal dipolar excitation at the magnetron frequency, leading to an increase of the magnetron radius to $R_- = R_0$. An azimuthal quadrupolar RF excitation is then applied to the ring electrode during a time $T_q = \pi/\omega_{conv}$. In the resonance case, *i.e.* for $\omega_q = \omega_c$, the magnetron motion is converted

into modified cyclotron motion and it follows from Eq. (A.44) that the final cyclotron radius is equal to the initial magnetron radius $R_0$. Because the reduced cyclotron frequency is much higher than the magnetron frequency, the conversion is accompanied by a strong increase in the radial kinetic energy $E_r$:

$$\Delta E_r \propto \omega_+^2 R_0^2 - \omega_-^2 R_0^2 \approx \omega_+^2 R_0^2 \,. \tag{A.45}$$

In the off-resonance case, the conversion is not complete and the increase in kinetic energy is thus lower. The exact functional form of the energy increase depends on the envelope of the excitation signal. If the envelope is rectangular, *i.e.* if the quadrupolar excitation is simply turned on for a time $T_\mathrm{q}$, the final radial kinetic energy is of the form [Köni1995]

$$E_r \propto \frac{\sin^2(\omega_\mathrm{b} T_\mathrm{q})}{\omega_\mathrm{b}^2} \,, \tag{A.46}$$

where

$$\omega_\mathrm{b} = \frac{1}{2}\sqrt{(\omega_\mathrm{q} - \omega_\mathrm{c})^2 + (\omega_\mathrm{conv}/2)^2} \,. \tag{A.47}$$

As the ions are ejected from the trap towards a detector installed on axis outside of the homogeneous-magnetic-field region, the magnetic moment due to their radial motion interacts with the gradient of the magnetic field. They experience an axial force

$$\mathbf{F} = -\boldsymbol{\mu}(\boldsymbol{\nabla} \cdot \mathbf{B}) \tag{A.48a}$$

$$= -\frac{E_r}{B}\frac{\partial B}{\partial z}\hat{z} \tag{A.48b}$$

which leads to a reduction of the time of flight from the trap to the detector upon which the ions eventually impinge.

The total flight time from the trap center at $z = 0$ to the detector at $z = z_1$ is given by the integral

$$T_\mathrm{tot}(\omega_\mathrm{q}) = \int_0^{z_1} \sqrt{\frac{m}{2\left\{E_0 - qU(z) - E_r(\omega_\mathrm{q})B(z)/B\right\}}}\,\mathrm{d}z \,, \tag{A.49}$$

where $E_0$ is the initial axial kinetic energy of the ion. $U(z)$ is the electrostatic potential difference and $B(z)$ the magnitude of the magnetic field along the flight path.

A scan of the quadrupolar-excitation frequency $\omega_\mathrm{q}$ thus produces a characteristic resonance in the time of flight. The theoretically expected line shape of such a resonance, due to an excitation with a rectangular envelope, is shown in Fig. A.6. The shape of this resonance is well understood [Köni1995] and its functional representation can be used to perform a least-squares fit to the data points from which the cyclotron frequency $\omega_\mathrm{c}$ of the ion can be extracted. The ion mass can then be calculated according to Eq. (A.7). The observed sidebands of the resonance are due to the rectangular envelope of the quadrupolar-excitation signal.

It follows from Eqs. (A.45), (A.46), and (A.49) that the depth of the main peak, the so-called time-of-flight effect, is a function of the initial radius $R_0$ of the magnetron motion before the excitation and the completeness of the conversion from magnetron to modified

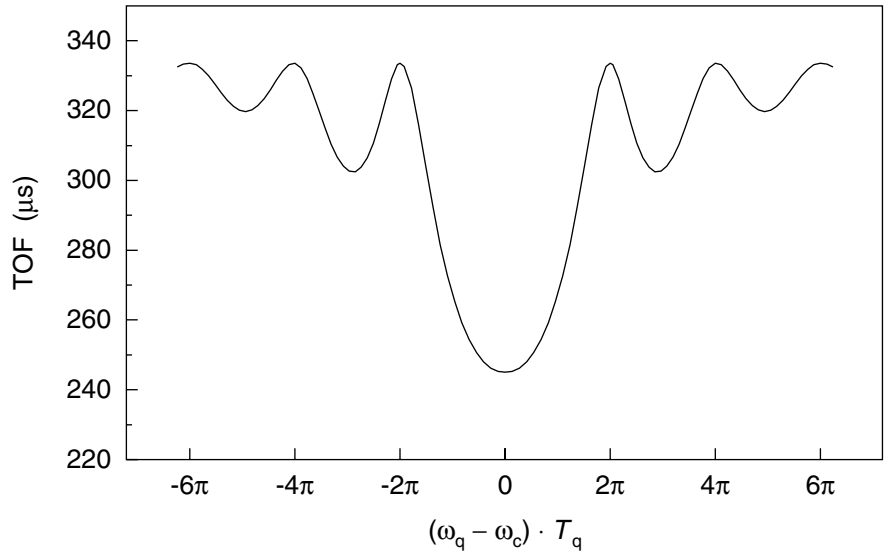


Figure A.6: Theoretical line shape of a time-of-flight cyclotron resonance for a rectangular envelope of the quadrupolar-excitation signal.

cyclotron motion. The latter depends in turn on the amplitude $U_q$ and the duration $T_q$ of the excitation. The line width of the centroid is inversely proportional to $T_q$. For a given ion mass (and thus for a given cyclotron frequency), the frequency resolving power is therefore essentially proportional to the duration of the excitation.

# B Calculation of decay energies for weak nuclear decays

The reaction energy of a nuclear reaction or the decay energy of a nuclear decay are often simply called the $Q$ value. The definition of the $Q$ value varies somewhat throughout the publications, depending on the context in which the quantity is measured or the purpose for which it is calculated or evaluated. In this short summary, the definition found in most nuclear-physics text books, such as [Mich1967] or [Wong1998], is adopted. According to this definition, the energy required for the creation of particles does not count towards the reaction energy, just as the energy liberated in the annihilation of particles does become available and may favor the reaction or decay.

## B.1 Definition of the $Q$ value

The $Q$ value is defined as the difference in the total kinetic energy $T$ of all involved particles before and after the reaction:

$$Q = T_\mathrm{f} - T_\mathrm{i}\,, \tag{B.1}$$

where the indices i and f refer to the initial and final states, respectively. A decay or reaction can only take place when $Q$ is positive (exothermic reaction). A reaction may be favored by supplying kinetic energy, for instance by bombarding a stationary target with an accelerated projectile.

In the case of nuclear decay, the parent nuclide may be assumed to be at rest in the laboratory frame initially and the initial kinetic energy $T_\mathrm{i}$ is thus zero. The decay energy is then equal to the total kinetic energy $T_\mathrm{f}$ of all ejectiles, including the daughter nucleus.

In a decay with only two decay products (apart from the very light neutrino), both ejectiles acquire equal linear momenta in opposite directions. In the non-relativistic limit, *i.e.* for $T \ll M$, the proportion of the kinetic energy associated with this momentum goes like the ratio of the other particle's mass to the total mass:

$$T_2 = T_\mathrm{f} \cdot \frac{M_1}{M_1 + M_2}\,. \tag{B.2}$$

In the case of an electron emitted from a daughter nuclide, the recoil of the nuclide is very weak and need not be taken into account. This is not the case, of course, for emitted nucleons or larger fragments.

When studying the kinematics of decays, atomic masses and atomic-mass differences need to be considered. That's why it is often convenient to carry out the calculations with mass excesses rather than the masses themselves, using the definition of the mass excess given by Eq. (4.1). The mass $M$ can then be expressed in terms of the mass excess $D$ as follows:

$$M(Z,N,E) = (Z+N)\cdot \mathrm{u} + (E-Z)\cdot m_e + D(Z,N)\,, \tag{B.3}$$

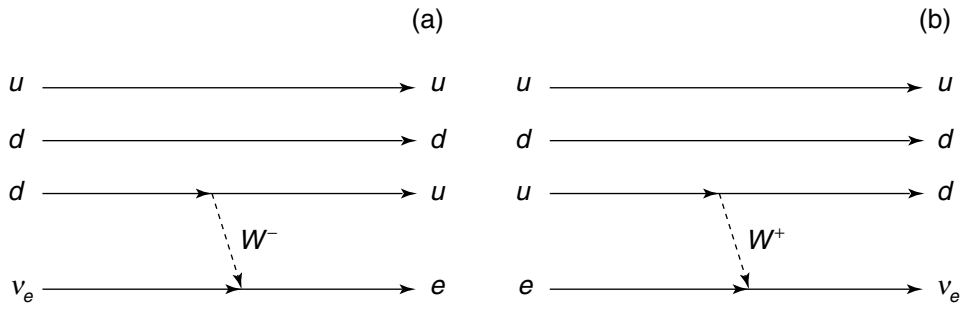


Figure B.1: Basic Feynman diagrams at the quark level for the beta decay. (a) neutron decay and (b) (bound) proton decay. The abscissa represents the time coordinate. All possible decay diagrams are obtained by changing the topology of these diagrams. A particle moving in the negative time direction is equivalent to its antiparticle moving in the positive time direction.

where $Z$ and $N$ are the number of protons and neutrons in the nucleus and $E$ is the number of atomic electrons. The second term stems from the fact that the mass excess is defined for the neutral atom. When a daughter atom is positively or negatively charged, the missing or additional electron mass must be taken into account.

## B.2 Kinematics

The weak decay that has been known for the longest time is the so-called beta decay, named after the characteristic radiation emitted in the form of highly energetic electrons or positrons. In the semi-leptonic beta decay, the exchange of a vector boson between a lepton and a quark contained in the nucleus of an atom leads to a change in flavor of the quark. Figure B.1 shows the basic Feynman diagrams for beta decay at the quark level. All possible decay diagrams are obtained by changing the topology of these diagrams. A particle moving in the negative time direction is equivalent to its antiparticle moving in the positive time direction. Electron ($e^-$ or $\beta^-$) decay of a nuclide corresponds to the Feynman diagram shown in Fig. B.1 (a); Positron ($e^+$) and electron capture ($\epsilon$ or EC) decay share the Feynman diagram of Fig. B.1 (b). Taken together, positron and electron capture decay are also called $\beta^+$ decay.

For a study of decay kinematics, only energy balances are considered. Virtual particles need therefore not be taken into account and can be omitted from the decay diagrams, or rather collapsed into a vertex. Figure B.2 shows the simplified decay diagrams for the three variants of weak nuclear decay. In the following the energy balances for these decay variants are established and their $Q$ values are deduced.

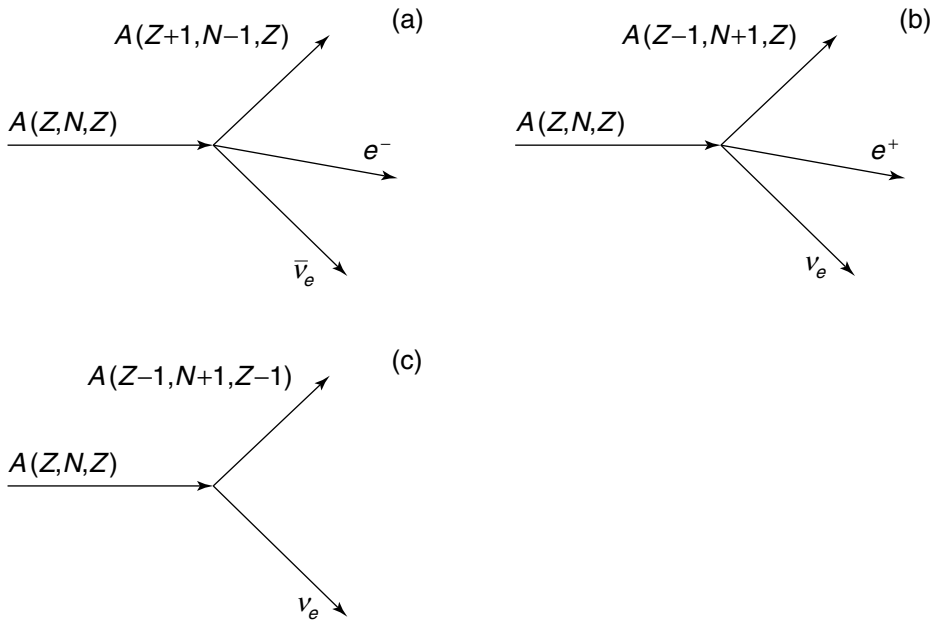


Figure B.2: Simplified decay diagrams for weak nuclear decay. (a) electron ($e^-$ or $\beta^-$) decay; (b) positron ($e^+$) decay; (c) electron capture ($\epsilon$ or EC) decay.

### B.2.1 Electron decay

In electron decay, an atomic neutron is converted into a proton, and an electron and an electron anti-neutrino are emitted. The simplified decay diagram for electron decay is shown in Fig. B.2(a). Using Eq. (B.3), the energy balance can be expressed in terms of the mass excesses:

$$M(Z,N,Z) = M(Z{+}1,N{-}1,Z) + m_e + T_\mathrm{f} \tag{B.4a}$$

$$(Z+N)\cdot u + D(Z,N) = (Z+N)\cdot u - m_e + m_e + D(Z{+}1,N{-}1) + T_\mathrm{f} \tag{B.4b}$$

$$\Longrightarrow D(Z,N) = D(Z{+}1,N{-}1) + T_\mathrm{f}\,. \tag{B.4c}$$

As can be seen from these equations, the masses of the missing atomic electron of the daughter nuclide and of the emitted $\beta$ ray cancel away. Since the kinetic energy of the mother nuclide is very small due to the mass ratio of the ejectiles [see Eq. (B.2)], the decay energy is then just the total final kinetic energy:

$$Q_{e^-} = T_\mathrm{f} = D(Z,N) - D(Z{+}1,N{-}1)\,. \tag{B.5}$$

In mass measurements, the decay energy is often determined from the energy spectrum of the emitted electron. The maximum possible kinetic energy of the electron is equal to $T_\mathrm{f}$ and the end point $E_{0e^-}$ of the energy spectrum then directly yields the mass difference between the mother and the daughter nuclide:

$$D(Z,N) - D(Z{+}1,N{-}1) = E_{0e^-}\,. \tag{B.6}$$

### B.2.2 Positron decay

In positron decay, an atomic proton is converted into a neutron, and a positron (an anti-electron) and an electron neutrino are emitted. The simplified decay diagram is shown in Fig. B.2(b). The energy balance can be derived from the diagram, again in terms of the mass excesses:

$$M(Z,N,Z) = M(Z-1,N+1,Z) + m_e + T_\mathrm{f} \tag{B.7a}$$

$$(Z+N)\cdot u + D(Z,N) = (Z+N)\cdot u + m_e + m_e + D(Z-1,N+1) + T_\mathrm{f} \tag{B.7b}$$

$$\Longrightarrow D(Z,N) = D(Z-1,N+1) + 2m_e + T_\mathrm{f}\,, \tag{B.7c}$$

leading to the following expression for the decay energy:

$$Q_{e^+} = T_\mathrm{f} = D(Z,N) - D(Z-1,N+1) - 2m_e\,. \tag{B.8}$$

Note that in the case of the positron decay, the daughter nuclide is negatively charged and is therefore heavier by one electron mass than a neutral atom would be. In addition, the positron is emitted, requiring another electron mass energy equivalent to be made available.

As is the case for electron decay, the measurement of the decay energy is accessible via a determination of the end point of the energy spectrum of the emitted positrons. However, in the case of positron decay, the mass difference between mother and daughter nuclides doesn't directly correspond to the end point energy $E_{0e^+}$, but two electron masses have to be added:

$$D(Z,N) - D(Z-1,N+1) = E_{0e^+} + 2m_e\,. \tag{B.9}$$

Because the mass difference is the fundamental quantity that is sought, the sum on the right hand side of the previous equation is often called the "total" decay energy and denoted by the symbol $Q_\mathrm{EC}$.

### B.2.3 Electron capture decay

Electron capture decay is represented by the same Feynman diagram as positron decay. The emission of a positron is equivalent to the absorption of an electron. The electron required for the decay stems in fact from the mother atom itself. It is captured from the shell into the nucleus, where the actual weak decay takes place. The vacancy left by the captured electron may be filled by an electron from an outer-lying shell. In the process, a characteristic X ray can be emitted. The energy balance of the EC can again be written down in terms of the mass excesses according to the diagram from Fig. B.2(c):

$$M(Z,N,Z) - B_e = M(Z-1,N+1,Z-1) + T_\mathrm{f} \tag{B.10a}$$

$$(Z+N)\cdot u + D(Z,N) - B_e = (Z+N)\cdot u + D(Z-1,N+1) + T_\mathrm{f} \tag{B.10b}$$

$$\Longrightarrow D(Z,N) - B_e = D(Z-1,N+1) + T_\mathrm{f}\,, \tag{B.10c}$$

where $B_e$ is the ionization energy of the captured electron, which is of the order of 10 eV and can thus in most cases be omitted. This leads to the following expression for the decay energy:

$$Q_\mathrm{EC} = T_\mathrm{f} = D(Z,N) - D(Z-1,N+1)\,. \tag{B.11}$$

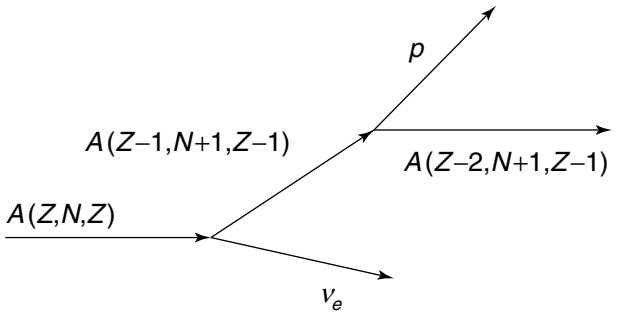


Figure B.3: Simplified decay diagram for beta-delayed proton decay. The special case shown here is that of a proton decay preceded by an electron capture decay (no emitted positron). The ejectile $p$ can also be expressed as $A(1,0,0)$.

Since no positron is emitted in the decay, it is not easily accessible to a kinematic measurement of the decay energy. The mass difference between mother and daughter nuclide is again equal to the decay energy, as was the case for electron decay. This also explains the choice of the symbol $Q_{\mathrm{EC}}$ in connection with the positron decay.

The $e^+$ decay and the EC decay follow the same selection rules and therefore constitute competing processes in many nuclides. Note, however, that the available decay energy for positron decay is lower by two electron masses. This may favor the EC decay or even, depending on the mother and daughter masses, render the $e^+$ decay energetically impossible.

### B.2.4 Beta-delayed proton decay

The daughter nuclides from $\beta^+$ decay are often highly excited, in particular those far from stability or approaching the proton drip line. These nuclides can further decay by proton emission. Since the density of states in the intermediate nuclei is very high at the levels that are populated by the $\beta^+$ decay, they can be considered a continuum. This assumption can be used to extract the total decay energy from the energy spectrum of the emitted proton, as is shown in the following.

Figure B.3 shows the simplified decay diagram for beta-delayed proton decay. The diagram shown here represents electron capture decay followed by proton decay. The similar diagram for positron decay followed by proton decay is not shown; the difference between the two decay channels is analogous to that between EC and $e^+$ decay. Just as for simple positron or electron capture decay, the actual branching ratios between the two decay channels vary strongly with $Q_{\mathrm{EC}}$ and depend on the selection rules [Bamb1977]. They can be determined experimentally.

The energy balance in terms of the mass excesses derived from the figure presents

itself as follows:

$$M(Z,N,Z) - B_e = M(Z{-}2,N{+}1,Z{-}1) + M(1,0,0) + T_\mathrm{f} \tag{B.12a}$$

$$\begin{aligned}(Z+N)\cdot u + D(Z,N) - B_e &= (Z+N-1)\cdot u + m_e + D(Z{-}2,N{+}1)\\ &\quad + u - m_e + D(^1\mathrm{H}) + T_\mathrm{f}\end{aligned} \tag{B.12b}$$

$$\Longrightarrow D(Z,N) - B_e = D(Z{-}2,N{+}1) + D(^1\mathrm{H}) + T_\mathrm{f}\,, \tag{B.12c}$$

and, again neglecting the electron binding energy $B_e$, leads to the decay energy

$$Q_{\epsilon p} = T_\mathrm{f} = D(Z,N) - D(Z{-}2,N{+}1) - D(^1\mathrm{H})\,. \tag{B.13}$$

If the total decay energy is to be determined from the end point of the proton energy spectrum, one must take into account the fact that the daughter nuclide $A(Z{-}2,N{+}1,Z{-}1)$ will carry the same momentum as the ejected proton. It will therefore also carry part of the final kinetic energy, which can never entirely be available to the proton only. The proportion of kinetic energy carried by the daughter nuclide is the inverse ratio of its mass $M(Z{-}2,N{+}1,Z{-}1)$ to that of the proton. From a measurement of the proton end point energy, the difference between the mass of the mother nuclide and that of the daughter nuclide can then be calculated as follows:

$$D(Z,N) - D(Z{-}2,N{+}1) = D(^1\mathrm{H}) + E_{0p}\cdot\frac{M(Z{-}2,N{+}1,Z{-}1) + M(^1\mathrm{H})}{M(Z{-}2,N{+}1,Z{-}1)} \tag{B.14a}$$

$$\approx D(^1\mathrm{H}) + E_{0p}\cdot\frac{Z+N}{Z+N-1}\,. \tag{B.14b}$$

That quantity is also often denoted by the symbol $Q_\mathrm{EC} - B_p$, where $B_p$ stands for the nuclear binding energy of the emitted proton.

# Bibliography


[Abel2000] H. Abele. *The Standard Model and the Neutron β-Decay*. Nucl. Instrum. Methods A **440**, 499–510 (2000).

[Agui1986] M. Aguilar-Benitez *et al.* *Review of Particle Properties*. Phys. Lett. B **170**, 1–350 (1986).

[Ande1962] P. W. Anderson. *Theory of Flux Creep in Hard Superconductors*. Phys. Rev. Lett. **9**(7), 309–11 (1962).

[Ande1964] P. W. Anderson and Y. B. Kim. *Hard Superconductivity: Theory of the Motion of Abrikosov Flux Lines*. Rev. Mod. Phys. **39**, 39–43 (1964).

[Anto1997] M. S. Antony, A. Pape, and J. Britz. *Coulomb Displacement Energies Between Analog Levels For $3 \leq A \leq 239$*. At. Data Nucl. Data Tables **66**(1), 1–63 (1997).

[Audi1982] G. Audi, M. Epherre, C. Thibault, A. H. Wapstra, and K. Bos. *Masses of Rb, Cs and Fr Isotopes*. Nucl. Phys. A **378**, 443–60 (1982).

[Audi1993] G. Audi and A. H. Wapstra. *The 1993 Atomic Mass Evaluation*. Nucl. Phys. A **565**, 1–397 (1993).

[Audi1995] G. Audi and A. H. Wapstra. *The 1995 Update to the Atomic Mass Evaluation*. Nucl. Phys. A **595**, 409–80 (1995).

[Audi1997] G. Audi, O. Bersillon, J. Blachot, and A. H. Wapstra. *The NUBASE Evaluation of Nuclear and Decay Properties*. Nucl. Phys. A **624**, 1–124 (1997).

[Audi2001] G. Audi. *The Evaluation of Atomic Masses*. In D. Lunney *et al.* (eds.), *Proc. of the APAC2000 Conference*, Hyp. Int. **132**, 7–34 (2001).

[Audi2002] G. Audi. Private communication (2002).

[Ball2001] G. C. Ball, S. Bishop, J. A. Behr, G. C. Boisvert, P. Bricault, J. Cerny, J. M. D'Auria, M. Dombsky, J. C. Hardy, V. Iacob, J. R. Leslie, T. Lindner, J. A. Macdonald, H.-B. Mak, D. M. Moltz, J. Powell, G. Savard, and I. S. Towner. *Precise Half-Life Measurement for the Superallowed $0^+ \longrightarrow 0^+$ β Emitter $^{74}$Rb: First Results from the New Radioactive Beam Facility (ISAC) at TRIUMF*. Phys. Rev. Lett. **86**(8), 1454–7 (2001).

[Bamb1977] W. Bambynek, H. Behrens, M. H. Chen, B. Crasemann, M. L. Fitzpatrick, K. W. D. Ledingham, H. Genz, M. Mutterer, and R. L. Intemann. *Orbital Electron Capture by the Nucleus*. Rev. Mod. Phys. **49**(1), 77–221 (1977).

[Beck1997a] D. Beck. *Massenbestimmung instabiler Isotope der Seltenen Erden um $^{146}$Gd mit dem ISOLTRAP-Spektrometer*. Ph.D. thesis, University of Mainz (1997).

[Beck1997b] D. Beck, F. Ames, G. Audi, G. Bollen, H.-J. Kluge, A. Kohl, M. König, D. Lunney, H. Raimbault-Hartmann, S. Schwarz, and J. Szerypo. *Towards Higher Accuracy With the ISOLTRAP Mass Spectrometer*. Nucl. Instrum. Methods B **126**, 374–7 (1997).

[Beck1999] F. Becker, W. Korten, F. Hannchi, P. Paris, N. Buforn, C. Chandler, M. Houry, H. Hübel, A. Jansen, Y. Le Coz, C. F. Liang, A. Lopez-Martens, R. Lucas, E. Mergel, P. H. Regan, G. Schönwasser, and C. Theisen. *Investigation of Prolate-Oblate Shape-Coexistence in $^{74}$Kr*. Eur. Phys. J. A **4**, 103–5 (1999).

[Berg2002] I. Bergström, C. Carlberg, T. Fritioff, G. Douysset, R. Schuch, and J. Schönfelder. *SMILETRAP – A Penning Trap Facility for Precision Mass Measurements Using Highly Charged Ions*. Nucl. Instrum. Methods A (2002), in press.

[Blau2002a] K. Blaum, G. Bollen, F. Herfurth, A. Kellerbauer, H.-J. Kluge, M. Kuckein, E. Sauvan, C. Scheidenberger, and L. Schweikhard. *Carbon Clusters for Absolute Mass Measurements at ISOLTRAP*. In M. Leino *et al.* (eds.), *Proc. of the ENAM2001 Conference*, Eur. Phys. J. A (2002), in press.

[Blau2002b] K. Blaum, G. Huber, H.-J. Kluge, and L. Schweikhard. Eur. Phys. J. D (2002), to be published.

[Bloc1953] F. Bloch. *Experiments on the g-Factor of the Electron*. Physica **19**, 821–31 (1953).

[Boll1992] G. Bollen, H.-J. Kluge, M. König, T. Otto, G. Savard, H. Stolzenberg, R. B. Moore, G. Rouleau, G. Audi, and the ISOLDE Collaboration. *Resolution of Nuclear Ground and Isomeric States by a Penning Trap Mass Spectrometer*. Phys. Rev. C **46**, R2140–3 (1992).

[Boll1996] G. Bollen, S. Becker, H.-J. Kluge, M. König, R. B. Moore, T. Otto, H. Raimbault-Hartmann, G. Savard, L. Schweikhard, H. Stolzenberg, and the ISOLDE Collaboration. *ISOLTRAP: A Tandem Penning Trap System for Accurate On-Line Mass Determination of Short-Lived Isotopes*. Nucl. Instrum. Methods A **368**, 675–97 (1996).

[Boll2001] G. Bollen. *Mass Measurements of Short-Lived Nuclides with Ion Traps*. Nucl. Phys. A **693**, 3–18 (2001).

[Brad1999] M. P. Bradley, J. V. Porto, S. Rainville, J. K. Thompson, and D. E. Pritchard. *Penning Trap Measurements of the Masses of $^{133}$Cs, $^{87,85}$Rb, and $^{23}$Na with Uncertainties ≤0.2 ppb*. Phys. Rev. Lett. **83**, 4510–3 (1999).

[Brow1986] L. S. Brown and G. Gabrielse. *Geonium Theory: Physics of a Single Electron or Ion in a Penning Trap*. Rev. Mod. Phys. **58**(1), 233–311 (1986).

[Burk1986] B. L. Burks, R. L. Varner, and E. J. Ludwig. *Q-Value Determination for the $^{80}Kr(d,p)^{81}Kr$ Reaction*. Phys. Rev. C **34**(6), 2316–8 (1986).

[Chan1997] C. Chandler, P. H. Regan, C. J. Pearson, B. Blank, A. M. Bruce, W. N. Catford, N. Curtis, S. Czajkowski, W. Gelletly, R. Grzywacz, Z. Janas, M. Lewitowicz, C. Marchand, N. A. Orr, R. D. Page, A. Petrovici, A. T. Reed, M. G. Saint-Laurent, S. M. Vincent, R. Wadsworth, D. D. Warner, and J. S. Winfield. *Evidence For a Highly Deformed Oblate $0^+$ State in $^{74}_{36}Kr$*. Phys. Rev. C **56**(6), R2924–8 (1997).

[Egge1994] B. R. Eggen, R. L. Johnston, and J. N. Murrell. *Carbon Cluster Structures and Stabilities Predicted from Solid-State Potentials*. J. Chem. Soc. Farad. Trans. **90**(20), 3029–37 (1994).

[Eich1962] E. Eichler, G. D. O'Kelley, R. L. Robinson, J. A. Marinsky, and N. R. Johnson. *Nuclear Levels of $Ge^{74}$*. Nucl. Phys. **35**, 625–44 (1962).

[Eins1905] A. Einstein. *Ist die Trägheit eines Körpers von seinem Energieinhalt abhängig?* Ann. Phys. **18**(3), 639–41 (1905).

[Elli1976] H. W. Ellis, R. Y. Pai, E. W. McDaniel, E. A. Mason, and L. A. Viehland. *Transport Properties of Gaseous Ions Over a Wide Energy Range*. At. Data Nucl. Data Tables **17**, 177–210 (1976).

[Elli1978] H. W. Ellis, E. W. McDaniel, D. L. Albritton, L. A. Viehland, S. L. Lin, and E. A. Mason. *Transport Properties of Gaseous Ions Over a Wide Energy Range: Part II*. At. Data Nucl. Data Tables **22**, 179–217 (1978).

[Erda1972] B. R. Erdal, L. Westgaard, J. Zylicz, and E. Roeckl. *New Isotopes $^{73}Zn$ and $^{74}Zn$*. Nucl. Phys. A **194**, 449–57 (1972).

[Farh1995] A. R. Farhan. *Nuclear Data Sheets Update for A = 74*. Nucl. Data Sheets **74**(4), 529–610 (1995).

[Frit2001] T. Fritioff, C. Carlberg, G. Douysset, R. Schuch, and I. Bergström. *A New Determination of the $^4He$ and $^3He$ Masses in a Penning Trap*. Eur. Phys. J. D **15**, 141–3 (2001).

[Ghos1995] P. K. Ghosh. *Ion Traps*. Clarendon Press, Oxford (1995).

[Goss1959] C. R. Gossett and J. W. Butler. *Neutron Thresholds in the $^{51}V(p,n)^{51}Cr$, $^{55}Mn(p,n)^{55}Fe$, $^{70}Zn(p,n)^{70}Ga$, and $^{75}As(p,n)^{75}Se$ Reactions*. Phys. Rev. **113**(1), 246–51 (1959).

[Gräf1980] G. Gräff, H. Kalinowsky, and J. Traut. *A Direct Determination of the Proton Electron Mass Ratio*. Z. Phys. A **297**, 35–9 (1980).

[Groo2000] D. E. Groom *et al.* *Review of Particle Physics*. Eur. Phys. J. C **15**(1–4), 1–878 (2000).

[Hagb1994] E. Hagberg, V. T. Kosowsky, J. C. Hardy, I. S. Towner, J. G. Hykawy, G. Savard, and T. Shinozuka. *Tests of Isospin Mixing Corrections in Superallowed $0^+ \longrightarrow 0^+$ $\beta$ Decays*. Phys. Rev. Lett. **73**(3), 196–9 (1994).

[Hard1981] J. C. Hardy, T. Faestermann, H. Schmeing, J. A. Macdonald, H. R. Andrews, J. S. Geiger, R. L. Graham, and K. P. Jackson. *$T_Z = \frac{1}{2}$ $\beta$-Delayed Proton Precursors*. Nucl. Phys. A **371**, 349–63 (1981).

[Hard1990] J. C. Hardy, I. S. Towner, V. T. Koslowsky, E. Hagberg, and H. Schmeing. *Superallowed $0^+ \longrightarrow 0^+$ Nuclear $\beta$-Decays: A Critical Survey With Tests of CVC and the Standard Model*. Nucl. Phys. A **509**, 429–60 (1990).

[Hard2001] J. C. Hardy and I. S. Towner. *Standard-Model Tests with Superallowed $\beta$-Decay: An Important Application of Very Precise Mass Measurements*. In D. Lunney *et al.* (eds.), *Proc. of the APAC2000 Conference*, Hyp. Int. **132**, 115–26 (2001).

[Herf2001a] F. Herfurth. *A New Ion Beam Cooler and Buncher for ISOLTRAP and Mass Measurements of Radioactive Argon Isotopes*. Ph.D. thesis, University of Heidelberg (2001).

[Herf2001b] F. Herfurth, J. Dilling, A. Kellerbauer, G. Bollen, S. Henry, H.-J. Kluge, E. Lamour, D. Lunney, R. B. Moore, C. Scheidenberger, S. Schwarz, G. Sikler, and J. Szerypo. *A Linear Radiofrequency Ion Trap For Accumulation, Bunching, and Emittance Improvement of Radioactive Ion Beams*. Nucl. Instrum. Methods A **469**, 254–75 (2001).

[Herf2001c] F. Herfurth, J. Dilling, A. Kellerbauer, G. Audi, D. Beck, G. Bollen, S. Henry, H.-J. Kluge, D. Lunney, R. B. Moore, C. Scheidenberger, S. Schwarz, G. Sikler, and J. Szerypo. *Towards Shorter-Lived Nuclides in ISOLTRAP Mass Measurements*. In D. Lunney *et al.* (eds.), *Proc. of the APAC2000 Conference*, Hyp. Int. **132**, 309–14 (2001).

[Herf2002] F. Herfurth, A. Kellerbauer, F. Ames, G. Audi, D. Beck, K. Blaum, G. Bollen, O. Engels, H.-J. Kluge, D. Lunney, R. B. Moore, M. Oinonen, E. Sauvan, C. Scheidenberger, S. Schwarz, G. Sikler, C. Weber, and the ISOLDE Collaboration. *Accurate Mass Measurements of Very Short-Lived Nuclei: Prerequisites for High-Accuracy Investigations of Superallowed $\beta$ Decays*. In M. Leino *et al.* (eds.), *Proc. of the ENAM2001 Conference*, Eur. Phys. J. A (2002), in press.

[Hoyl1990] F. Hoyler, J. Jolie, G. G. Colvin, H. G. Börner, K. Schreckenbach, P. Van Isacker, P. Fettweis, H. Göktürk, J. C. Dehaes, R. F. Casten, D. D. Warner, and A. M. Bruce. *Spectroscopy of the Odd-Odd Nucleus $^{76}$As and Its Supersymmetric Description*. Nucl. Phys. A **512**, 189–216 (1990).

[Jaus1987] W. Jaus and G. Rasche. *Radiative Corrections to $0^+$–$0^+$ $\beta$ Transitions*. Phys. Rev. D **35**(11), 3420–2 (1987).

[John1964] C. H. Johnson, C. C. Trail, and A. Galonsky. *Thresholds for (p,n) Reactions on 26 Intermediate-Weight Nuclei*. Phys. Rev. **136**(6B), 1719–29 (1964).

[Kato1969] T. Katoh, T. Morii, H. Inoue, Y. Yoshizawa, H. Gotoh, and E. Sakai. *Beta- and Gamma-Ray Spectroscopy of $^{80m}Br$*. J. Phys. Soc. Japan **26**(5), 1071–4 (1969).

[Kell2001] A. Kellerbauer, T. Kim, R. B. Moore, and P. Varfalvy. *Buffer Gas Cooling of Ion Beams*. Nucl. Instrum. Methods A **469**, 276–85 (2001).

[Kell2002] A. Kellerbauer, F. Herfurth, E. Sauvan, K. Blaum, H.-J. Kluge, C. Scheidenberger, G. Bollen, M. Kuckein, and L. Schweikhard. *Carbon Cluster Ions for a Study of the Accuracy of ISOLTRAP*. In J. Hangst *et al.* (eds.), *Proc. of the APAC2001 Conference*, Hyp. Int. (2002), in press.

[Kett1999] J. B. Ketterson and S. N. Song. *Superconductivity*. Cambridge University Press, Cambridge (1999).

[Köni1995] M. König, G. Bollen, H.-J. Kluge, T. Otto, and J. Szerypo. *Quadrupole Excitation of Stored Ion Motion at the True Cyclotron Frequency*. Int. J. Mass Spectrom. Ion Proc. **142**, 95–116 (1995).

[Köst2002] U. Köster. Private communication (2002).

[Krät1990] W. Krätschmer, L. D. Lamb, K. Fostiropoulos, and D. R. Huffman. *Solid $C_{60}$: A New Form of Carbon*. Nature **347**, 354–8 (1990).

[Krot1985] H. W. Kroto, J. R. Heath, S. C. O'Brien, R. F. Curl, and R. E. Smalley. *$C_{60}$: Buckminsterfullerene*. Nature **318**, 162–3 (1985).

[Krot2000] H. W. Kroto. *$C_{60}$ and Carbon: A Postbuckminsterfullerene Perspective*. Int. J. Mass Spectrom. Ion Proc. **200**, 253–60 (2000).

[Kugl2000] E. Kugler. *The ISOLDE Facility*. Hyp. Int. **129**, 23–42 (2000).

[Lifs2000] C. Lifshitz. *Carbon Clusters*. Int. J. Mass Spectrom. Ion Proc. **200**, 423–42 (2000).

[Lunn2000] D. Lunney and G. Bollen. *Extending and Refining the Nuclear Mass Surface With ISOLTRAP and MISTRAL*. Hyp. Int. **129**, 249–269 (2000).

[Manb2001] F. R. Manby, R. L. Johnston, and C. Roberts. *Predatory Genetic Algorithms*. Commun. Math. Comp. Chem. **38**, 111–22 (2001).

[Mats1981] S. Matsuki, N. Sakamoto, K. Ogino, Y. Kadota, T. Tanabe, and Y. Okuma. *Level Structure of $^{76}$Kr from the $^{78}$Kr(p,t)$^{76}$Kr Reaction*. Nucl. Phys. A **370**, 1–12 (1981).

[McDa1973] E. W. McDaniel and E. A. Mason. *The Mobility and Diffusion of Ions in Gases*. Wiley, New York (1973).

[Mich1967] A. Michalowicz. *Kinematics of Nuclear Reactions*. Iliffe Books Ltd., London (1967).

[Mohr1999] P. J. Mohr and B. N. Taylor. *CODATA Recommended Values of the Fundamental Physical Constants: 1998*. J. Phys. Chem. Ref. Data **28**, 1713–852 (1999).

[Molt1982] D. M. Moltz, K. S. Toth, R. E. Tribble, R. E. Neese, and J. P. Sullivan. *Masses of $^{76}$Kr and $^{74}$Kr*. Phys. Rev. C **26**(5), 1914–20 (1982).

[Molt1987] D. M. Moltz, A. C. Betker, J. P. Sullivan, R. H. Burch, C. A. Gagliardi, R. E. Tribble, K. S. Toth, and F. T. Avignone, III. *Masses of $^{77}$Kr and $^{75}$Kr*. Phys. Rev. C **35**(4), 1275–9 (1987).

[Nxum1993] J. N. Nxumalo, J. G. Hykawy, P. P. Unger, C. A. Lander, R. C. Barber, K. S. Sharma, and H. E. Duckworth. *Energy Available for the Double Beta Decay of $^{82}$Se*. Phys. Lett. B **302**, 13–4 (1993).

[Ober1997] J. Oberheide, P. Wilhelms, and M. Zimmer. *New Results on the Absolute Ion Detection Efficiency of a Microchannel Plate*. Meas. Sci. Technol. **8**, 351–4 (1997).

[Oino2001] M. Oinonen, J. Äystö, P. Baumann, J. Cederkäll, S. Courtin, P. Dessagne, S. Franchoo, H. Fynbo, M. Górska, J. Huikari, A. Jokinen, A. Knipper, U. Köster, G. Le Scornet, C. Miehé, A. Nieminen, T. Nilsson, Y. Novikov, K. Peräjärvi, E. Poirier, A. Popov, D. M. Seliverstov, T. Siiskonen, H. Simon, O. Tengblad, P. Van Duppen, G. Walter, L. Weissman, and K. Wilhelmsen-Rolander. *Non-Analog $\beta$ Decay of $^{74}$Rb*. Phys. Lett. B **511**, 145–50 (2001).

[Orma1989] W. E. Ormand, B. A. Brown, and B. R. Holstein. *Limits on the Presence of Scalar and Induced-Scalar Currents in Superallowed $\beta$ Decay*. Phys. Rev. C **40**(6), 2914–7 (1989).

[Orma1995] W. E. Ormand and B. A. Brown. *Isospin-Mixing Corrections for fp-Shell Fermi Transitions*. Phys. Rev. C **52**(5), 2455–60 (1995).

[Otto1993] T. Otto. *Penningfallen-Massenspektrometrie an neutronenarmen Rubidium- und Strontium-Isotopen*. Ph.D. thesis, University of Mainz (1993).

[Otto1994] T. Otto, G. Bollen, G. Savard, L. Schweikhard, H. Stolzenberg, G. Audi, R. B. Moore, G. Rouleau, J. Szerypo, and Z. Patyk. *Penning-Trap Mass Measurements of Neutron-Deficient Rb and Sr Isotopes*. Nucl. Phys. A **567**, 281–302 (1994).

[Quin1998] T. J. Quinn and I. M. Mills. *The International System of Units (SI)*. Bureau International des Poids et Mesures, Sèvres (France), 7th edition (1998).

[Raim1997] H. Raimbault-Hartmann, D. Beck, G. Bollen, M. König, H.-J. Kluge, E. Schark, J. Stein, S. Schwarz, and J. Szerypo. *A Cylindrical Penning Trap for Capture, Mass Selective Cooling, and Bunching of Radioactive Ion Beams*. In G. Münzenberg *et al.* (eds.), *Proc. of the 13th EMIS Conference*, Nucl. Instrum. Methods B **126**, 378–82 (1997).

[Ries1963] R. R. Ries, R. A. Damerow, and W. H. Johnson, Jr. *Atomic Masses from Gallium to Molybdenum*. Phys. Rev. **132**(4), 1662–72 (1963).

[Roec1974] E. Roeckl, D. Lode, K. Bächmann, B. Neidhart, G. K. Wolf, W. Lauppe, N. Kaffrell, and P. Patzelt. *Decay Properties of Neutron Deficient Kr Isotopes*. Z. Phys. **266**, 65–7 (1974).

[Rudo1997] D. Rudolph, C. Baktash, C. J. Gross, W. Satula, R. Wyss, I. Birriel, M. Devlin, H.-Q. Jin, D. R. LaFosse, F. Lerma, J. X. Saladin, D. G. Sarantites, G. N. Sylvan, S. L. Tabor, D. F. Winchell, V. Q. Wood, and C. H. Yu. *Systematics of Even-Even $T_z$ = 1 Nuclei in the A = 80 Region: High-Spin Rotational Bands in $^{74}$Kr, $^{78}$Sr, and $^{82}$Zr*. Phys. Rev. C **56**(1), 98–117 (1997).

[Saga1996] H. Sagawa, V. G. Nguyen, and T. Suzuki. *Effect of Isospin Mixing on Superallowed Fermi β Decay*. Phys. Rev. C **53**(5), 2163–70 (1996).

[Sava1991] G. Savard, S. Becker, G. Bollen, H.-J. Kluge, R. B. Moore, T. Otto, L. Schweikhard, H. Stolzenberg, and U. Wiess. *A New Cooling Technique for Heavy Ions in a Penning Trap*. Phys. Lett. A **158**, 247–52 (1991).

[Sche2002] C. Scheidenberger, G. Bollen, F. Herfurth, A. Kellerbauer, H.-J. Kluge, M. Koizumi, S. Schwarz, and L. Schweikhard. *Production and Trapping of Carbon Clusters for Absolute Mass Measurements at ISOLTRAP*. In H. Ravn *et al.* (eds.), *Proc. of the RNB2000 Conference*, Nucl. Phys. A **701**, 574c–8c (2002).

[Schm1973] H. Schmeing, J. C. Hardy, R. L. Graham, J. S. Geiger, and K. P. Jackson. *A New N = Z Isotope: Krypton 72*. Phys. Lett. B **44**(5), 449–52 (1973).

[Schm1975] H. Schmeing, J. C. Hardy, R. L. Graham, and J. S. Geiger. *The Decay of $^{74}$Kr*. Nucl. Phys. A **242**, 232–42 (1975).

[Sirl1978] A. Sirlin. *Current Algebra Formulation of Radiative Corrections in Gauge Theories and the Universality of the Weak Interactions*. Rev. Mod. Phys. **50**(3), 573–605 (1978).

[Sirl1986] A. Sirlin and R. Zuchini. *Accurate Verification of the Conserved-Vector-Current and Standard-Model Predictions*. Phys. Rev. Lett. **57**(16), 1994–7 (1986).

[Sirl1987] A. Sirlin. *Remarks Concerning the $O(Z\alpha^2)$ Corrections to Fermi Decays, Conserved-Vector-Current Predictions, and Universality*. Phys. Rev. D **35**(11), 3423–7 (1987).

[Step1987] G. S. F. Stephans, H. T. Fortune, L. C. Bland, M. Carchidi, R. Gilman, G. P. Gilfoyle, and J. W. Sweet. *Distribution of Proton Spectroscopic Strengths in the Odd-A Rb Isotopes*. Phys. Rev. C **35**(5), 2033–48 (1987).

[Thul1955] S. Thulin. *Studies in Nuclear Spectroscopy with Electromagnetically Separated Gaseous Isotopes II: Disintegration of Some Krypton and Xenon Isotopes*. Arkiv Fysik **9**(11), 137–95 (1955).

[Town1973] I. S. Towner and J. C. Hardy. *Superallowed $0^+ \longrightarrow 0^+$ Nuclear $\beta$-Decays*. Nucl. Phys. A **205**, 33–55 (1973).

[Town1999] I. S. Towner and J. C. Hardy. *The Current Status of $V_{ud}$*. In P. Herczeg *et al.* (eds.), *Proc. of the 5th International WEIN Symposium*, pages 338–59, World Scientific, Singapore (1999).

[Town2002] I. S. Towner. Private communication (2002).

[VanD1992] R. S. Van Dyck, Jr., D. L. Farnham, and P. B. Schwinberg. *A Compensated Penning Trap Mass Spectrometer and the $^3$H–$^3$He Mass Difference*. J. Mod. Optics **39**(2), 243–55 (1992).

[Viei2002] N. Vieira, G. Audi, Z. Djouadi, H. Doubre, C. Gaulard, S. Henry, D. Lunney, M. de Saint Simon, C. Thibault, G. Bollen, and the ISOLDE Collaboration. *MISTRAL: A High Precision Mass Spectrometer for Short-Lived Nuclides*. In M. Leino *et al.* (eds.), *Proc. of the ENAM2001 Conference*, Eur. Phys. J. A (2002), in press.

[Wadd1956] R. C. Waddell and E. N. Jensen. *Decay Scheme of $Br^{82}$*. Phys. Rev. **102**(3), 816–22 (1956).

[Waps1977] A. H. Wapstra and K. Bos. *The 1977 Atomic Mass Evaluation*. At. Data Nucl. Data Tables **19**, 175–297 (1977).

[Wint1987] C. Winter, B. Krusche, K. P. Lieb, T. Weber, G. Hlawatsch, T. von Egidy, and F. Hoyler. *Spectroscopy of $^{88}$Sr with the $^{87}$Sr(n,$\gamma$) and $^{87}$Sr(d,p) Reactions*. Nucl. Phys. A **473**, 129–59 (1987).

[Wong1998] S. S. M. Wong. *Introductory Nuclear Physics*. John Wiley & Sons, New York, 2nd edition (1998).

[Wurz1994] P. Wurz and K. R. Lykke. *Kinetics of Multiphoton Excitation and Fragmentation of $C_{60}$*. Chem. Phys. **184**, 335–46 (1994).

[Zgan2002] E. F. Zganjar, A. Piechaczek, G. C. Ball, P. Bricault, J. M. D'Auria, J. C. Hardy, D. F. Hodgson, V. Iacob, P. Klages, W. D. Kulp, J. R. Leslie, M. Lipoglavsek, J. A. Macdonald, H.-B. Mak, D. M. Moltz, G. Savard, J. von Schwarzenberg, C. E. Svensson, I. S. Towner, and J. L. Wood. *Tests of the Standard Model from Superallowed Fermi β-Decay Studies: The $^{74}$Rb β-Decay*. In M. Leino *et al.* (eds.), *Proc. of the ENAM2001 Conference*, Eur. Phys. J. A (2002), in press.

[Zumb1982] J. D. Zumbro, A. A. Rollefson, R. W. Tarara, and C. P. Browne. *Q Values for Proton- and Deuteron-Induced Reactions on Selenium Targets*. Phys. Rev. C **26**(6), 2668–9 (1982).